Development of an automated procedure for morphometric analysis of neurons in culture

Ph.D. Thesis

Dmitry Karasik

Protein Laboratory

Institute of Molecular Pathology

Faculty of Health Sciences

Copenhagen University

2005

Preface

The work of this thesis was performed during the years 1999-2003 at the Protein Laboratory, Institute of Molecular Pathology, Faculty of Health Sciences in the research group of Professor *Elisabeth Bock*. Parts of the work of this Ph.D. study have resulted in the following publications:

- Berezin A, Karasik D, Belman V, Berezin V, Bock E. Prima - Perl toolkit for X, win32, & OS/2 PM. *Proceedings of the Open Source Convention,* August 1999, Monterey CA.

- Karasik D, Berezin A, Belman V, Sporring J. Graphical User-Interface and Image Processing for Perl. *Software: Practice and Experience.* Article in press, scheduled to appear in April 2005.

- Karasik D, Li S, Novitskaya V, Berezin V, Bock E. An automatic procedure for the evaluation of neurite outgrowth (manuscript).

Abstract

The neuritogenic response to a variety of environmental cues is an essential attribute of neuronal differentiation. Therefore evaluation of neurite outgrowth is a valuable tool for the study of the molecular mechanisms controlling differentiation of neuronal cells and remodeling of neuronal extensions important for neuronal plasticity. Manual analysis of neurite length is a most time consuming step if the goal is to process numerous series of images. In the thesis, an algorithm for digital analysis of images of primary cultures of dissociated neurons immunostained for neuronal markers using a fluorescent tag is presented. The algorithm includes the following operations: ridge detection, skeletonization and blob extraction. The automated object recognition method for estimation of neurite length was compared with a previously developed stereological procedure employing primary cultures of rat hippocampal and cerebellar granule (CGN) neurons. Differentiation of hippocampal neurons was induced by treatment with various concentrations of the S100A4 protein, whereas neurite outgrowth in CGN cultures was stimulated by treatment with an NCAM mimetic peptide, P2, and an FGF mimetic peptide, 10F10, in the absence or presence of various concentrations of an inhibitor of the FGF receptor, SU5402. In all cases it was found that the values of neurite lengths obtained employing the automated approach positively correlated with those obtained using the stereological method with correlation coefficients of 0.82, 0.90, and 0.91, respectively, indicating that the developed algorithm provides a precise and efficient method for the estimation of neurite outgrowth in cultures of primary neurons.

Furthermore, a set of software packages was developed for the research, including both end-user applications and development toolkits. The end-user programs such as PrLenS, MorphometryI, ManCen, and PrAverB were extensively used in my project and as well as by other researchers at the Protein Laboratory (Kolkova et al., 2000a and 2000b, Køhler et al., 2003, Ditlevsen et al., 2003, Soroka et al., 2003, Neiiendam et al., 2004, Pedersen et al., 2004). The applications were developed using the toolkits Prima and IPA

(the latter is named after an abbreviation of 'image processing algorithms'), stand-alone software packages for the Perl language, that provide graphical user-interface and image processing functionality with features not found in any other Perl toolkits. Prima is a platform-independent Perl graphic toolkit with an object oriented interface. Its features include (i) an extensive set of Perl-coded interface elements (widgets), (ii) a wide range of image types and conversion routines, and (iii) a visual builder. IPA is an image processing toolkit that provides a set of common two-dimensional operators, and it is based on the Prima toolkit.

In this thesis, a fully automated procedure for quantification of neurite outgrowth is described. The procedure is based on a new computation method, which in turn is based on a general ridge enhancement technique and analysis of pixel intensity distribution in fluorescent images of primary cultures of neurons immunostained for a neuronal marker, GAP-43. The software used for the quantification of neurite outgrowth was implemented using Prima and IPA toolkits.

List of Contents

List of Figures

List of Abbreviations

10F10-d   dendrimeric form of 10F10 peptide

1D,2D,3D   one (two, three) - dimensional

BDNF   brain-derived neurotrophic factor

bFGF   basic fibroblast growth factor

BSA   bovine serum albumin

C3d   dendrimeric form of the C3 peptide

CAMs   cell adhesion molecules

CGN   cerebellar granule neurons

CNS   central nervous system

CPU   central processing unit

CSPGs   chondroitin sulfate proteoglycans

ECM   extracellular matrix

FBS   fetal bovine serum

FGF   fibroblast growth factor

FGFR   fibroblast growth factor receptor

GAP-43   growth associated protein-43

GCC   GNU C Compiler

GIF   Graphics Interchange Format

GIMP   GNU Image Manipulation Program

GNU   GNU's Not Unix

GTK   GIMP Toolkit

GTP   guanosine-5'-triphosphate

GUI   graphical user interface

HB-GAM	heparin-binding growth-associated molecule
HEPES	4-(2-hydroxyethyl)-1-piperazineethanesulfonic acid
HTML	hyper-text markup language
Ig	immunoglobulin
IPA	image processing algorithms
IPL	image processing library
IUR	independent, uniform, random
MAG	myelin-associated protein
MAP	microtubule-associated protein
MAPK	mitogen-activated protein kinase
MSVC	Microsoft Visual C++
NCAM	neural cell adhesion molecule
NGF	nerve growth factor
NS	nervous system
NT	neurotrophin
OS	operational system
P2d	dendrimeric form of the P2 peptide
p75^{NTR}	p75 neurotrophin receptor
PBS	phosphate buffered saline
PC12	rat pheochromocytoma cell line
PDL	Perl data language
PNS	peripheral nervous system
SDGF	schwannoma-derived growth factor
SDK	software development kit
SU5402	3-[(3-(2-carboxyethyl)-4-methylpyrrol-2-yl)methylene]-2-indolinone
Trk	tropomyosin-related kinase
XML	extensible markup language

1 Introduction

Neuronal differentiation is a fundamental aspect of the embryonic development of the nervous system. The important morphological determinants of neuronal differentiation are initial sprouting of processes (neurites) followed by elongation of axons and pathfinding and also by dendritic arborization ultimately resulting in the formation during development of a complex neuronal network. Numerous environmental cues such as extracellular matrix-associated neurite promoters, cell adhesion molecules, neurotrophic factors, proteoglycans etc. are involved in controlling the initiation and guidance of a neurite (Kiryushko et al., 2004). Neuronal differentiation and neurite outgrowth are also important features of the processes of neuro-regeneration following traumatic injury in the peripheral (PNS) and central nervous system (CNS) and recovery after an ischemic insult. In the CNS, neuro-regeneration is manifested by proliferation of neural stem- and progenitor-cells, their migration and differentiation into neurons and by neurite outgrowth (McKerracher, 2001; Forbes et al., 2002). Finally, the constant adaptation of an individual to the environmental demands continuous changes in the morphology and function of synapses including the establishment of new synapses and the removal of functionally obsolete synapses. These processes which are pivotal in e.g. memory and learning require the capacity to extend and retract neurites.

Identification of environmental cues and also artificial compounds promoting neuronal differentiation and neurite outgrowth is of importance for our understanding of the molecular mechanisms underlying neuronal differentiation and pathfinding, and also for the development of drugs for the treatment of neurodegenerative disorders. Cell cultures of primary neurons or neuronal cell lines are often used for this purpose. The simplest and fastest method to monitor the effect of compounds on neuronal differentiation and plasticity of neuronal processes is morphometric analysis of neurite outgrowth in cell culture. This approach is also useful to study the signal transduction mechanisms underlying differenti-

ation of neurons. Recent advances in modern microscopy using a computerized microscope workstation have facilitated morphometric analysis of neuronal cell cultures dramatically. The microscope table positions, filter wheel changes, auto-focusing and the frame grabber for time-lapse video recording all can be controlled by special software allowing fully automated image sampling from multiple microscopic fields. However, the time-consuming step in the evaluation of neurite length is the analysis of multiple recorded images, which in general consists of retrieving images one at a time and tracing neuronal processes by means of a computer mouse. Some years ago a procedure for quantification of neurite outgrowth based on stereological principles was developed at the Protein Laboratory (Rønn et al., 2000). This stereological method essentially is based on use of specific sampling rules and an unbiased counting frame incorporated into a software package PrLenS. These modifications allow reduction of the time spent on measurements of the neurite length to 20% of the time required for the manual neurite-tracing analysis (Rønn et al., 2000). In this thesis a fully automated procedure for quantification of neurite outgrowth is described. The procedure is based on a new computation method, which in turn is based on a general ridge enhancement technique and analysis of pixel intensity distribution in fluorescent images of primary cultures of neurons immunostained for a neuronal marker, GAP-43.

2 Background

2.1 Factors regulating neurite outgrowth

In vertebrates, the nervous system develops from two cell complexes of ectodermal origin, the neural tube and the neural crest. The neural tube is the source of the CNS, while the neural crest is the source of the majority of neurons and glial cells in the PNS. During development of the PNS, cells from the neural crest undergo a number of transformations leading to their differentiation into various types of neurons and glial cells. Neural precursors, the neuroblasts, migrate out of the neural crest, differentiate, and assemble into a functional network by growing dendrites and axons (collectively named neurites) which make multiple specialized contacts (synapses).

Neurite outgrowth proceeds by the dynamic behavior of a specialized part at the tip of a process, called a growth cone. The growth cone at the end of the neurite can advance approximately 1mm per day. The growth cone is a broad, thickened part of the neurite with a number of long thin filopodia. Filopodia constantly extend and retreat, guiding the growth cone. The migration of a growth cone results in neurite elongation, while its splitting creates a branch point. The migration can be directed by selective adhesion, properties of the substratum, and diffusible molecular cues (Alberts et al., 1989).

The process of neurite formation is usually triggered by the binding of a neuritogenic ligand to its receptor and the subsequent activation of the corresponding intracellular signalling cascades. A number of substances promoting neurite extension has been identified, along with compounds retarding and prohibiting the outgrowth. Both attractive and repellent guidance molecules exist, many of these possessing both properties depending on cell type and conditions (Kiryushko et al., 2004).

The processes of neural development and regeneration are based on the ability of axons and dendrites to grow in a highly persistent and directed manner. This is accomplished by

the patterns of attractant and repellent activities changing both in space and time. To navigate between the guiding cues, the growth cone and filopodia possess cell-surface receptors for extracellular signals, so that the recognition of signalling molecules by the growth cone drives the neurite toward the appropriate target cell. The extracellular signalling cues can either attract or repel growth cones, and operate either at close range or over a distance (Tessier-Lavigne et al., 1996).

2.1.1 Signals originating from the extracellular matrix (ECM)

Various molecular components of the ECM regulate growth-cone movement and morphology of early neurites.

Glycoproteins belonging to the laminin, fibronectin, and tenascin protein families are known to promote neurite outgrowth. Laminins constitute a family of proteins found largely in the basal laminae. They play a major role during neuronal development, binding with various sites to collagen, and specific non-integrin and integrin receptors. Binding of laminin to integrin receptors triggers intracellular signalling. Also, laminins are found to serve as attractive guidance cues and as neurite growth promoters (Tardy, 2002). Fibronectins are soluble multi-adhesive ECM proteins capable of binding to a multitude of cellular and ECM molecules (Ruoslahti et al., 1996). In the NS fibronectins primarily target the integrin receptors, initiating various intercellular signalling processes and consequently affecting cell adhesion and migration (Choung et al., 2002). Tenascins constitute a family of ECM glycoproteins which induce neuritogenesis of different types of neurons. The neuritogenic effect of tenascin C was shown to be mediated by both direct and indirect interactions with cell surface integrins and cell adhesion molecules (CAMs)(Rigato et al., 2002). The family of glycosaminoglycans is represented by molecules carrying large polysaccharide chains, of which neural cells express mainly heparan sulfates, hyaluronate, and chondroitin sulfates. Heparan sulfates and hyaluronate promote neuritogenesis, while chondroitin sulfates act as outgrowth inhibitors. Heparan sulfates promote axonal outgrowth and pathfinding (Halfter, 1993) and participate in establishing of axonal pathways (Joseph et al., 1996).

Hyaluronate is a major component of the ECM around migrating and proliferating cells. By binding to the surface receptor CD44 hyaluronate activates intracellular signalling cascades and promotes cell growth and migration. It has also been shown to inhibit neurite outgrowth *in vitro* (Oohira et al., 2000). The heparin-binding growth-associated molecule (HB-GAM) is a secretory ECM-associated protein, shown to promote outgrowth of neurites

in the CNS and PNS (Raulo et al., 1992; Pavlov et al., 2002).

2.1.2 Trophic factors

The growing neurons compete for specific trophic polypeptides, secreted by target tissues (Raff, 1992). The selective survival of neurons is regulated by a number of growth factors belonging to the neurotrophin family, and the first discovered neurotrophin was termed nerve growth factor (NGF) (Levi-Montalcini et al., 1961). Other members of the family are brain-derived neurotrophic factor (BDNF), neurotrophin-3(NT-3), and neurotrophin-4 (NT-4). Neurotrophins bind to and activate two types of receptors, the tropomyosin-related kinase (Trk) and p75^{NTR} (Huang et al., 2001; Lee et al., 2001). Binding of individual neurotrophins activates different Trk receptors: NGF binds to TrkA, BDNF to TrkB, and NT-3 binds to TrkC. Also, different intracellular signalling cascades are triggered by neurotrophins, including the pathways involving phospholipase C (PLC), Ras-MAP kinase, and PI3-kinase (Markus et al., 2001; Sofroniev et al., 2001). p75^{NTR} also binds to all neurotrophins but with lower affinity. When Trk and p75^{NTR} receptors are activated simultaneously, the specificity of the binding increases. Interestingly, binding of NGF to p75^{NTR} without binding to TrkA may promote cell death (Patel et al., 2000).

The family of fibroblast growth factors (FGFs) plays a critical role in the development of the CNS (Murphy et al., 1990). In the developing NS, neurons predominantly express the FGFR1, and glial cells the FGFR2. The binding of FGFs to FGFRs leads to receptor dimerization which allows autophosphorylation of their tyrosine kinase domains (Williams et al., 1994). These events in turn activate a number of signalling cascades, which stimulate neuronal cell differentiation and survival (Desire et al., 1998; Pataky et al., 2000). Neurite outgrowth is simulated by FGF via activation of a second messenger pathway that requires calcium influx into neurons via Ca^{2+}channels (Archer et al., 1999).

2.1.3 Guidance molecules

Studies *in vivo* indicate that neurons can grow towards distant targets and do so in a stepwise fashion. The intermediate targets that guide the growth cone on its way to the final destination are various molecules, acting as attractants or repellent cues depending on the cell type and physiological conditions. The most studied guidance molecules are the families of netrins, semaphorins, ephrins, and slits.

The family of Netrin proteins functions as both attractive and repellent cues by binding to the UNC-40 and UNC-5 receptor proteins (Livesey, 1999; Keleman et al., 2001; Gitai et al., 2003).

Semaphorins are a large family of transmembrane proteins with bi-functional properties. Semaphorins act as inhibitory cues by activating the Rho-family of GTPases (Jin et al., 1997), and as attractive cues by activating MAPK signalling pathways (Pasterkamp et al., 2003).

Ephrins are developmentally regulated molecules that contribute to axonal pathfinding through their binding to the Eph receptor tyrosine kinases. Ephrins mainly act as inhibitory cues (Henkemeyer et al., 1996), but some members act as attractive cues (Brownlee et al., 2000; Moreno-Flores et al., 2002) in axon guidance processes in the brain.

Slits are large bi-functional proteins acting as repulsive cues for axons in the CNS (Ringstedt et al., 2000; Sang et al., 2003).

2.1.4   Cell adhesion molecules (CAMs)

Adhesion of neighbouring cells is a primary feature of the architecture of many tissues, including CNS. CAMs enable neurons to adhere tightly and specifically with cells of the same or similar type. Most of CAMs mediate neurite outgrowth by triggering intracellular signalling cascades. There are four major families of CAMs: integrins, cadherins, immunoglobulin superfamily CAMs (Ig CAMs) and selectins.

Cadherins mediate calcium dependent homophilic binding, whereas integrins require both calcium and magnesium for their function. Ig CAMs are defined by the presence of one or more copies of the Ig homology modules which have a characteristic Ig-fold, a compact structure with two cysteine residues separated by 55-75 amino acids (Vaughn et al., 1996). The selectins are not involved in neurite outgrowth.

Three main CAMs in the vertebrate nervous system, N-cadherin of the cadherin family, and L1 and NCAM of the Ig superfamily, are strong stimulators of neurite outgrowth. They activate the elongation of processes via various signalling cascades, where the most common are pathways activated via the FGF receptor (Perron et al., 1999; Kolkova et al., 2000a).

N-cadherin mediates cell adhesion both in developing and mature tissues, participates in a number of morphogenetic events (Ivanov et al., 2001), and is an important regulator of neurite outgrowth, axonal guidance and fasciculation during neural development (Shiga et al., 1991).

The neuronal cell recognition molecule L1 is expressed in the developing

NS and has a crucial role in the NS maturation, including axonal outgrowth (Brummendorf et al., 1998). In vitro, L1 strongly stimulates neurite outgrowth (Doherty et al., 1992; Doherty et al., 2000).

In the developing NS, NCAM appears early in embryonic development. It is detected at the blastoderm stage, and later it is expressed on the derivatives of all three germ layers (Crossin et al., 1985; Edelman, 1986). In the mature organism, NCAM is mainly expressed in tissues of neural origin, although some non-neural tissues continue to express low amounts of NCAM throughout life. *In vitro*, NCAM strongly stimulates neurite outgrowth (Doherty et al., 1992).

2.1.5   Inhibitors of neurite outgrowth

A number of molecules are known to cause growth cone collapse. During normal development, the inhibitory cues assist the correct wiring of the NS by repelling growing neurites from certain areas and abrogating outgrowth after the development is complete. In the CNS, contrary to the PNS, axons do not re-grow after damage, primarily due to inhibitory molecules produced by oligodendrocytes, especially during the response to CNS injury. The most studied inhibitory proteins are chondroitin sulfate proteoglycans (CSPGs), myelin-associated protein (MAG), and Nogo-A.

CSPGs are powerful blockers of neurite outgrowth and one of the best characterized inhibitory molecules of axon guidance in the CNS (Hartmann et al., 2001; Morgenstern et al., 2002; Jones et al., 2003). CSPGs such as neurocan and phosphacan can also bind growth factors (bFGF), and several cell adhesion molecules (Retzler et al., 1996; Rauch et al., 2001).

MAG specifically induces growth cone collapse by interacting with p75 and GT1b receptors (Vinson et al., 2001). However, MAG is also reported to stimulate neurite outgrowth from young neurons (Turnley et al., 1998).

NogoA is a powerful CNS myelin inhibitor. It contains three functional domains: the N-terminal region, the C-terminal region (Nogo66) and amino-Nogo; they all strongly inhibit neurite outgrowth (Oertle et al., 2003). Nogo66 directly activates the Rho GTPase (Fournier et al., 2003) which results in a modification of the cytoskeleton in the growth cone.

16

2.1.6   Synthetic peptides

The study of the molecular mechanisms underlying the neurite outgrowth processes triggered by various factors revealed that peptide motifs can mimic the effect of growth factors and adhesion molecules on the activation of the signalling cascades leading to neurite outgrowth. Several peptides have been shown to produce neuritogenic effects.

Peptides derived from the variable chain of antibodies against the neural cell adhesion molecules L1 and CHL1 have been reported to promote neurite outgrowth from cerebellar neurons, dorsal root ganglion and motor neurons (Dong et al., 2002; Dong et al., 2003). Synthetic peptides derived from the alpha globular domain of laminin-1, AG73-chitosan and A99-chitosan, promote neurite outgrowth of PC12 cells (Mochizuki et al., 2003). A 15-aminoacid sequence from tenascin-C, D5, has been found to promote neurite outgrowth. The sequence is critical for the interaction of tenascin-C with neurons (Meiners et al., 2001). A peptide sequence from Schwannoma-derived growth factor (SDGF) termed SDGF(38-80) has been demonstrated to induce short neurite outgrowth in PC12 cells (Takenouchi et al., 1999).

It has been shown that neurons respond to specific NCAM isoforms with an increased neurite outgrowth. The extracellular portion of this molecule consists of five immunoglobulin (Ig) and two fibronectin type III (F3) modules, where the second Ig module is a natural ligand of the first Ig module (Kiselyov et al., 1997) forming *cis*-dimers of NCAM and inducing neurite outgrowth. Recently, a set of NCAM-mimetic peptides triggering activation of neurite outgrowth were identified (Berezin et al., 2004). A ligand of the N-terminal Ig module, C3, promotes neurite outgrowth in primary hippocampal neurons and PC12E2 cells (Rønn et al., 1999; Rønn et al., 2002). Its tetramer, C3d, disrupts NCAM-mediated cell adhesion, but activates simultaneously intracellular signalling cascades similar to those activated by homophilic NCAM binding (Kolkova et al., 2000a), and promotes neuritogenesis and synaptogenesis in primary neurons (Kiryushko et al., 2003). A 12-aminoacid sequence from the FG loop of the second Ig module of NCAM, termed P2, has been shown to inhibit cell aggregation, activate the MAPK signalling pathway and stimulate neurite outgrowth in primary hippocampal neurons (Soroka et al., 2002).

A recently identified peptide sequence motif derived from the second F3 module of NCAM, termed the FGL peptide (Kiselyov et al., 2003), has been shown to induce neurite outgrowth from hippocampal, dopaminergic neurons and CGN (Neiiendam et al., 2004).

2.1.7 Metastasis-related protein S100 A4 (Mts1)

Identification of new factors with neurotropic activity is a crucial step in understanding the molecular mechanics behind neuronal development, plasticity, and regeneration. It was observed that members of the S100 protein family are expressed in different patterns during cell growth and differentiation. The observation indicated that the S100 proteins may play regulatory roles in these processes. Indeed, S100β, a protein contained at high levels in glial cells, was found to possess neurotrophic activity on neurons from the central nervous system (Kligman et al., 1985).

Proteins of the S100 family were initially discovered in the brain, and thus were believed to be specific to the nervous system. However the proteins were later found in other tissues and cells.(Donato, 2003). Intracellularly, S100 proteins interact with various targets and function as modulators for cellular processes, such as cytoskeleton remodelling, cell growth, and cell differentiation (Sorci et al., 2003). Extracellularly, dimers of the S100B protein are reported to function as neuronal survival factors and growth factors (Winningham-Major et al., 1989; Bhattacharyya et al., 1992).

Ample evidence suggest that the *mts1*/S100A4 gene plays an important role in tumor progression (Ambatsurmian et al., 1996; Li et al., 2003). It has been shown that S100 A4 (Mts1) affects cell motility and cytokinesis through its association with actin stress fibers (Kriajevska et al., 1998). Its role in metastasis has been suggested to depend on these effects.

Recently it has been confirmed that S100 A4 is a very efficient neuritogenic factor. The mechanism of S100 A4-stimulated neurite outgrowth involves activation of phospholipase C, protein kinase C, depends on the intracellular level of Ca^{2+}, and requires activation of the MAPK signal-regulated kinases 1 and 2 (Novitskaya et al., 2000).

2.2 Stereological quantification of neurite outgrowth

Stereology is a collection of tools for efficient estimation of quantitative properties of real world structures. It is related to the areas of stochastic geometry and spatial statistics, and allows estimation of geometric parameters of any dimension. The basic methods are traditionally used to estimate volume (three-dimensional (3D) parameter), area (2D parameter), length (1D parameter), and number of objects (non-dimensional parameter) (Russ et al., 2000).

The stereological methods have been successfully applied in the field of histology for estimation of the number of cells, length of neuronal processes etc (Abercrombie, 1946; Andersen et al., 2003).

2.2.1 Sampling design

Sampling in stereology is a pivotal issue, because stereological methods are concerned with extraction of information about the total structure while only a part of it is available for quantification. The essence of sampling is the selection of parts of the population to infer correct conclusions about the entire population (Cassel et al., 1993). Two sampling approaches which are used in a wide range of statistical applications, are termed the model-based and the design-based approach, respectively. Below cell counting methods based on the two approaches are reviewed.

2.2.1.1 Model-based approach

The model-based approach is based on information about the sampled objects (Geuna, 2000). Models are built from available object information, such as shape or size, and from either *a priori* knowledge or assumptions about probability of objects to be sampled. If the assumptions are not robust or predictive, bias may be introduced. The precision of an estimate can be detected from the coefficient of error from the data themselves, although it is not possible to infer the bias from the data. Therefore, the model-based methods have to be combined with calibration studies and correction factors.

The *simple profile-based counts* method is based on the assumption that the total number of objects is directly proportional to the number of cross-sectional object profiles, and can directly be deduced from this number. In neurobiological studies this assumption does not hold since most cells from the nervous system possess large morphological differences.

The dependency of the simple profile-based models validity on morphology of objects being sampled is studied in (West, 1993; Coggeshall et al., 1996). Also, when sectioning of tissue is used, eventual cell fragments count as entire cells which leads to over-estimation, inversely proportional to the thickness of the section.

The *Abercrombie method* (Abercrombie, 1946) aimed to correct the over-estimation by accounting for the section thickness. The multiplication factor $\frac{T}{T+H}$, where T is the mean section thickness and H is the mean cell height is applied to the raw experimental data to obtain corrected results. The model contains the assumption that H, which is measured on the z axis, correlates with the probability of cells being sampled in the x and y axes. Still, biases may be present with the Abercrombie method, in particular those induced by the problem of lost caps, which occurs when small parts of cells are barely within, or have fallen out of, the section surface and therefore are not counted (Hedreen, 1998; Hedreen, 1998). Additional bias is introduced when size, shape, and orientation of cells are not taken into account (Abercrombie, 1946; Hendry, 1976). The *Floderus method* (Floderus, 1944) introduces the lost-caps correction factor, but since it assumes spherical cell configuration it can only be used for estimations of the number of spherical cell bodies (Mendis-Handagama et al., 1992). Fullman's (Fullman, 1953) and Hendry-Coupland's (Hendry, 1976) corrections are free of this assumption (Smolen et al., 1983).

The *empirical counting methods* are free of the lost caps problem by performing a preliminary study which is conducted so the population-specific ratio between the true reconstructed cell number and the number of the corresponding profiles is calculated. The model is reported to produce unbiased results (Pover et al., 1991; Hedreen, 1998).

2.2.1.2 Design-based approach

The design-based approach, contrary to the model-based, has no assumptions about the population. Also, it enforces the equal opportunity rule, where all objects from the population have one and the same probability of being sampled. The rule has to be observed when selecting both sampling units and estimation rules. In theory, design-based methods may produce unbiased (Hedreen, 1999) results without any additional correction factors (Mayhew et al., 1996; West, 1999); in practice the total absence of bias is unattainable.

A direct sampling scheme, the *simple random sampling* where all possible combinations of n sampling units have the same probability of being sampled, requires large number of samples for achieving a sufficient precision. Series of sampling designs have been devised to circumvent this problem. The *multistage* sampling deals with sub-samples, extracted

from larger samples, which are in turn extracted from the population total. The *stratified* sampling is similar to the multistage in that the population total is divided into strata that are sampled separatedly. The *systematic random sampling* method consists of a systematic selection of every n^{th} unit of the population, starting from a randomly selected starting point. The systematic sampling appears to be the one that best fits the requirements of neuromorphological research (Geuna, 2000).

Series of estimators that fulfill the equal opportunity requirement for the design-based approach were devised both in two and three dimensions. Sterio (Sterio, 1984) proposed a *physical disector* probe, consisting of two parallel planes separated by a known distance, and used for estimation of the population in the volume. Gundersen (Gundersen, 1986) adapted the method for neuromorphological needs with *the optical disector* probe, where slices are separated by focal planes. The extension of the optical disector method, *the optical fractionator,* is a combination of a sampling design of a *fractionator* volumetric probe with the optical disector estimator (Gundersen et al., 1988).

Traditionally IUR (isotropic, uniform, and random) sampling designs are preferred because by definition they require no special correction for bias. However, in special cases non-IUR designs can be successfully used (Dorph-Petersen et al., 2000).

2.2.2   Statistical principles of stereological estimation

The estimation, as the process of inferring a total of a parameter, by measuring the parameter in parts of the total, is used widely in statistics and is directly related to the sampling design. If the total parameter can be expressed as

$$\hat{X} = \int_X f(x)dx \tag{2.1}$$

where X is the total, $f : X \rightarrow \mathbb{R}^+$ is the observation for each $x \in X$, then an unbiased Horwitz-Thompson estimator (Cassel et al., 1993) can be used to describe the relation between a parameter available from the sample, the sampling density (probability), and the total:

$$\hat{X} = \int_{\mathbf{S}} \frac{f(x)}{p(x)}dx \tag{2.2}$$

where $\mathbf{S} \subseteq X$ is the sample and $p(x)$ is the sampling probability of the individual x. In practice, random sampling methods based on this estimator are not always efficient, and therefore are often preferred to systematic random sampling methods (Cruz-Orive, 1993;

Geuna, 2000). The corresponding estimator in its generic form is

$$\hat{X}_T = T \sum_{k \in \mathbb{Z}} f(\mathbf{U} + kT) \tag{2.3}$$

where $\mathbf{U}$ is uniform random in an interval of the real axis of the length T.

The Horwitz-Thompson estimator can be used for estimation of the curve length. The modified Cauchy-Crofton formula

$$L = \frac{1}{2} \int_0^\pi \int_{\mathbb{R}} |\{\ell(\theta, x) \cap R\}| dx d\theta \tag{2.4}$$

where $\ell(\theta, x)$ is a line with direction θ and distance x to O, R is the curve in the plane, and $|\cdot|$ indicates number of elements and is essentially the total of intersections between $\ell(\theta, x)$ and R. In order to employ systematic random sampling where a sample can be expressed as

$$\{\mathbf{\Theta}, \mathbf{U} + kT\}_{k \in \mathbb{Z}} \tag{2.5}$$

uniform random variables $\Theta \sim U[0, \pi)$ and $\mathbf{U} \sim U[0, T]$ where $T \in \mathbb{R}_+$ are introduced. Here, the sample parameterizes a set of parallel and equidistant lines

$$\{\ell(\theta, x) : (\theta, x) \in \{\mathbf{\Theta}, \mathbf{U} + kT\}_{k \in \mathbb{Z}}\} \tag{2.6}$$

and is essentially the total of intersection points between the curve and the set of equidistant and parallel test lines with randomly chosen direction and position. The curve length estimator is thus

$$\hat{L} = \frac{1}{2}\pi T N \tag{2.7}$$

where N is the number of intersections and T is the distance between test lines. In 3D, curve length is estimated correspondingly by 3D probes (Mouton et al., 2002).

The variance for the systematic random sampling cannot be estimated by a standard formula, since the observations are neither independent nor identically distributed. In terms of covariogram g of f ,

$$g(y) = \int_{\mathbb{R}} f(x) f(x + y) dx \tag{2.8}$$

the variance of $\hat{X}_T$ may be interpreted as the difference between the integral of g and its

discrete approximation (Gundersen et al., 1999):

$$\mathrm{Var}(\hat{X}_T) = T \sum_{j \in \mathbb{Z}} g(jT) - \int_{\mathbb{R}} g(y) dy \qquad (2.9)$$

The variance of $\hat{X}_T$ can be estimated by transitive methods (Matheron, 1965; Matheron, 1971) for small T. For the worst case, where the measurement function is not continuous, the magnitude of the approximated variance is of the order T^2 (Kiêu, 1997; Kiêu et al., 1999).

2.2.3 Sampling methods in neurobiological research

2.2.3.1 Cell counting

Both model-based and design-based counting methods are traditionally used to acquire the number of cells in biological tissues. In 3D estimation the counting of biological particles is performed by various modifications of design-based methods, the disector and the fractionator, which are based on unbiased principles (Mandarim-de-Lacerda, 2003).

The fractionator is a method for estimation of particle number (Gundersen et al., 1988). The principle of the fractionator is that the population is partitioned, and then a known fraction is sampled, the fraction is partitioned and the sub-fraction is taken. This process is repeated until the final sub-fraction is considered appropriate for the analysis. The estimate for the population total is the parameter observed from the final sub-fraction multiplied by the inverse fraction of sub-samples.

Another unbiased estimation method, the disector (Sterio, 1984), can also be used for cell counting. A schematic representation of the disector is given in Figure 2.1.

The exclusion lines and planes in the disector method provide independence of the morphological variation between particles and against counting the same object two or more times. The sections can be both physical and optical, and the principles of the method can also be applied to counting planar objects in 2D. The schematic representation of the method is given in Figure 2.2.

The randomness requirements, where there are no selected or consistent placement of measurement regions, must be observed at all time. In the *in vitro* neuronal culture, which is characterized by sparseness of individual cells, no preference over registration place because of clumping, sparseness, or other subjective criteria must be made.
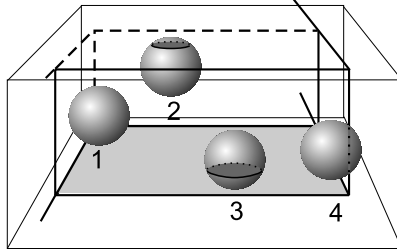
Figure 2.1. Schematic representation of the disector.
The unbiased counting frame is projected at the section volume, where two frame sides are parts of the section planes, and one of them is the exclusion plane. In the example, the lower plane is selected as the exclusion plane, and the particles that cross the plane (object 3) or the exclusion lines (object 4) are not counted. Thus, only object 2 is to be counted, as object 1 is fully within the section and is not representative.
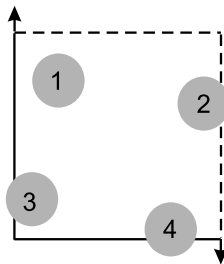
Figure 2.2. Schematic representation of the method for object counting in 2D.
The unbiased counting frame is superimposed on the planar image. Particles that cross the exclusion lines are not counted. Here, objects 1 and 2 are to be counted, whereas objects 3 and 4 cross exclusion lines and are excluded.
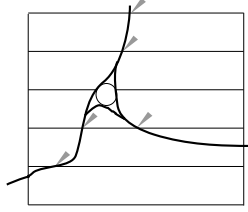
Figure 2.3. Curve length estimation by counting intersections with the lineal sampling grid.
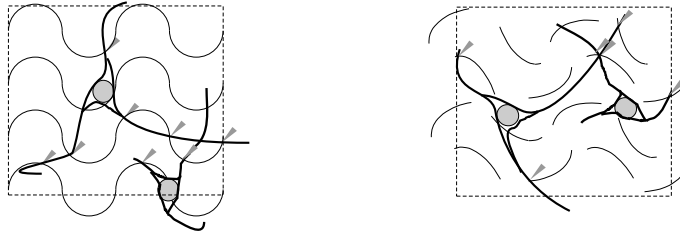
Figure 2.4. Curve length estimation by counting intersection events with isotropic curvilineal sampling grids.
The sampling grid on the left is constructed from parallel circular line probes. The sampling grid on the right consists of a set of disjointed cycloid curves.

2.2.3.2 Neuritic length estimation

Estimation of neuritic length in 2D is based on treatment of neurites as ideal lines that are counted by estimation of the number of intersection events with a sampling grid. If the sampling grid is constructed from a set of parallel equidistant test lines, then the curve length estimator $\hat{L} = \frac{1}{2}\pi TN$ is used, where N is the number of intersections and T is the distance between lines. An example of a lineal sampling grid is given in Figure 2.3.

Typically, neuronal cultures do not have any intrinsic orientation; but in case they do, the isotropy requirement does not hold, and therefore the stereological design must provide isotropy. In practice compensation is either obtained by rotating on the image acquisition stage, or a variant of the lineal sampling grid is used, where straight lines are replaced with circular or cycloid features, either as lines or as disjointed curves (see Figure 2.4). Cycloid sampling grids are typically used in 3D line length estimation methods, because grids constructed from circular curves do not provide unbiased measurement.
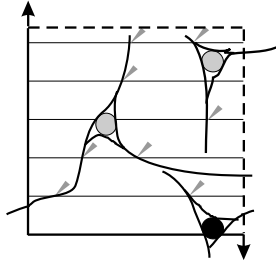
Figure 2.5. Simultaneous estimation of number of cells and neuritic length.
The number of cells is counted with respect to the unbiased counting frame. The cell body marked black is not counted as it touches the exclusion line. Neuritic length is estimated from the number of intersections between the neurites and the sampling grid. The normalized average neuritic length is a ratio between the estimated total neuritic length and the estimated total number of cells.

2.2.3.3 Combined set-up

Since neuronal cells in cultures typically are interconnected, the estimated neuritic length is more useful when counted per-cell, or as normalized neuritic length

$$\bar{L} = \frac{L}{C} \tag{2.10}$$

where L is an estimate of the total observed neuritic length, and C is an estimate of the total number of cells. For efficiency, the counting frame and the sampling grid can be combined. The combined setup depicted in Figure 2.5 is minutely described in Rønn et al. (2002) where individual rules for both unbiased cell counting and length estimation apply.

2.3 Quantification of cell morphology based on image analysis

Manual methods for quantification of biological features are dependent on the subjectivity of an operator and psychological factors such as stress and fatigue. Therefore it is preferred to conduct quantitative studies by employing non-subjective image analysis techniques for segmentation of a variety of structured features. In particular, quantitative analysis of cell cultures has a long history (Macagno et al., 1979; Connor, 1986; Smith et al., 1996; Sack et al., 2003). The utilization of image processing for analysis of biological structures is an active research field, and new studies report successful application of image processing techniques for quantification of neuronal outgrowth (Dima et al., 2002; Weaver et al., 2003).

The automatic quantification methods are based on various image processing algorithms that almost always require preliminary tuning before they can be applied to the acquired data. The algorithms for extraction of desired features, such as neurites or cell bodies employ various models for representing the feature in the feature space of the experiment, which is defined primarily by biological variability of cells and image recording conditions. Neural cells can crudely be modeled as a combination of circular blobs (cell body) and curvilinear features (neurites), and therefore the majority of neurite outgrowth quantification frameworks target these as features of interest. Some feature-based approaches are described below.

2.3.1 Segmentation methods

When features in images can directly be approximated by the corresponding pixel intensity, image segmentation methods can be used for feature extraction. The segmentation methods divide pixels into categories, depending on some property of one or more pixels in an image. Depending on segmentation rules, the pixels which belong to the desired features in the image are marked with an unique identifier, directly available as an estimate of the desired feature.

A group of *thresholding* methods performs classification for each pixel in the image using threshold values and a set of decision rules based on the pixel value itself, its local vicinity, or a global image parameter. Gray-level thresholding is the simplest but often effective method of image segmentation (Russ, 1995), since lighting in experiments often can be set

up so the only segmentation needed is the thresholding. More elaborate methods operate on the shape of the image histogram and select a threshold value depending on the position of histogram peaks, or seek the optimal solution to a certain function reflecting the segmentation result (Haralick et al., 1985). Non-parametric Otsu thresholding (Otsu, 1979) maximizes the ratio of the between-class variance to the total variance. Parametric thresholding methods operate on the assumption of normality of distribution, and they aim at the minimization of the probability of a false positive classification, by assigning a pixel to a class with maximum decision function response for it. Parametric minimum-distance thresholding methods try to estimate the distribution parameters by fitting the intensity histogram; maximum-likelihood methods estimate the set of parameters that maximize the probability of observation of the pixel intensity distribution (Titterington et al., 1985).

Region-based segmentation methods divide the image into several non-overlapping regions, based on a selected homogeneity criterion, such as the average intensity value or the texture energy. Regions are formed either by accumulating pixels around a "seed" in region-growing methods (Zucker, 1976), or decomposing an entire image into smaller parts until homogeneity condition holds in so called split and merge methods (Horowitz et al., 1975). The variational approaches segment the image so that a homogeneity criterion is maximized within regions and minimized along region boundaries (Mumford et al., 1988). The variational methods have been combined with active contours (Blake et al., 1988) that employ a propagated deformation of region boundaries to satisfy the minimization requirement (Chan et al., 1999). The region-based segmentation methods combined with the scale-space paradigm by accounting for the correspondence between structures extracted at different scales, are shown to aid over- and under-segmentation, and yield partitioning closer to visual perception for the generally orderless images (Olsen et al., 1997; Shi et al., 2000).

Further development of thresholding methods, which generally are of single modality, are image *classification* methods that are used for segmentation of multiple images representing features from the same feature space. The classification algorithms are either unsupervised or supervised; the latter require *a priori* information, typically a predefined set of classes with samples. The unsupervised methods include threshold-based parallelepiped method, objective function-based minimum distance, k-means, and fuzzy c-means methods (Dua et al., 1973; Bezdek, 1981). Supervised methods include probabilistic Bayes and k-nearest neighbour methods (Dua et al., 1973), as well as methods originating from the field of artificial intelligence, such as decision trees and artificial neural networks. These methods can be used for image segmentation when large number of

28

samples are available (Kamber et al., 1995; Tatsumi et al., 2002; Zheng et al., 2004). The Bayesian matching is employed in methods based on deformations of region boundary (Zhu et al., 1996; Sifakis et al., 2002).

Segmentation methods are seldom used alone, but rather at a pre-processing stage before further analysis in order to emphasize the desired features or reduce noise.

2.3.2   Mathematical morphology methods

Mathematical morphology operates with point sets, their connectivity and shape, assumed to model real images (Serra, 1982). A morphological transformation Ψ is given by the relation of the point set A (image) with point set B (structuring element). For example, morphological dilation combines two point sets A and B using vector addition in a result that is a set of all possible vector additions of pairs of elements, one from each of the sets

$$A \oplus B = \{p : p = a + b, a \in A \text{ and } b \in B\} \tag{2.11}$$

where a and b represent point set elements (pixels) as vectors. See Section 5.2.3.3 for the detailed formulation of some of the morphological operators.

Morphological operators are used mainly for image pre-processing, segmentation, extraction of object structure, and for description of quantitive parameters of an object such as area and perimeter. These tasks are directly applicable in the problem domain of analysis of microscopy images of cells.

Usually morphological operators are used together with other image processing algorithms. For example, segmentation techniques such as grayscale *watershed transform* (Vincent et al., 1991) are demonstrated to be used for cell quantification (Ranefall et al., 1997; Latson et al., 2003). A set of elementary morphological operators, including erosion, dilation, thinning, and reconstruction, as well as operators derived from them are used in a wide range of image analysis algorithms.

The morphological thinning operation converts an object into its representative skeleton preserving its topology. Variants of thinning algorithms are known, mostly based on a medial axis transformations (Lam et al., 1992). The thinning operation is an efficient tool for extracting object parameters such as length and connectivity. It is used in several algorithms for analysis of skeletonization of the cell body (Malgrange et al., 1994; Treubert et al., 1998). Figure 2.6 depicts result of the application of a thinning operation to a pre-processed and binarized microscopy image of neurites.
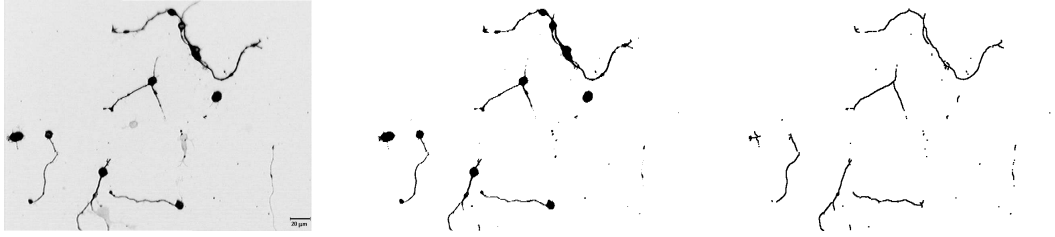
Figure 2.6. Morphological thinning applied to a binarized image of a stained neuronal culture.
On the left: an image recorded from the microscope. In the middle: an image converted to a binary form using the fixed threshold. On the right: the result of a skeletonization algorithm applied to the binarized image.

2.3.3   Edge-based techniques

On microscopy images neurites often manifest themselves as curvilineal structures, with widths significantly lesser than their lengths. Moreover, recording conditions usually can be adjusted so that neurites appear in contrast to the image background. Various image processing operators can assist in recovering the lineal or other features by analyzing magnitudes that correspond to the edge strength in the image.

A set of differential image processing operators, also called edge-detectors, calculate the edge magnitude from the difference between neighbouring pixels. The most known are the Marr-Hildreth, Sobel, Prewitt, and Canny edge detectors (Russ, 1995). In combination with thresholding and mathematical morphology-based techniques edge detectors can be used to extract various features from biological images (Jap et al., 1991), in particular to quantify neurite outgrowth (Bilsland et al., 1999). Edge-based techniques targeted at recovery of continuous feature outlines can be applied either to the results of edge detectors, or directly to the original image.

Ridge detection methods target ridge structures, defined similarly to edges on intensity images (Haralick 1983; Eberly et al., 1994). The local properties of an image are used to determine the strength of ridge points, which as well as information about edge points, can be used in higher-level image analysis. In terms of Gaussian function, the definition of edges and ridges is correspondingly based on the first and second derivatives of a Gaussian function (Lindeberg, 1998); other definitions of ridges exist (Crowley et al., 1984; Colchester, 1990).

Hough transform (Hough, 1962) allows extraction of curves described by paramet-

30

ric functions, such as straight lines, circles, ellipses, etc. Many variations of the original transform exist, for example, the normalized Hough transform is used when image dimensions inflict bias over the detected features (Hansen et al., 1997). The generalized Hough transform is used when the parametric description of the desired feature is not known (Ballard, 1981). Methods based on the Hough transform are used for quantification in a wide variety of biological applications, in particular for cell counting (Thomas et al., 1992; Barber et al., 2001).

Border-detection methods recursively traverse the input image and construct a border as a linked pixel chain, following some criteria. The simplest border detector follows the maximum magnitude in the neighbourhood. More advanced methods such as graph searching and methods based on dynamic programming use cost functions to navigate the direction of the border construction (Martelli, 1972). Combined with *a priori* knowledge about the desired features methods, based on dynamic programming are successfully used in angiography to recover outlines of arteries and heart ventricles (Sonka et al., 1994; Geiger et al., 1995). For reconstruction of neurite outgrowth, a track finding pattern recognition algorithm has been used on pre-processed images (Ford-Holevinski et al., 1986). Recently, algorithm for automatic extraction of neurite outgrowth based on ridge tracking algorithm was successfully used on images of retinal explant culture (Weaver et al., 2003).

In cases when interaction of an extraction algorithm with an expert is possible, semi-automatic methods can be used. For example, the *live-wire* paradigm (Barrett et al., 1997) which partially is driven by a border-detection algorithm and partially interactively by a human expert. Recently a live-wire setup combined with a neurite extraction algorithm based on approximation of a neurite as a Gaussian ridge has been reported (Meijering et al., 2004).

2.3.4 Multi-scale approaches

Image processing operators work on pixel level, and their parameters depend on the size of the detected features. In general it is not known how to interpret an image on the pre-processing stage, so in order to solve the problem, the phenomenon is observed at different resolutions, or *scales,* and at each a formal model is created (Witkin, 1983; Koenderink, 1984; Sporring et al., 1997; Sonka et al., 1998). The idea of scale is fundamental in Marr's 2D edge detection technique (Marr, 1982) where a particular scale is created as a result of convolution of the original image with a Gaussian kernel of the corresponding size,

$$G(x,y) = \frac{1}{2\pi\sigma^2} e^{-\frac{x^2+y^2}{2\sigma^2}} \tag{2.12}$$

where σ is the standard deviation of the normal distribution. It is related to the scale parameter t as

$$t = \sigma^2 \tag{2.13}$$

so that for any image f its scale-space representation L at the scale t is

$$L(\cdot; t) = G(\cdot; t) * f \tag{2.14}$$

Canny's edge detector (Canny, 1983; Canny, 1986) processes an image at different scales by convolving it with a 2D Gaussian function of corresponding σ values, and locates the edge by differentiating the result directionally. The edge location corresponds to the local maximum of the image f convolved with the first derivative of Gaussian in the direction $\mathbf{n}$:

$$|\mathbf{n}| = 1 \tag{2.15}$$

$$G_n = \mathbf{n} \cdot \bigtriangledown G \tag{2.16}$$

$$\frac{\partial}{\partial \mathbf{n}} G_n * f = 0 \tag{2.17}$$

The resulting edges at multiple scales are aggregated.

Canny's method was extended by the Lindeberg's approach, where edges are defined as intersections of two zero-crossing surfaces in scale-space (Lindeberg, 1998). In the method derivatives are normalized with respect to the scale t

$$\partial_\xi = t^{\gamma/2} \partial_x \tag{2.18}$$

where γ is normalization parameter of edge strength with respect to scale, favoring the edge diffuseness versus the spatial extent of the edge model. Maxima over scales of the normalized derivatives are used for automated scale selection, and extracted edges with a strength above a certain threshold are aggregated. The approach can also be used for ridge detection, where ridges are observed in zero-crossings of the second derivative instead of

the first. In terms of differential geometry a ridge is defined as

$$L_{uv} = 0 \tag{2.19}$$

$$L_{uu}^2 - L_{vv}^2 > 0 \tag{2.20}$$

where L are local derivatives in a (u, v) Gauge coordinate system, which is related to Cartesian system through partial derivatives,

$$\partial_u = sin\alpha\partial_x - cos\alpha\partial_y \tag{2.21}$$

$$\partial_v = cos\alpha\partial_x + sin\alpha\partial_y \tag{2.22}$$

and is characterized by the fact that one of two first-order derivatives L_u is zero, and v is the gradient direction.

Another approach uses 3D wavelet transform for edge extraction across scales with fixed scales (Dima et al., 2002), and is reported to be successful for quantification of neurons from confocal microscopy images.

2.4 Implementation

2.4.1 Programming language

End-user programs performing the actual image processing can be viewed as consisting of two functional parts, the back-end and the front-end. The back-end, which contains implementation of algorithms and no user interactions, are traditionally implemented in low-level languages as assembler or C, for the computation efficiency. The front-end provides an interface between the back-end and the user. The front-end tasks, especially dealing with graphic user interfaces, are efficiently written with higher-level, object-oriented languages, such as C++, or scripting languages such as Tcl or Perl (Lieberman, 1998).

The choice of language where the two parts are to be combined, usually favors the efficiency, and therefore the development of the user interface is often conducted with sub-optimal tools. One solution to the problem is to link parts written with different languages, optimal to each parts, together (Savikko, 2003). Below i briefly describe languages widely used for implementation of either image processing or user interface.

Machine *assembler* works at the lowest level directly interacting with computer's central processing unit (CPU). The efficiency of programs written in assembler is maximal within a particular computer architecture, although its cost-effectiveness is very low due to the fact that the programmer must explicitly account for each computational operation on the hardware level. Also, assemblers are typically specific to a particular architecture and are not portable. Nowadays, image processing programs written on machine assembler are used in microprocessors in video-recording devices for real-time picture enhancement and pre-processing (Kneip et al., 1995).

The languages *C* and *C++* are standard tools for implementation of image processing algorithms (Lindley, 1991). The majority of publicly available image analysis software is written in C or C++. The C++ is a near-complete super-set of C, and is a popular solution when a complex graphic user interface is to be linked with efficient back-end algorithms (Watson, 1993). Both languages are inherently portable and independent of hardware architecture, however the executable programs written in C and C++ are dependent on hardware and operational system (OS), and require a relatively high cost in development, especially where sophisticated user interfaces are involved. Also, where back-end parts in such a bipartite software model usually are not dependent on capabilities of either a particular OS or hardware, the front-end parts heavily depend on a graphic user interface

(GUI) library, where the latter usually is OS-dependent.

A family of *scripting languages* which includes Tcl, Perl, Python, Java, Lisp, Ruby, and others, is characterized by the fact that the programs written using these are neither dependent on hardware architecture, nor on the operational system. With the exception of a few platform-oriented languages, such as Microsoft Visual Basic, the scripting languages are mostly platform-independent (Barron, 2001).

The programs written in C, or assembler, or a similar language, require an additional step of compilation into the CPU instruction set before they can be executed. In contrast, programs written with the scripting languages are usually executable directly in the form of source code. The development costs using the scripting languages are also lower than using compilable languages, which is attributed to the absence of memory leak and violation problems, which constitute a large part of all problems in programs written in C and C++ . In particular, development costs for Perl and Python are reported to be about two times less than for C and C++ (Prechelt, 2000).

The scripting languages are not used for implementation of efficient algorithms due to their inherently low execution speed, because the programs are executed under a virtual machine. The linking of scripting languages with software written in C and C++ is possible and desirable especially where the software is OS and hardware-independent (Orwant et al., 1999; Wall et al., 2000).

2.4.2   Image processing software

A variety of existing generic software packages such as the commercially available Intel's IPL (Image Processing Library), Microsoft's Visual SDK, Matlab, Imagtek's REX, and public domain ImageMagick, SciLab, and ipl98 provide a large set of image processing operators and implementations of specifically targeted analysis algorithms for software development in C and C++ (Digital et al., 2002; Intel). Several provide links to other languages, for example SciLab contains the Tcl interface, and Matlab includes the Perl distribution (Scilab).

An example of a problem-oriented image processing software is PDL, the Perl data language toolkit (Soeller). PDL aims at integration of the scripting language Perl with an efficient implementation of a numerical algorithm, including a set of image processing operators.

2.4.3   Graphic user interface software

Software packages for enabling GUI in programs are mostly large stand-alone libraries, targeted at software development in C and C++ (Tai, 2003). These are divided in two large groups, platform-dependent and platform-independent. While both groups can be integrated with the scripting languages, integration of the platform-dependent libraries is less promising since the scripting languages are inherently platform-independent.

The most popular platform-independent GUI libraries, known to be successfully integrated with one or more scripting languages, are Qt, Gtk, Wx, FLTK, and Tcl-Tk (Tai, 2003; Blanchette et al., 2004; WxWindows). The last is a library originally created with a strong link to the scripting language Tcl . Link packages between the platform-independent libraries Qt, Gtk, and Wx and various scripting languages can be freely obtained. In particular, Perl can be linked with these libraries using freely available software packages (CPAN). Also, the Perl version of Tcl-Tk named Perl-Tk is freely available (Walsh, 1999; Tk).

Perl-Tk and Tcl-Tk are unique software packages in a sense that the underlying Tk core which is written in C and interacts with platform-specific GUI mechanisms is tightly interrelated with the scripting language, Perl and Tcl respectively. Moreover, the Tk core is not available without links to various scripting languages. Where Tcl-Tk is the only GUI library available for Tcl, Perl-Tk is not unique for Perl GUI (CPAN). The fact that Perl-Tk was originally designed to be linked with Tk, makes it preferable to software packages linking Perl with Qt, GTK, and Wx.

3 Aims of the project

The primary aim of the project was to develop an automated procedure for morphometric analysis of neurons in culture. It was planned to develop algorithms and subsequently software for automatic tracing of neuronal processes (neurites) and for cell counting. Cell cultures of primary hippocampal and cerebellar granule neurons immunostained for a neuronal marker, GAP-43, were used in the study. Finally, the results obtained using automated recognition algorithms were compared with results obtained by using a semi-automated stereological approach, in order to estimate the accuracy of the developed automated method.

The secondary aim of the project was to implement a set of computer programs targeted at various aspects of manual and automatic extraction of statistical data from recorded images of neuronal cultures. The aspects include estimation of neurite lengths, and extraction of cell morphology and motility. A set of generic software toolkits developed within the project for the efficient implementation of user interface and image processing applications, was used as a basis for the programs.

4 Materials and methods

4.1 Cell cultures

Cultures of dissociated hippocampal neurons were prepared from embryonic day 18 Wistar rats as previously described (Maar et al., 1997; Rønn et al., 2000). Cultures of dissociated cerebellar granule neurons (CGN) were prepared from 7-day-old rats as previously described (Ditlevsen et al., 2003). The neurons were plated at a density of 7000 cells/cm^2 in non-coated eight-well-Permanox Lab-Tek chamber slides (NUNC, Roskilde, Denmark) in Neurobasal medium containing 20 mM HEPES, 100 units/ml peniciline, 100 μg/ml streptomycin (all from Gibco BRL, Paisley, UK), and 0.4% w/v bovine serum albumin (BSA, Sigma-Aldrich, Copenhagen, Denmark) supplemented with B27 (Gibco BRL).

4.2 Neurite outgrowth assay

Cultures of hippocampal neurons and CGN were grown for 24 h at 37^{0}C in a humidified atmosphere of 5% CO_2. The cells were fixed with 4% (v/v) formaldehyde and immunostained using polyclonal rabbit antibodies against rat GAP-43 (Chemicon Int., Temecula, CA, USA), and secondary Alexa Fluor goat anti-rabbit antibodies (Molecular Probes, Leiden, Netherlands). Images of 150-200 cells were captured for each group in each experiment using systematic random sampling as previously described (Rønn et al., 2000) by computer-assisted fluorescence microscopy using a Nikon Diaphot inverted microscope with a Nikon Plan 20 x objective (Nikon, Tokyo, Japan), a Videotech BZT video-camera (Grundig Electronics, Nurnberg, Germany) and the software package Prima developed at the Protein Laboratory (Copenhagen, Denmark). Images were stored as 768 x 576 pixel GIF images with an 8-bit grayscale intensity resolution and a spatial resolution of 0.41 μm/pixel. The neurite length was estimated using two alternative methods, stereological

analysis and automated image processing.

4.3   Image analysis

4.3.1   Stereological procedure

The recorded images were analyzed using the software package PrLenS developed at the Protein Laboratory essentially as previously described (Rønn et al., 2000). A test grid containing a certain number of horizontal lines (usually six to ten) within an unbiased counting frame was superimposed onto images of the cell cultures. Each intersection of a neuronal process (neurite) with a line was marked by means of a computer mouse. The number of cells was also counted by marking neuronal cell bodies located within the borders of the counting frame. The neurite length per cell was calculated using the equation

$$L = \frac{1}{2C}\pi T N \qquad (4.1)$$

where L is the absolute length of neurites (μm), T is the vertical distance between the test lines used, C is the number of neurons and N is the number of neurite intersections. Estimates of neurite length obtained using the described stereological procedure have been reported to correlate well to estimates obtained using manual tracing of neurites (Rønn et al., 2000).

4.3.2   Automated image processing

Neurites appear as a network of thin ridge structures with or without gaps, connected or not connected to the cell body. The procedure for automated image processing is based on the use of a ridge filtering algorithm as well as skeletonization and blob extraction algorithms. The ridge filter algorithm is a combination of directional second derivatives of the two-dimensional Gaussian function:

$$(\mathbf{n} \cdot \bigtriangledown)^2 G \qquad (4.2)$$

where $\mathbf{n}$ is the filter direction, and

$$G(x,y) = \frac{1}{2\pi\sigma^2}e^{-\frac{(x^2+y^2)}{2\sigma^2}} \qquad (4.3)$$

where σ is the standard deviation of the normal distribution. Here, the local ridge direction is determined by the direction $\mathbf{n}$ of a filter which gives a maximum response when applied to the image.

A single-scale Gaussian ridge detector proposed by Lindeberg (Lindeberg, 1998) is formulated to include influence of Gaussian blobs on the detection output, so the detection of both types of structures proceeds simultaneously:

$$\mathcal{N} = t^4(L_{xx} + L_{yy})((L_{xx} - L_{yy})^2 + 4L_{xy}^2) \tag{4.4}$$

where L terms are directional second derivatives of the image scale t

$$t = \sigma^2 \tag{4.5}$$

$$L(\cdot; t) = G(\cdot; t) * f \tag{4.6}$$

and $\mathcal{N}$ is a measure of ridge strength on image f. Application of the filter produces an image with significantly higher intensity values in pixels situated at ridges and center of blobs.

The pixels with intensity values near the average of the image background are discarded, and the image is binarized so only the pixels corresponding to the desired features remain:

$$O(x, y) = \begin{cases} 1 & \text{if } I(x, y) > \text{avg}(I(x, y) \in \text{background})) \\ 0 & \text{otherwise} \end{cases} \tag{4.7}$$

where $I(x, y)$ is the pixel value of the filtered image, and $O(x, y)$ is the value of the corresponding pixel as a result of binarization. The process is straightforward since the average value of the image background value in the filtered image is significantly less than the average value of the features (ridges and blobs).

$$\text{avg}(I(x, y) \in \text{background}) \ll \text{avg}(I(x, y) \in \text{features}) \tag{4.8}$$

Further, the binarized image is subjected to subsequent morphologic erosions, corresponding to the magnification scale and average breadth of neurites. The average neurite breadth in pixels is supplied by an expert, where the values is based on the morphology, and the biological variability of the cells, and the magnification at which the image is recorded. The classification of the feature in question is based on this value, and if a feature is broader than the expert-given value, it is considered as a cell body, otherwise as a

neurite. Representative centroids are subtracted from the original skeletonized binarized image, where the resulting 1-pixel wide lines correspond to the neurites in the original grayscale image.

4.4   Peptides and proteins

The P2 peptide, corresponding to a 12-amino acid sequence localized in the second immunoglobulin (Ig) module of the neural cell adhesion molecule (NCAM) and representing a homophilic binding site (NCAM binding to NCAM), was synthesized as a tetrameric dendrimer (P2d) composed of four monomers with the sequence GRILARGEINFK coupled to a lysine backbone as previously described (Soroka et al., 2002).

The oligomeric form of the recombinant mouse S100A4 protein (Novitskaya et al., 2000) was a generous gift from prof. Eugene Lukanidin (Danish Cancer Society, Copenhagen, Denmark).

4.5   Software

Linear regression analysis for statistical evaluation was performed using the R software package (R). Applications were written using the languages Perl (ActiveState; Perl) and C. GCC (GNU) and MSVC (Microsoft) compilers were used for compilation of the C code. Applications were run on the FreeBSD (FreeBSD), Windows 98/NT/2000 (Microsoft), Linux (Linux), OS/2 (IBM) and Irix (SGI) operation systems.

5   Results

In this chapter the experimental results obtained during the study are described. The stereological setup, algorithm details, and comparison of results using the automated recognition algorithm with results collected from human experts are given in Section 5.1. All programs used in the study were implemented in the Perl language, using two software toolkits created by the author, and are described in detail in Section 5.2. Also, a description of programs created during the study used in other research projects at the Protein Laboratory are included.
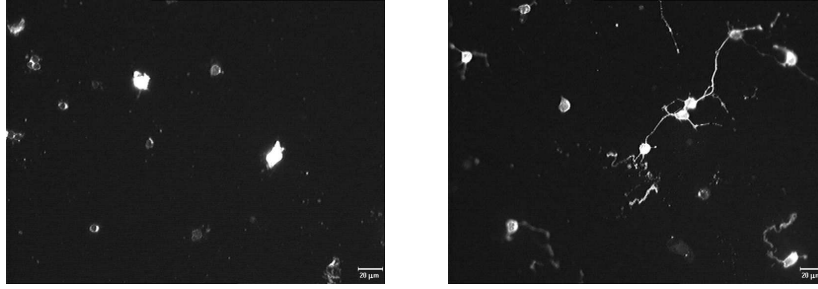
Figure 5.1. Typical microscope images of neurons
On the left: example of an image of neurons without neurites. On the right: example of
an image of neurons with developed neurites.

5.1 Automated quantification of neurite outgrowth

A new computational method for quantification of neurite lengths from microscope
images of cultures of primary neurons was developed. The method is based on a ridge
enhancement and analysis of distribution of pixel intensity in the image. The graphical
user interface and image processing toolkits, and the end-user applications based on these,
were developed so that it is necessary for the user to select two scale selection parameters,
the average neurite width and the minimum cell body area. These parameters are applied
for the processing of a series of images, recorded from experiments, acquired under the
same optical magnification, and using the same type of cell culture.

5.1.1 Object recognition

Neurons and neuronal processes (neurites) as they appear on typical microscope images,
are shown in Figure 5.1. The digital image processing of the images of cultures of primary
neurons begins with the application of a filtering algorithm. The algorithm enhances
Gaussian ridges and blobs, and simultaneously suppresses other features in image. The
ridges and the blobs are extracted from the filtered image, and then processed separately
further, in order to determine whether a particular detected object represents a neurite or
a cell body, respectively.

Spatial sizes of neurites and cell bodies, as they appear on images, directly depend on the
optical magnification used when the images are captured by a video-camera attached to a
microscope. This dependency leads to a differentiation from the Lindeberg's scale selection
scheme, that is optimal when no *a priori* information about the image is available. Here,

the spatial ridge detector operates on a single scale, which may either be set *a priori,* or determined as the scale that yields a maximal specific response of the detector. Figure 5.2 shows an example of an image on different scales, and the results of the ridge detector applied to them.

The result of the ridge detector is then binarized, so that the detected objects appear as groups of pixels with distinct pixel value. Depending on the object area and shape, the objects are further classified either as cell bodies, neurites, or artifacts; the last are discarded at this stage. The objects representing cell bodies and neurites are further mapped into skeletons and blobs, that can be used as estimators of neuritic lengths and number of neurons, correspondingly. The medial axis transform operator implemented as a morphological transform is a fast algorithm, (Ji et al., 1992) and it is applied to the images to convert binary objects into 1-pixel wide representative skeletons.

The binary shapes, containing all the objects detected by the ridge filter, are transformed into a representative set of circles. The centers of the circles, corresponding to the largest blobs are classified as centers of cell bodies. Finally, in the reconstructed image, the lengths of representative skeletons are assumed to be the total neurite length; the areas occupied by cell bodies are excluded from calculations at this stage. The number of detected blob structures are assumed to be the number of neurons.

An example of application of the filtering algorithm on a typical recorded image is shown in Figure 5.3A. The ridge structures corresponding to neurites are extracted from the image (Figure 5.3B) and converted into the representative skeletons (Figure 5.3C). The blob structures corresponding to cell bodies are extracted from the image (Figure 5.3D). The reconstructed image in which the blob structures (cell bodies) and the skeletons of neurites are superimposed is shown in Figure 5.3E.

5.1.2 Effect of the S100A4 protein on neurite outgrowth from primary hippocampal neurons

To validate the automated object recognition procedure for estimation of neurite length, it was compared to a stereological procedure in which neurite outgrowth was estimated by manually marking all neuronal cell bodies and intersections of all neuronal processes with the lines within the counting frame on each retrieved image, taken from each microscopic field via a CCD video-camera. First, as a model system, a primary culture of hippocampal neurons was used. The neurite outgrowth response was induced by treatment of cultures with the S100A4 protein. The S100A4 protein is an efficient neuritogenic

A

B

C

D
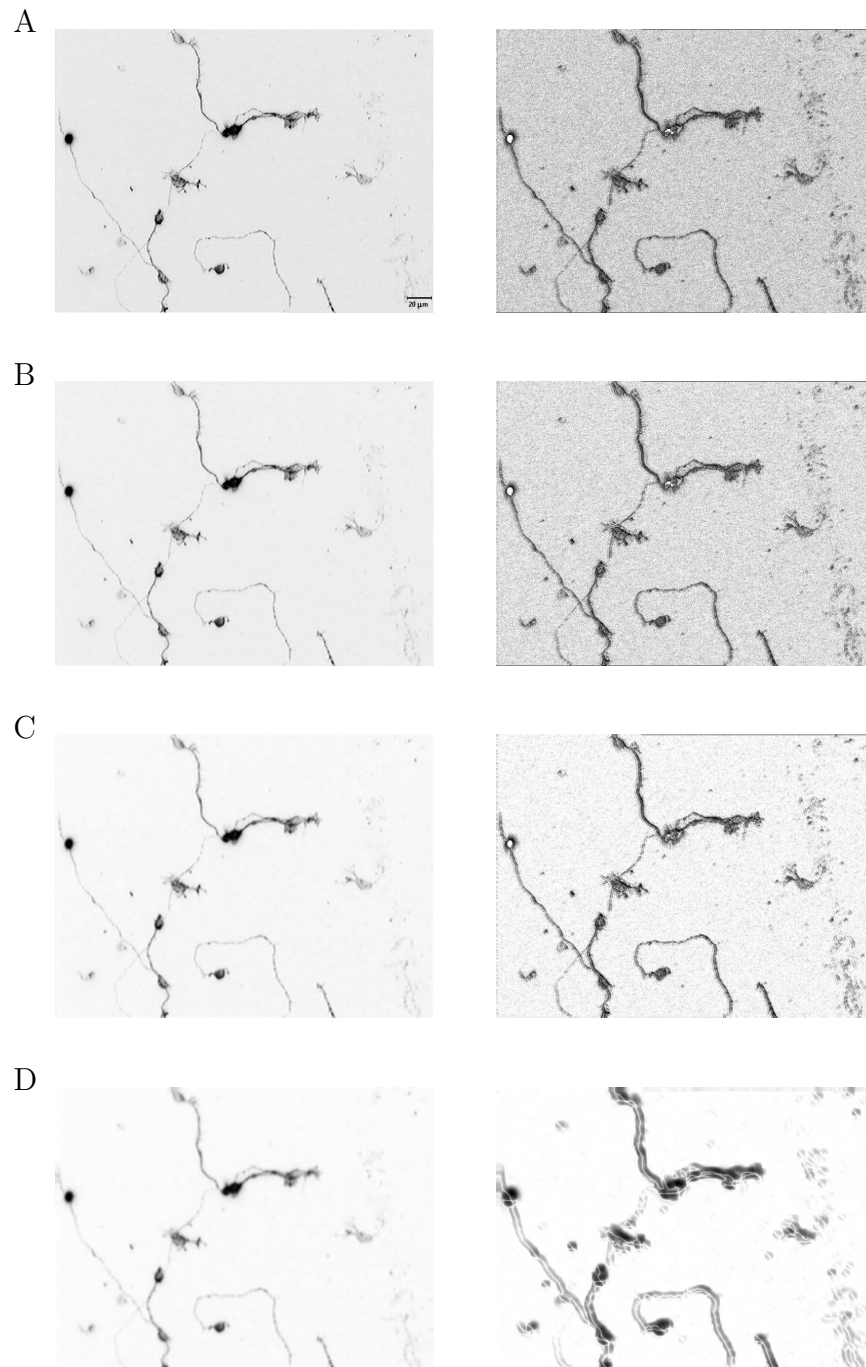
Figure 5.2. Results of application of the ridge detection filter on different scales. The left column contains scales 4,16, and 256 of the original (inverted) image. The right column contains results of the ridge detection filter applied to the corresponding images on the left.
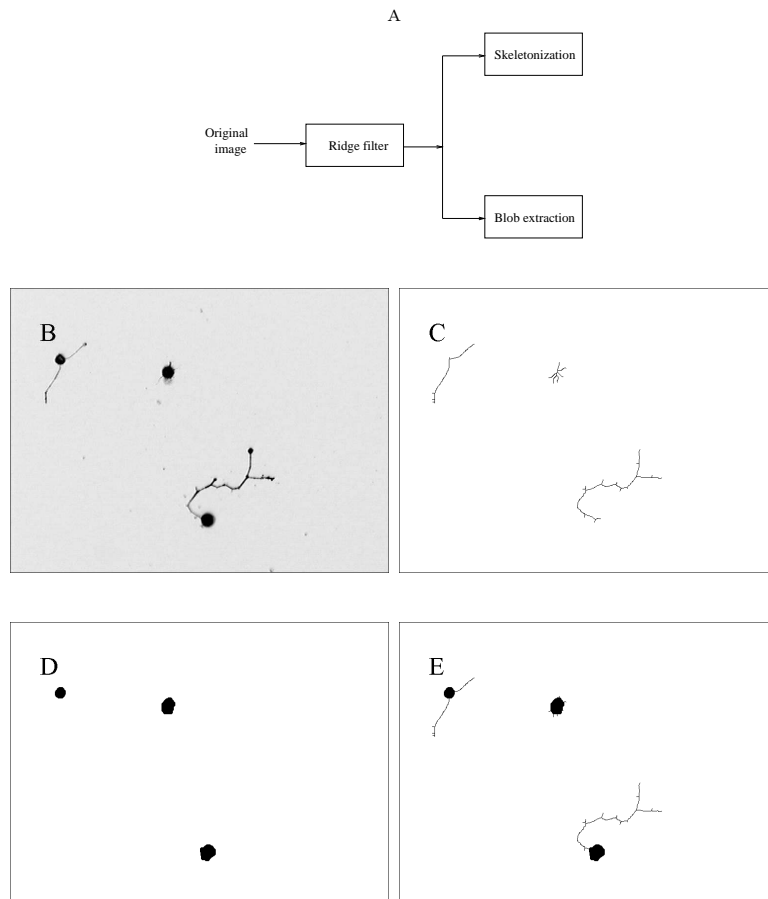
Figure 5.3. Block diagram of the cell body and neurite detection algorithm (A) and illustration of its application (B-E).
B: The original (inverted) image. C: Skeletonization D: Image after the extraction of blobs. E: reconstructed image.

factor which can induce differentiation of hippocampal neurons through the activation of phospholipase C, protein kinase C, and the extracellular signal-regulated kinase (ERK)s 1 and 2. This extracellular function of the protein depends on its aggregation state, since only the oligomeric form, but not the S100A4 dimer has the potential to induce neurite outgrowth (Novitskaya et al., 2000). Cultures of hippocampal neurons were treated with various concentrations of oligomeric S100A4 for 24 h, fixed and immunostained for GAP-43, and recorded images were analyzed using the stereological and automated methods. Oligomeric S100A4 strongly induces neurite outgrowth from hippocampal neurons in a concentration range from 1.25 to 10 μM. The same dose-response profile was obtained using the automated procedure (Figure 5.4A) and the stereological method (Figure 5.4B). However the stereological method gave higher absolute values of neurite lengths (in μm) than the automated procedure. Based on the neurite outgrowth data from four independent experiments, regression lines with 95% confidence limits were plotted to illustrate the correlation between the two procedures for evaluation of neurite outgrowth. From Figure 5.4C it appears that the values of neurite lengths per cell obtained employing the automated approach correlated positively with those obtained using the stereological method (r = 0.82, df = 12, P < 0.001).

5.1.3 Effect of an inhibitor of the FGF receptor, SU5402, on neurite outgrowth from CGN induced by an NCAM mimetic peptide

It was also tested if the automated procedure can be applied for the estimation of neurite outgrowth from other types of neurons. Cultures of cerebellar granule neurons (CGN) were treated with a neuritogenic peptide, P2d. This small peptide is a fragment of the second Ig module of NCAM, which by structural studies has been identified as a part of the homophilic binding site for the first Ig module of NCAM (Soroka et al., 2002). Treatment of hippocampal neurons, CGN and mesencephalic dopaminergic neurons with P2d has been reported to induce a neuritogenic response and to promote cell survival (Soroka et al., 2002; Pedersen et al., 2004). It is also known that NCAM-mediated neurite outgrowth depends on the activation of the FGF-receptor signaling pathway (Kiselyov et al., 2003). Therefore CGN were treated with the NCAM mimetic peptide P2d in a concentration of 0.32 μM and with an inhibitor of FGF-receptor, SU5402, in various concentrations. From Figure 5.5 it appears that SU5402 in a dose-dependent manner inhibited the neuritogenic response of

A

B

C
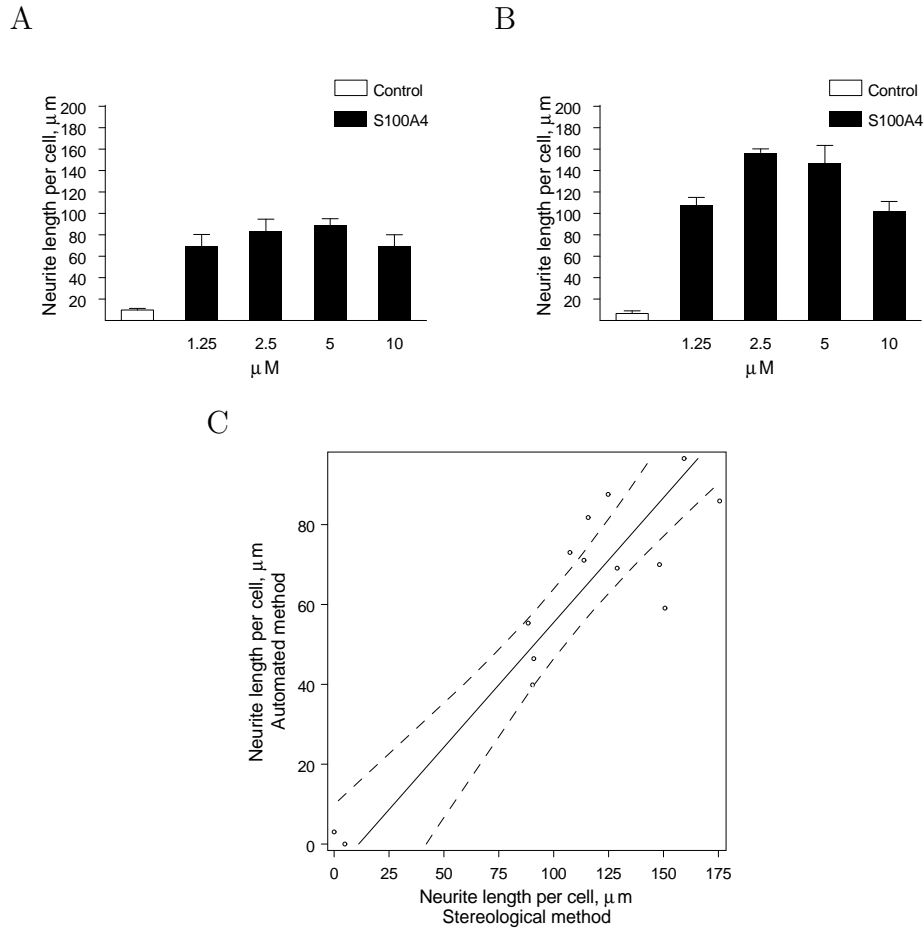
Figure 5.4. Effect of oligomeric S100A4 on neurite outgrowth from hippocampal neurons. The effect is estimated by using the automated procedure (A) and the stereological method (B).Correlation between neurite length determined by automated and stereological methods (C). Hippocampal cells were grown for 24 h in the presence of increasing concentrations of oligomeric S100A4. The oligomeric fraction of S100A4 was obtained by size exclusion chromatography of the recombinant mouse S100A4 as previously described (Novitskaya et al., 2000). Cultures were fixed and immunostained for GAP-43. For each condition in each individual experiment, 40-45 different microscopic fields were recorded. Results from four independent experiments made on separate days are in all cases expressed as a mean ±S.E.M.

CGN to P2d stimulation. The same dose-response profile was observed with the automated procedure (Figure 5.5A) and with the stereological method for evaluation of the neurite length (Figure 5.5B). The stereological method gave slightly higher absolute values of neurite lengths than the automated procedure. In Figure 5.5C it can be seen that the values of neurite length per cell obtained employing the automated approach correlated positively with those obtained using the stereological method (r = 0.909, df = 13, P < 0.001).

5.1.4 Effect of a peptide derived from fibroblast growth factor 10(FGF10), termed 10F10, on neurite outgrowth from CGN

The automated procedure also was tested using series of images obtained by recording experiments in which the effect of a peptide derived from FGF10, termed 10F10, on neurite outgrowth from CGN was investigated. The 10F10 peptide, MYVALNGKGAPRRG, was recently identified an agonist of the FGF receptor-1 (Li et al., manuscript in preparation). From Figure 5.6 it appears that 10F10 strongly induced neurite outgrowth from CGN in a dose-dependent manner. This response was dependent of the activation of the FGF receptor, since the inhibitor of the receptor (SU5402) inhibited neurite outgrowth induced by the 10F10 peptide. The same dose-response profile was obtained using the automated procedure (Figure 5.6 A,C) and the stereological method (Figure 5.6 B,D).

5.1.5 Evaluation of automated estimation of neurite outgrowth

All data from the above-described experiments were combined and regression lines with 95% confidence limits were plotted to assess the correlation between the two procedures for evaluation of neurite outgrowth (Figures 5.7). The estimates of neurite length by the automated and stereological procedures were found to be linearly correlated with correlation coefficients of 0.845 (df = 57, p < 0.0001). Thus, the developed automated method appeared to be an efficient alternative to the semi-manual stereological procedure for the determination of the neurite length.

To further validate the automatic procedures, data measurements of neuritic lengths and the number of cell bodies (neurons) were separately analyzed. The correlation coefficient for neurite lengths and the number of neurons was found to be 0.976 (Figure 5.7B) and 0.808 (Figure 5.7C).
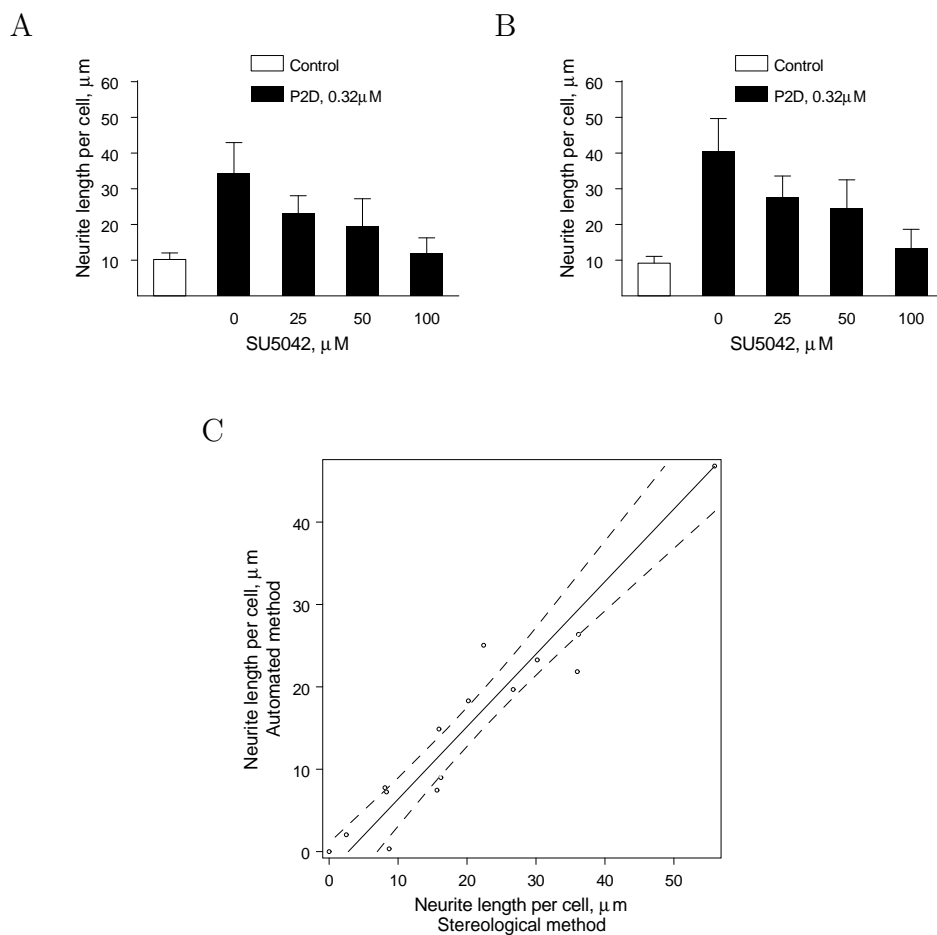
Figure 5.5. Effect of an NCAM mimetic peptide, P2d, on neurite outgrowth from CGN. The effect is estimated by using the automated procedure (A) and the stereological method (B). Correlation between neurite length determined by automated and stereological methods (C). CGN were grown for 24 h in the presence 0.32 μM P2d and increasing concentrations of SU5402. Cultures were fixed and immunostained for GAP-43. For each condition in each individual experiment, 40-45 different microscopic fields were recorded. Results from four independent experiments made on separate days are in all cases expressed as a mean $\pm$S.E.M.
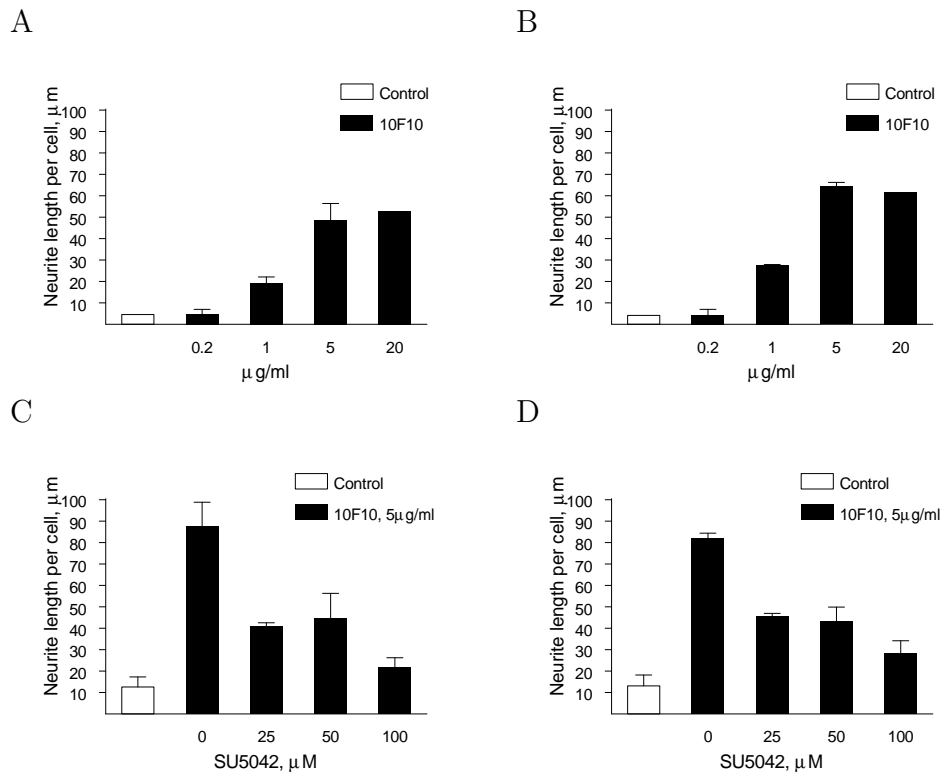
Figure 5.6. Effect of a peptide derived from FGF10, 10F10, and a FGF receptor inhibitor, SU5402, on neurite outgrowth from CGN.

The effect is estimated by using the automated procedure (A,C) and the stereological method (B,D). The dose-response relationship of 10F10 is shown in panel A and B, and the effect of the FGF receptor inhibitor SU5042 is shown in panel C and D. Cultures were fixed and immunostained for GAP-43. For each condition in each individual experiment, 40-45 different microscopic fields were recorded. Results from four independent experiments made on separate days are in all cases expressed as a mean ±S.E.M.
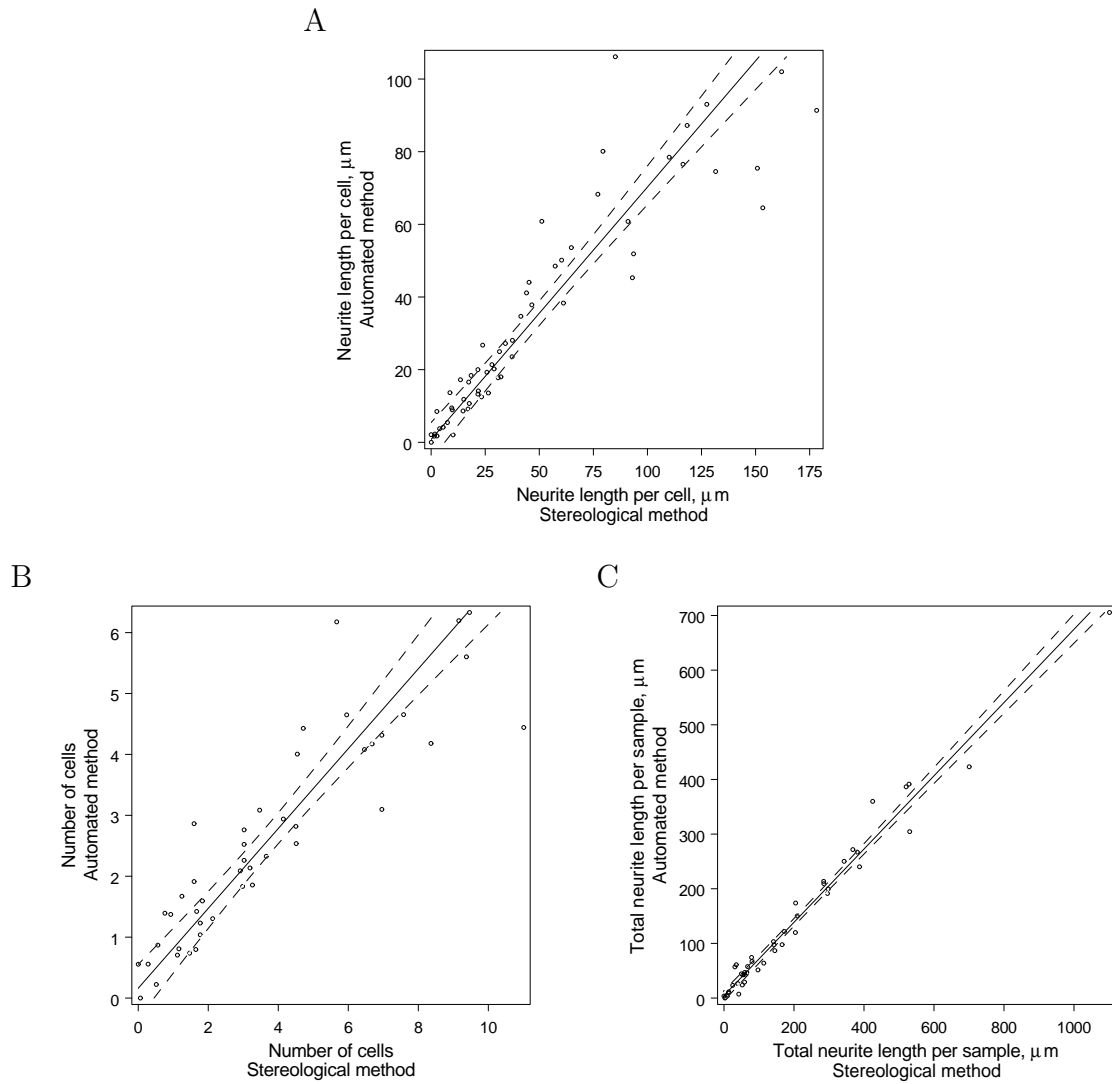
Figure 5.7. Evaluation of automated estimation of neurite outgrowth.
All data presented in Figures 5.4, 5.5, and 5.6 were combined and regression lines with 95% confidence limits were plotted. The graphs reflect the measurements of neurite length per cell (A), number of cells (B) and the total length of neurites (C), respectively.

The differences are attributed to errors of both the algorithm and the human experts. The algorithmic errors arise from a misinterpretation of cell-like bright areas and imprecise neurite tracing on the skeletonization stage. The human experts tend to interpret filopodia, manifested as minor neurite branches, differently. Also, images where cells are entangled with each other cause human experts to disregard weaker features.

The manual measurements were performed on 2106 images from 51 experiments of 20 to 100 images per experiment. The number of analyzed images per experiment was chosen by an expert human analyzer. The number of analyzed cell bodies per experiment was approximately 200.

The automated quantification algorithm was implemented on Perl, whereas individual image processing operators were implemented in C for efficiency. The automated analysis of a typical 768 x 576 image takes less than 3 seconds on a 2.4GHz Pentium IV machine running the FreeBSD operation system.

5.2 A graphical user-interface toolkit and an image processing toolkit

5.2.1 Applications

A number of applications have been developed in Perl for biological research. The applications perform a range of recording, processing, and statistical tasks needed in the laboratory and have been tested on several computers running Windows 98/NT/2000, Linux, FreeBSD, OS/2, and Irix.

The set of programs described below are targeted at different aspects of quantification of recorded images. The programs are designed to perform both manual and automatic extraction of data from the images, and allow the user to modify, load, and save the accompanying data in files. The accompanying data is displayed as superimposed graphics over a selected image. The data format is plain text or XML, and is arranged to be easy readable by both man and machine.

All of the applications share their interface features and are organized as a image displaying panel with menu, toolbar and status panel. The user can adjust various aspects of image and data display in a standard setup dialog.

5.2.1.1 PrLenS: a program for manual and automatic stereological length estimation

PrLenS is a data sampling application capable of both manual and automated stereological estimation of the length of line-like features from recorded images of cells. The application assists the user in quantifying morphological features of a cell culture by employing a stereological method of curve length estimation described in Section 2.2.3.2.

PrLenS's main working area is presented by a frame superimposed on the image, where the user marks intersections of curves of interest within the frame by a computer mouse in the manual mode. As shown in Figure 5.8, the frame consists of parallel equidistant lines in order to obtain uniform sampling of the shape data, and objects are considered according to conventional stereological principles.

The user can work with an arbitrary number of mark sets in order to mark or count objects of interest. Two mark sets are specifically used for selecting objects and features, and used to calculate total normalized curve lengths. PrLenS uses a set of parallel, equidistant
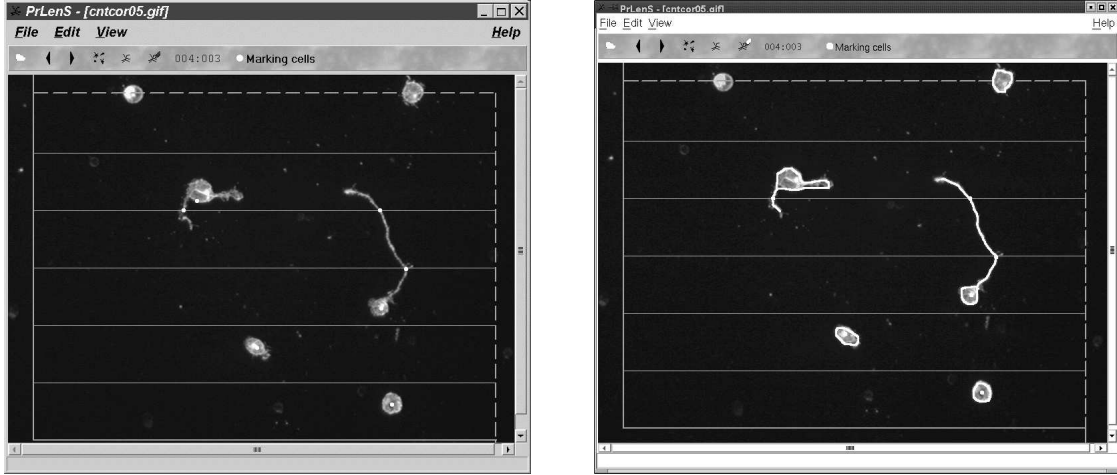
Figure 5.8. Manual and automated sampling of lengths of neurites.
(A) Screenshot of the application, running under MS Windows in manual mode. Centers of cells and crossings of neurites are marked manually by the user. (B) Screenshot of the same application, running under Unix/X11 in automatic mode. The program automatically extracts and outlines centers of the cells and neurites in different colors.

lines superimposed on a curve, and estimates the length of a randomly oriented curve by

$$\hat{L} = \frac{1}{2}\pi TN \tag{5.1}$$

where N is the number of intersections between the lines and curve, $\hat{L}$ is the boundary of the curve, and T is the distance between two parallel lines.

The algorithm of automatic quantification of neurite outgrowth described in Section 5.1.1 is implemented in PrLenS. The user can set up detection parameters and launch bulk quantification of image series inside the program. The PrLenS application has been used for estimation of neuritic lengths in various research projects (Kolkova et al., 2000a; Kolkova et al., 2000b; Ditlevsen et al., 2003; Køhler et al., 2003; Soroka et al., 2003; Neiiendam et al., 2004; Pedersen et al., 2004; Pedersen et al., 2004; Korshunova et al.).

5.2.1.2 MorphometryI: a program for manual and automatic measuring of cell shape

MorphometryI is a data sampling application capable of both manual and automatic extraction of morphological parameters from recorded images of cells (see Figure 5.9).

The parameters are calculated from contours of objects of interest, marked either by the human operator or produced by an image processing algorithm. The user can outline the object contours by means of a computer mouse, or set up application segmentation parameters so that the program performs automatic outlining of features. The program extracts morphological parameters from closed contours and samples as a sequence of n points with corresponding coordinate pairs

$$P_0 = (x_0, y_0), \ P_1 = (x_1, y_1) \ \ldots \ P_{n-1} = (x_{n-1}, y_{n-1}) \tag{5.2}$$

on a cyclic domain where $P_n = P_0$. The following parameters are reported by the application:

- Object area

$$A = |\frac{1}{2} \sum_{i=0}^{n-1} x_i y_{i+1} - x_{i+1} y_i| \tag{5.3}$$

- Object perimeter

$$P = \sum_{i=0}^{n-1} \sqrt{(x_i - x_{i+1})^2 + (y_i - y_{i+1})^2} \tag{5.4}$$

- Object breadth

$$B = \min\{\max\{x_i cos\theta - y_i sin\theta\} - \min\{x_i cos\theta - y_i sin\theta\}|i \in 0..n-1, \theta \in 0..\pi\} \tag{5.5}$$

- Object length

$$L = \max\{\max\{x_i cos\theta - y_i sin\theta\} - \min\{x_i cos\theta - y_i sin\theta\}|i \in 0..n-1, \theta \in 0..\pi\} \tag{5.6}$$

- Object width

$$W = \frac{4A}{\pi L} \tag{5.7}$$

- Object form factor

$$F = \frac{4\pi A}{P^2} \tag{5.8}$$

Convex hull area A_c, convex hull perimeter P_c, convex hull length L_c, and convex hull form factor F_c are calculated by the same equations, but the contour points outline the object
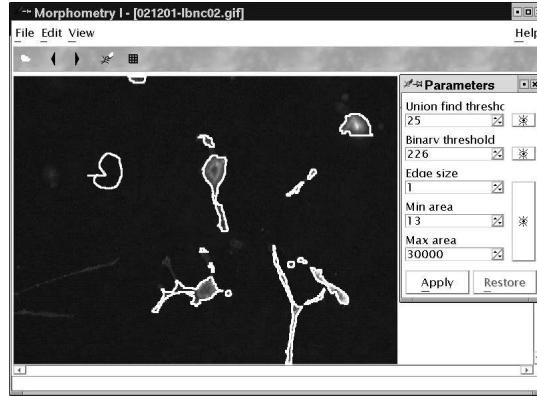
Figure 5.9. The MorphometryI application.
Main image display and automated contour recognition window. The contours outline cells and representative areas of background.

convex hull. These parameters are used to calculate the spreading index

$$SI = \frac{\pi L_c^2}{4 A_c} \qquad (5.9)$$

and bipolarity index

$$BI = \frac{L}{W} \qquad (5.10)$$

The number and area of domains (process index and process domain area, respectively) created by subtracting the object area from the convex hull area are calculated. The MorphometryI program has been used in various cell motility and morphology studies (Tkach et al., 2003; Walmod et al., 2004).

5.2.1.3   ManCen: a cell motility tracking program

ManCen is a motility tracking application and is able to assist the user in tracking objects of interest through series of images (see Figure 5.10). The application was used for a motility evaluation study of fibroblastoid and adenocarcinoma cells by analyzing parameters derived from sampled data. ManCen keeps track of each cell through the series as a sequence of coordinates. The following parameters are extracted (Walmod et al., 2000):

- The mean squared cell displacement after a given time (t_i)

$$\langle d^2(t_i)\rangle = \frac{1}{N(k-i+1)} \sum_{m-1}^{N} \sum_{s-1}^{k} \sqrt{(x_m(t_s) - x_m(t_{s-1}))^2 + (y_m(t_s) - y_m(t_{s-1}))^2}$$

(5.11)

where $i = 0, 1, 2..k$ is the observation number, k is the total number of observations minus one, t_i is the time interval between the initial (t_0) and the i-th observations, $x_m(t_i)$ and $y_m(t_i)$ are coordinates of cell m at time t_i, and N is the total number of cells.

- The mean cell speed, ratio of mean cell displacement $\langle d_\tau\rangle$ to the time interval τ

$$\langle S_\tau\rangle = \frac{\langle d_\tau\rangle}{\tau} = \frac{1}{Nk\tau} \sum_{m-1}^{N} \sum_{s-1}^{k} \sqrt{(x_m(t_s) - x_m(t_{s-1}))^2 + (y_m(t_s) - y_m(t_{s-1}))^2} \quad (5.12)$$

- The mean-cell-path length, for a sample of cell population at a given time

$$\langle L\rangle = \frac{1}{N} \sum_{m-1}^{N} \sum_{s-1}^{k} \sqrt{(x_m(t_s) - x_m(t_{s-1}))^2 + (y_m(t_s) - y_m(t_{s-1}))^2}$$

(5.13)

The locomotive index

$$LI = \frac{\langle d\rangle}{\langle L\rangle}$$

(5.14)

The framework for evaluation of individual-cell motility (Walmod et al., 2000) is based on results acquired with ManCen. Also, the program has been used for cell motility research (Walmod et al., 2004).

5.2.1.4 PrAverB: Average Brightness Estimation

PrAverB is an application for manual assessment of average brightness of rectangular areas in an image. With the application, the user can overlay rotatable and scalable parallelepiped frames over the image and select a binarization threshold over each sub-image, thus masking the area of interest. PrAverB reports pixel area and average brightness of the masked sub-image. The application is employed for quantification of scanned images of gel plates used in blot transfer procedures.

Figure 5.10. The ManCen application.
Manual markings indicate positions of cell centroids in a time series of images.

5.2.2 Prima: a Perl toolkit for graphic user interface

The applications described above were built using the Prima library. Prima is a platform-independent GUI toolkit implemented in C and Perl with an object-oriented interface (Karasik, 2004), running on Unix/X11, Win32, and OS/2 platforms. It provides a Perl implementation of an extensible set of interface elements, standard dialogs, and a Visual Builder program. Having been designed originally for image processing needs, the toolkit also contains basic image processing capabilities.

Prima supports a rich set of operations and transformations applicable to two dimensional arrays of pixels (images) including conversion between the image formats, image scaling, and raster combination. In addition to 1, 4, 8, and 24 bits per pixel formats are supported together with byte, short, long, float, double, and complex pixel types. When an image conversion process involves the down-sampling of pixel data, one of four error distribution algorithms can be selected either automatically or specified by the programmer. Prima can load and save images using many file formats. The exact list the Prima core supports is defined at time of compilation; also, dynamic linking of image file format drivers is supported.

The main goal of Prima is to provide basic windowing and graphics services in a framework of Perl classes. The core classes are implemented in C, and wrapper classes in Perl. Since Prima was planned to run on multiple platforms, the C code is divided into a system-independent and a system-dependent part. All core classes are implemented in a platform-independent fashion, and their hierarchy tree is displayed in Figure 5.11. The standard distribution of Prima includes many Perl classes, which implement a set of interface elements (widgets) expected to be found in any windowing toolkit: buttons, check boxes and radio buttons, input fields, list boxes etc. The complete list of the currently implemented widgets is shown in Figure 5.12.

Prima features a set of classes, whose instances represent graphic interface objects - buttons, scrollbars, and the like. For their on-screen appearance management, the toolkit employs a widespread object-oriented technique, where each interface element draws its visual representation. Contrary to Perl-Tk, which provides rendering of on-screen pixels by a framework of movable and scalable graphic objects (line, circle, etc.), Prima does not rely on concept of graphic objects for visualization. Instead, each interface object controls its appearance by issuing explicit calls to draw graphic primitives inside the special *onPaint* callback routines. Although Perl-Tk allows easier management of the on-screen objects, its approach is poorly scalable, when custom clipping regions, screen scrolling, or raster logical
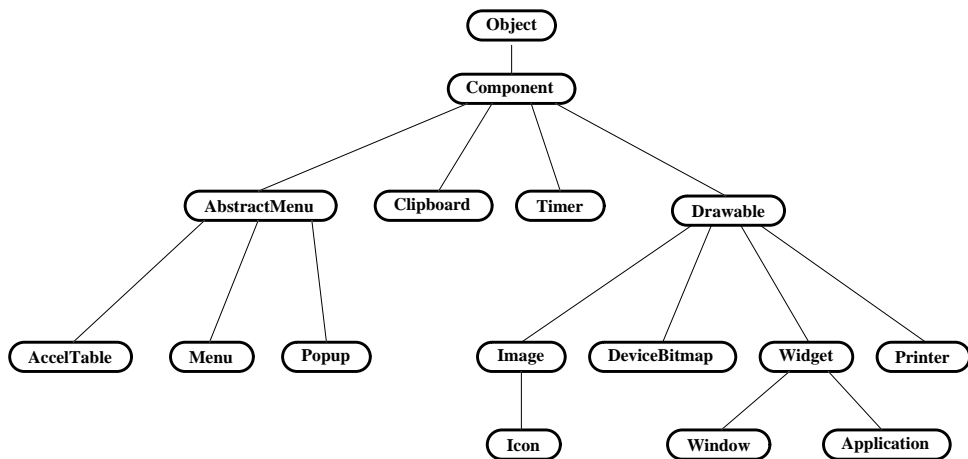
Figure 5.11. The Prima core classes hierarchy
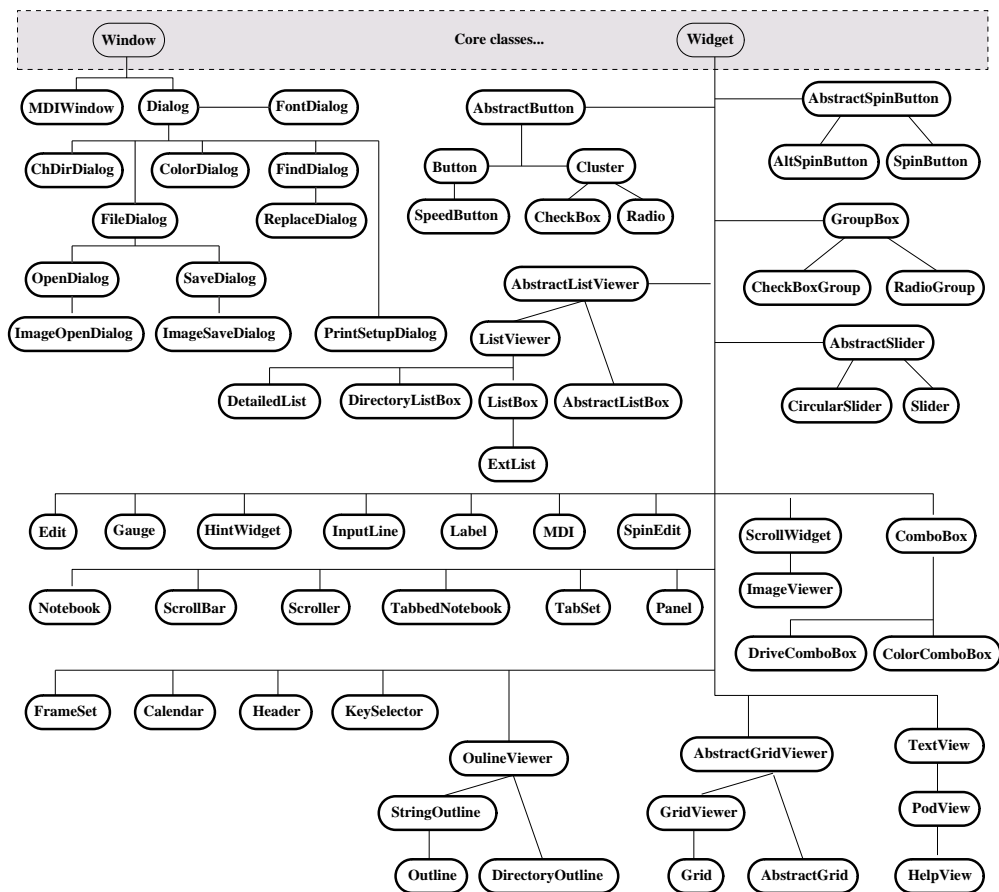
Figure 5.12. The Prima non-core classes hierarchy
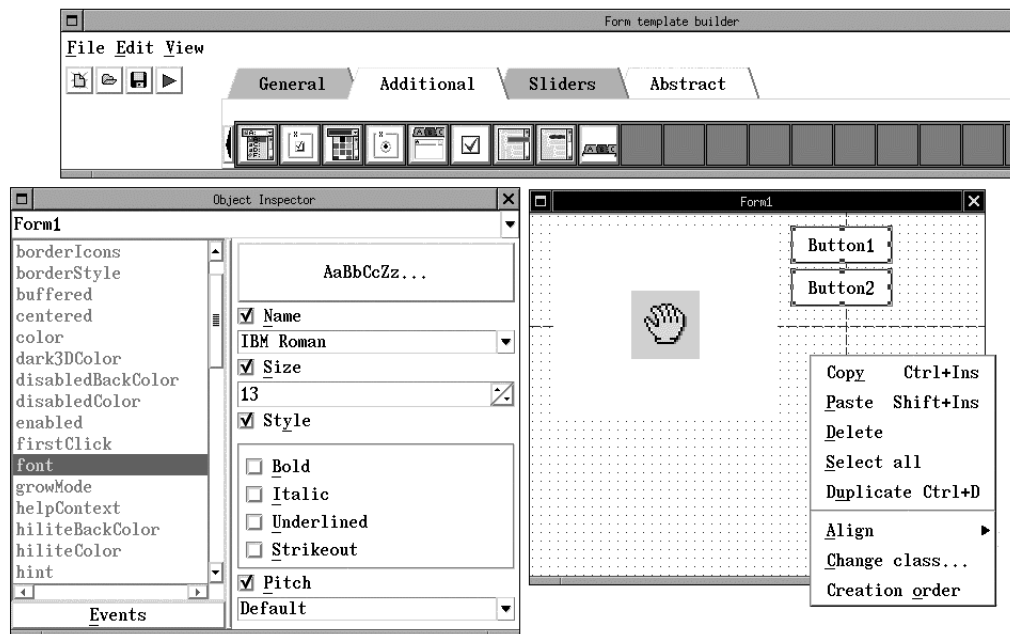
Figure 5.13. A screenshot of Prima Visual Builder

operations are involved, and requires additional C coding in order to access the internal parts of graphic objects' machinery. Furthermore, inability of Perl-Tk to provide direct drawing operation requires a larger body of the toolkit knowledge from the programmer as well as limiting one to C coding. In contrast, the Prima toolkit was implemented so that additional C programming is possible but unnecessary, and the amount of information not available from Perl is kept to a minimum.

A list of unique features of Prima includes pure-Perl implemented interface elements, an image conversion subsystem, and a visual builder (see Figure 5.13). The Perl implementation of sophisticated interface elements, like a HTML browser, is not prohibitively expensive, given the speed of modern day computers. Such an implementation is (arguably) easier to develop and support in Perl than in C or C++, and in particular, a Perl implementation saves the expenses of debugging eventual memory corruption and leaks, intrinsic to the low-level language implementations.

5.2.3 IPA: a Perl toolkit for image processing

IPA is an image processing toolkit based on Prima functionality, and it provides a set of common two-dimensional operators. It complements the Prima toolkit with image processing functions, and it is designed to be portable and platform-independent. IPA features a set of basic processing operators widely described in the literature (Levine et al., 1985; Pratt et al., 1991; Russ, 1995; Sonka et al., 1998) and grouped in modules by the type of algorithms involved. In terms of implementation, most of the basic operators are divided in categories "point", "local", "global", after the area span that affects each particular pixel in the image output. The respective operators are collected under corresponding namespaces, and additionally mathematical morphology operators are grouped under the namespace `Morphology`.

Similarly to many numerical packages, IPA provide a minimalistic interactive shell, `iterm`, which is a combination of a command line with an image viewer window. Its usage primarily concerns interactive exploration of image processing operators, although the shell is capable of parsing and executing the full spectrum of Perl language constructions. IPA can be linked together with the PDL using a connector package `PDL-PrimaImage` (Karasik, 2003).

All IPA algorithms were implemented in C in order to gain efficiency. The input and output of 2D pixel arrays and allocation routines are delegated to the `Prima::Image` class implemented in the Prima toolkit. The class provides storage to pixel data and image attributes: Array dimensions, pixel bit depth, number of channels, pixel memory layout, and color index array (palette) for eventual image visualization. IPA internally employs `Prima::Image` functions that provide image re-sampling and data conversion between various integer and floating-point pixel formats.

The IPA functionality is summarized below, including namespaces, implementation, and details of image processing algorithms. Functions registered in the namespaces `IPA::Point`, `IPA::Local`, and `IPA::Morphology` are supplied with formulations of corresponding algorithms or implementation details.

5.2.3.1 IPA::Point

The module contains functions that perform single point transformations and simple image arithmetics. Single-point processing techniques determine pixel value in the output image from the value of the corresponding pixel in the input image. The process can be

described with the mapping function $o = M(i)$ where o and i are the pixel values in the input and output images O and I, respectively. The following arithmetics is implemented:

- Algebraic summations and *max* function of N images

$$o = \sum_{n=1}^{N} i_n \tag{5.15}$$

$$o = \frac{1}{N} \sum_{n=1}^{N} i_n \tag{5.16}$$

$$o = \sum_{n=1}^{N} |i_n| \tag{5.17}$$

$$o = \sqrt{\sum_{n=1}^{N} i_n^2} \tag{5.18}$$

$$o = \max_{n=1}^{N} i_n \tag{5.19}$$

$$o = \max_{n=1}^{N} |i_n| \tag{5.20}$$

- Algebraic subtractions of two images

$$o = i_1 - i_2 \tag{5.21}$$

- Global thresholding

$$o = \begin{cases} 0 & \text{if } i < i_{min} \cup i > i_{max} \\ 1 & \text{otherwise} \end{cases} \tag{5.22}$$

- Gamma function

$$o = i^{1/\gamma} \tag{5.23}$$

- Gate function of test value t and three inputs

$$o = \begin{cases} i_1 & \text{if } i_0 = t \\ i_2 & \text{otherwise} \end{cases} \tag{5.24}$$

64

A_0	A_1	A_2
A_7	$I(x,y)$	A_3
A_6	A_5	A_4

Figure 5.14. Numbering convention for 3x3 pixel addressing

- Non-adaptive histogram equalization

$$o = i\frac{\sum_{n=1}^{i} N(n)}{\sum_{n=1}^{max} N(n)} \tag{5.25}$$

where $N()$ is number of pixels at intensity level i.

- Generic mapping table (transfer function) f

$$o = M(i) \tag{5.26}$$

5.2.3.2   IPA::Local

Functions registered in the `IPA::Local` namespace operate in the local vicinity of a pixel, and produce an image where every pixel is dependent on the values of the corresponding source pixel and its neighbours. The process can be formulated as an impulse response function,

$$O = \begin{cases} \mathcal{O}\{I(x,y)\} & \text{if } 1 < x, y < L \\ 0 & \text{otherwise} \end{cases} \tag{5.27}$$

where $\mathcal{O}$ is a spatial linear operator, $L \times L$ is area of neighbourhood for output pixel, I and O input and output images. Many of these are implemented by a convolutions with two-dimensional kernels. In particular, for 3x3 kernels the pixel numbering convention depicted in Figure 5.14 is used.

The following operators are provided:

- Crisping effect

$$\mathcal{O}\{\cdot\} = I(x,y) - \sum_{i=0}^{7} A(i) \tag{5.28}$$

- Sobel edge detector

$$\mathcal{O}\{\cdot\} = \sqrt{G_x(x,y)^2 + G_y(x,y)^2} \tag{5.29}$$

where horizontal and vertical derivatives are computed as

$$G_x = \frac{1}{4}((A_2 + 2A_3 + A_4) - (A_0 + 2A_7 + A_6)) \qquad (5.30)$$

$$G_y = \frac{1}{4}((A_0 + 2A_1 + A_2) - (A_6 + 2A_5 + A_4)) \qquad (5.31)$$

- Canny-Deriche edge detector (Deriche, 1987)

- Convolution with custom kernel K

$$O = I * K \qquad (5.32)$$

- Median filter (Huang et al., 1979)

- Segmentation into S non-overlapping homogeneous regions

$$\bigcup_i^S R_i = I \qquad (5.33)$$

$$|H(R_i) - H(R_j)| > t \text{ for adjacent regions } R_i \qquad (5.34)$$

where H is homogeneity criterion and t threshold. Here, the algorithm is designed for various H, although only average region intensity criterion

$$H = \frac{1}{N} \sum_i^N R \qquad (5.35)$$

is currently implemented.

5.2.3.3 IPA::Morphology

The `IPA::Morphology` namespace contains image processing operators based on concepts of mathematical morphology, which in turns operates with point sets, their connectivity and shape. The result of a morphological operator can be described as

$$O = \Psi(I, B) \qquad (5.36)$$

where Ψ is geometrical transformation or mapping, given by relation of the input image I with a small structuring element B in Euclidean space $\mathcal{Z}^2$. Here structuring elements

are limited to 3x3 kernels and implemented using *min* and *max* operations rather than boolean logic, which makes the functions immediately applicable to the grayscale images as well as to the binary. The following operators are implemented:

- Dilation
$$I \oplus B = \{p : p = i + b, i \in I \text{ and } b \in B\} \tag{5.37}$$

- Erosion
$$I \ominus B = \{p : p + b \in I \text{ for every } b \in B\} \tag{5.38}$$

- Opening
$$I \circ B = (I \ominus B) \oplus B \tag{5.39}$$

- Closing
$$I \bullet B = (I \oplus B) \ominus B \tag{5.40}$$

- Gradient
$$\text{grad}(I) = (I \oplus B) - (I \ominus B) \tag{5.41}$$

- Reconstruction of two binary images I and J
$$\rho_I(J) = \lim_{n \to \infty} \delta_I^{(n)}(J) \tag{5.42}$$

where geodesic (here, limited to I) dilation operator δ of size n of a set J is given as
$$\delta_I^{(n)}(J) = \{i \in I, \exists j \in J, d_I(i,j) \leq n\} \tag{5.43}$$

and $d_I(i,j)$ is the shortest path between points i and j inside I (Vincent, 1993).

- Sequential thinning
$$I \oslash B_{\{(i)\}} = (((I \oslash B_{(1)}) \oslash B_{(2)}) ... \oslash B_{(n)}) \tag{5.44}$$

where
$$I \oslash B = I \backslash (I \otimes B) \tag{5.45}$$

- Generic hit-and-miss transform
$$I \otimes B = \{p : B_1 \subset I \text{ and } B_2 \subset I^c\} \tag{5.46}$$

where B_1 and B_2 two structure elements, matching correspondingly I and its complement I^c.

- Watershed segmentation (implemented after (Vincent et al., 1991))

Where applicable, the operators are implemented for 4- and 8- pixel neighbourhood (as in Table 5.14, considering pixel sets $C_4 = A_{(1,3,5,7)}$ and $C_8 = A_{(0,1,2,3,4,5,6,7)}$, respectively).

In addition to the operators above, set connectivity filtering operators are provided. The boolean filtering criteria

$$o = \begin{cases} 1 & \text{if } f(\aleph_p\{p : p = i \cap b, i \in I, b \in C_{(4 \text{ or } 8)}\}) = \text{ TRUE} \\ 0 & \text{otherwise} \end{cases} \tag{5.47}$$

where $\aleph$ is set size, ranging from 0 to 4 or 8, depending on C, are implemented as sequences of hit-and-miss blocks to be applied to each pixel of I. Each set contains 2^9 boolean elements, representing pre-calculated responses for all combinations of a 3x3 set. The following criteria are defined:

- Isolated point filter

$$f = \aleph_p > 0 \tag{5.48}$$

- Pruning

$$f = \aleph_p > 1 \tag{5.49}$$

- Node break

$$f = \aleph_p < 3 \tag{5.50}$$

5.2.3.4 Other IPA modules

The `IPA::Global` module contains methods that produce images, where the value of each output pixel depends on all input image pixel values, $O = F(I)$. The namespace contains functions implementing Fourier transform and two-dimensional band filter functions, plus a set of topology-based functions for binary images: Area filtering, contour identification, contour fill.

The `IPA::Geometry` module provides geometrical transformation on images: translation, rotation, mirroring. Scaling is not provided as it is supported by the underlying core functionality of the Prima toolkit.

The `IPA::Misc` module contains a set of miscellaneous, non-related functions such as channel splitting and combination routines, and intensity histogram calculation.

6 Discussion

Measurements of neurite length by manual tracking of neurites on retrieved images of video-recorded microscopic fields from cell cultures are the most time-consuming step in analysis of neurite outgrowth. Also, user-related bias is common to manual analysis of images with regard to estimation of neurite length. At Protein Laboratory a stereological method for quantification of neurite length based on stereological principles has been developed, which both simplifies the analysis of neurite outgrowth and dramatically reduces the time of image processing (Rønn et al., 2000). However, the user-introduced bias is still present in the stereological procedure, since an operator needs to mark manually cell bodies and intersections of neurites with the grid built in an unbiased counting frame. In order to avoid the manual component entirely in the determination of neurite outgrowth, an algorithm allowing automatic processing of images of cultures of dissociated neurons was developed, under the condition that neurons are stained with a fluorescent dye (in our case it was GAP-43 immunostaining). The algorithm is based on ridge filtering, skeletonization, and the blob extraction, and automatically yields all information for determination of the number of neurons and the total neurite length. The algorithm was tested using cultures of hippocampal and cerebellar granule neurons treated with neuritogenic compounds by comparing automated vs. stereological determination of neurite outgrowth. In total, more than 2000 images were subjected to the analysis, and a statistically significant linear correlation between the two methods was found, with correlation coefficients ranging from 0.85 to 0.97 in different experiments.

Several of the state of the art algorithms targeted at detection of neurites (and, in general cases, any visible features manifested as ridges or edges) are also based on multi-scale feature detection (Dima et al., 2002; Meijering et al., 2004). To attain a higher degrees of accuracy, one may employ sophisticated detection of additional features inherent to the images (branching points) (Dima et al., 2002) , or resort to hints provided by a hu-

man expert (Meijering et al., 2004). Another recently invented method does not employ the multi-scale approach, but rather depends on the inherent radial direction of cultured neurites (Weaver et al., 2003). An algorithm suitable for automated estimation of the number of attached cells and the neurite length was developed and tested on cultures of dissociated retinal ganglion cells, which were double stained for NCAM (immunofluorescence staining of cells with neurites) and DNA (staining of cell bodies with bisbenzimide) (Treubert et al., 1998). The novelty of our approach was the development of an algorithm that can be used for quantification of neurite outgrowth by digital image analysis of cultures of dissociated neurons stained with only one single fluorescent marker. Employing this algorithm it is shown that the exogenous S100A4 protein in its oligomerized form is a strong inducer of neurite outgrowth from hippocampal neurons. Furthermore, it is demonstrated that an induction of the neuritogenic response in cerebellar neurons by an NCAM mimetic peptide, P2, involves obligatory activation of the FGF receptor.

Image analysis-based quantitative studies that do not involve a human operator are most often unable to reproduce the results of a human expert exactly, although, if compared, the correlation between the results is relatively high. The stereological methods on the contrary do not introduce large bias, but are significantly less productive. The presented method was found to yield results comparable to those obtained by a human expert with a high degree of accuracy, although depending on the type of input the results possess certain deviations. The error tendencies of the neurite detector algorithm are to appear mostly in cell cultures where neurites are absent or relatively short. This is attributed to a high sensitivity of the ridge detector to sharp and irregular boundaries of specific neurites. A possible method to mitigate the effect is to apply weighing to the detector results, where shorter neurites would give lesser impact on the total result. Without the experimental back up though, this approach should be considered as speculative. In contrast, the results of the automated analysis from cell cultures with longer, developed neurons strongly correlate with the human results.

While the method sometimes does not detect neurites that are weakly manifested visually, but recognized by the human eye, or gives false positives in the circumstances described above, the main source of error is not under- or over-detection of neurites, but rather under-detection of cell bodies. The latter occurs mostly when cell bodies overlap, or form a tight conglomerate, but nevertheless are counted as single cell, distorting the normalized (lengths to number of cells) ratio. Although these conglomerates are not representative within the cell model, and strictly speaking, should be omitted by human experts,

they rarely are, so the detection program in practice was forced to deal with these. On the other hand, automatic exclusion of conglomerates from images, as well as a detection of the proper number of cell bodies within conglomerates, both address the same problem, the determination of whether a particular blob consists of one, or more than one, cell body. This problem is acknowledged, but is unsolved within this study. Still, in case further research is to be done, a promising way to tackle the problem is to model and reconstruct 2D structures of cell bodies, accounting for variability of morphology and shape within individual cell models.

The proposed method was tested within a set of constraint conditions, and in particular, neuronal models, experimental conditions, and image acquisition setup and conditions were fixed. This does not mean that the detector algorithm is crafted exclusively for input acquired under these conditions only, since the underlying ridge detection principle is valid on theoretically any image displaying visually discernible neurites, given these are not heavily intertwined. Nevertheless, since the detection experiments were not carried out under other conditions, the presented method may not produce valid results if applied directly to significantly different input, and may therefore require additional pre-processing in order to be adapted to the input.

The comparison between results of manual and automated analysis showed a high degree of correlation. Comparison to the stereological methods, the presented method is faster and requires no active human interaction. The presented method is an efficient and accurate way to estimate lengths of neurons grown *in vitro*, and it can be used for fast estimation of dose-response effect of various substances on neurite outgrowth.

Although the results of the proposed method on an individual image may not match with the results provided by a human expert, or even be erroneous in rare cases, the gross outcome, namely the effect of a substance on the neuronal culture, closely corresponds to the gross results of the expert. Moreover, this outcome was the actual aim of the whole study, primarily because the accuracy of the method is less relevant in the scope of the biological research, targeted at the search of compounds with profound outgrowth acceleration functions, rather than the precise measurement of the effect or reconstruction of neurons. This aspect largely contributes to the principal difference between the state of the art methods and the proposed method.

The software implementation of the detector algorithm within a graphic-user interface program was accomplished in such a fashion so that the resulting set of programs can be run on a wide range of platforms. Also, it was attempted to design the development

process so that parts of the software responsible for the interface and the detection were built using optimal tools for each part, namely the scripting language Perl for the former and C for the latter. The criterion for the implementation of image processing algorithms was defined to be speed of execution, whereas the criterion for the interface and program logic was defined to be speed of development and separation of program logic from the underlying algorithms. As a part of the research, two Perl-C toolkits, Prima and IPA were developed, to provide a common basis for implementation of the user interface and the image processing programs. The set of programs based on Prima and IPA for estimation of neurite lengths, and extraction of cell morphology and motility was implemented within the research. Currently, the two toolkits have grown out of this research into a separate, non-academic domain, and are freely available on the internet.

In conclusion, the present study demonstrates the usefulness of the developed algorithm for automated determination of neurite outgrowth in primary cultures of dissociated neurons stained with a fluorescent dye.

7 Conclusions

1. The automatic quantification of neuritic lengths from microscopy images based on ridge detection is a fast and accurate method for estimation of neurite outgrowth on neuronal differentiation models. Also, it is a promising tool for a larger area of research where quantification of neuritic lengths requires a significant amount of human resources.

2. The platform-independent implementation of automatic quantification program, along with a set of related programs and software development toolkits, is provided.

A Results of automatic detection

Below are examples of the results of automatic detection of neurites and cell bodies, performed by the PrLenS program. Images on the left (inverted) are the original microscopy images recorded by Z.Li, a sub-set of images recorded from experiments of cells treated by the of 10F10-d peptide and the SU5402 inhibitor. Images on the right contain composite responses of the detector program as regards cell centroids and neurites. The magnification coefficient is constant in all images.

81
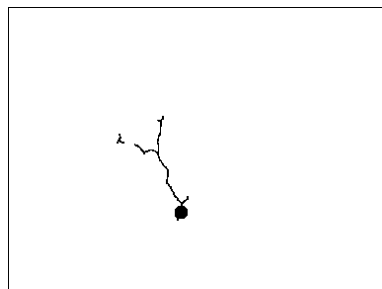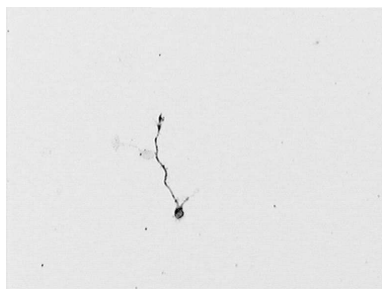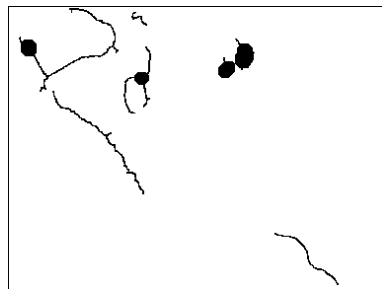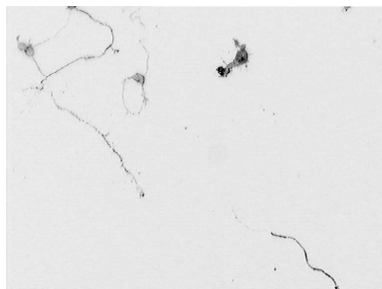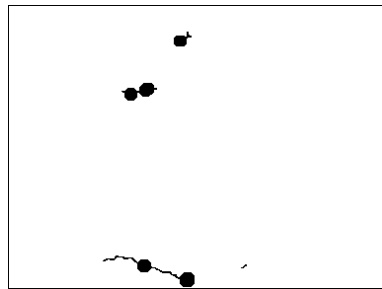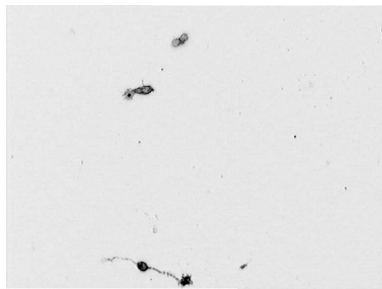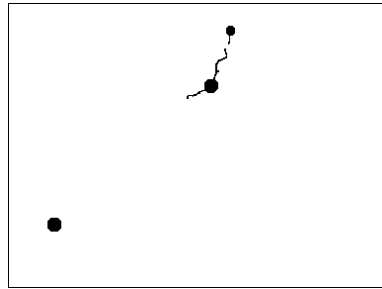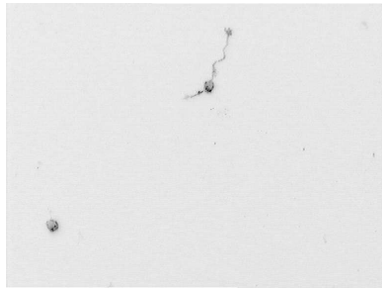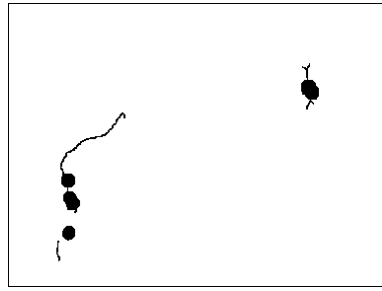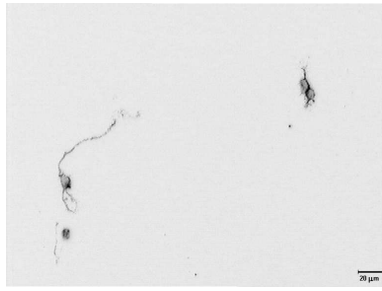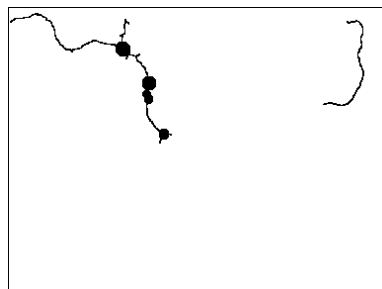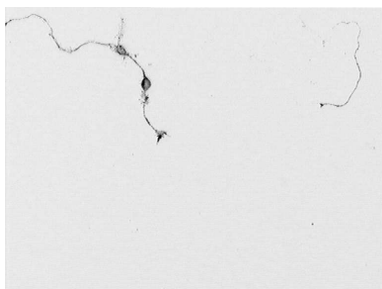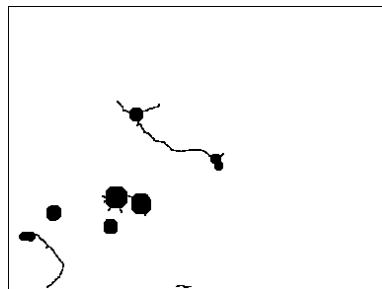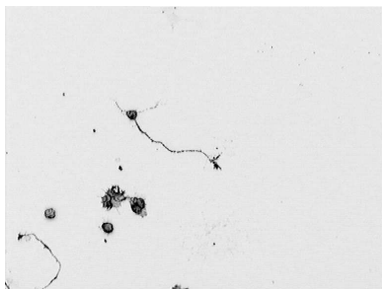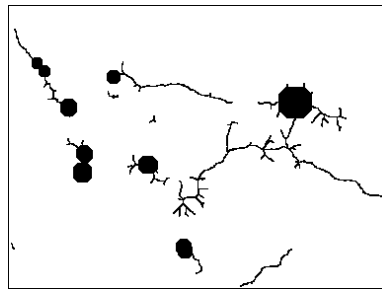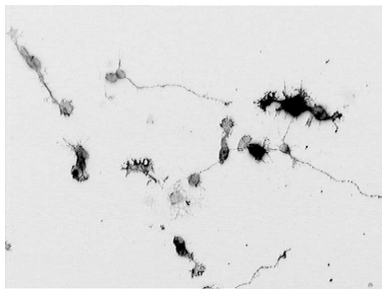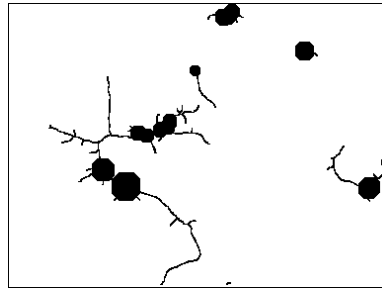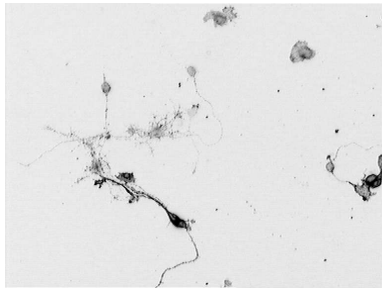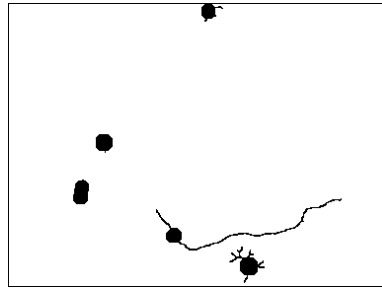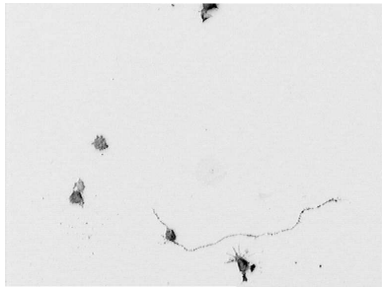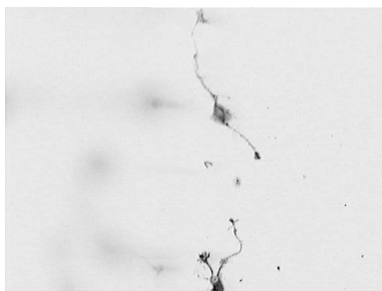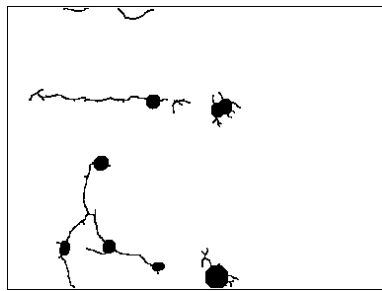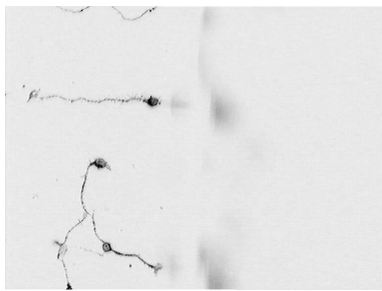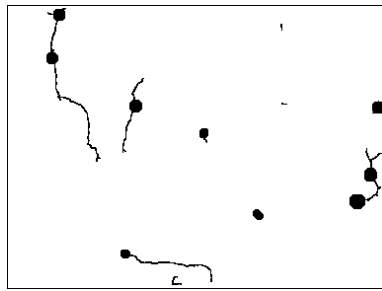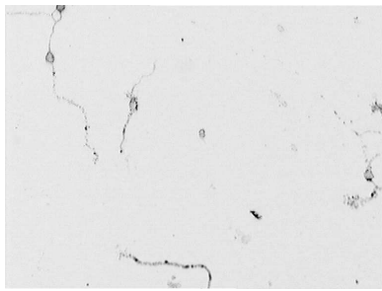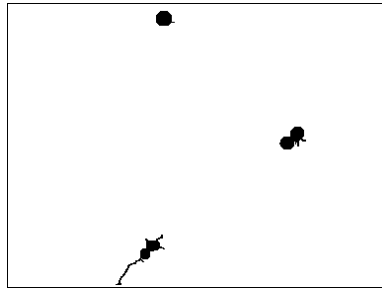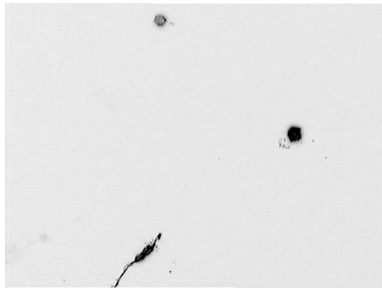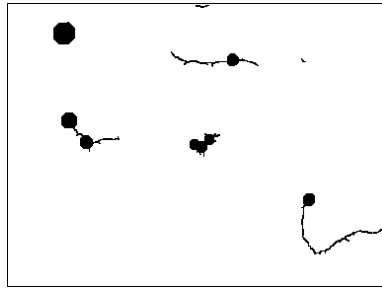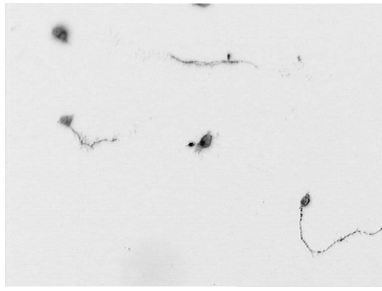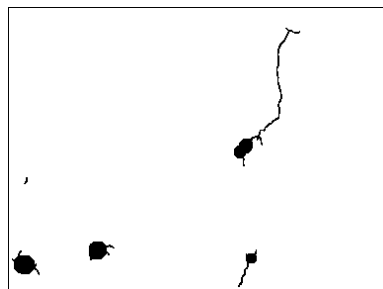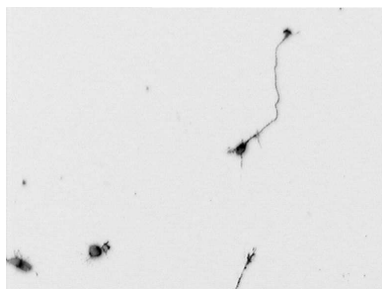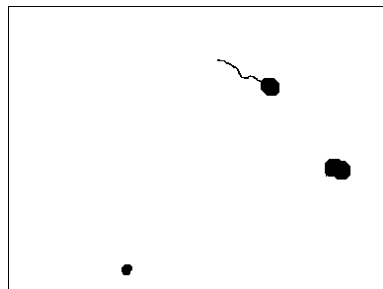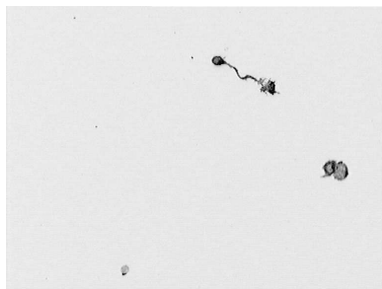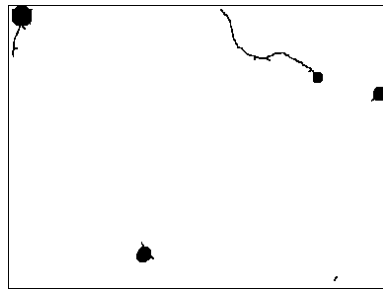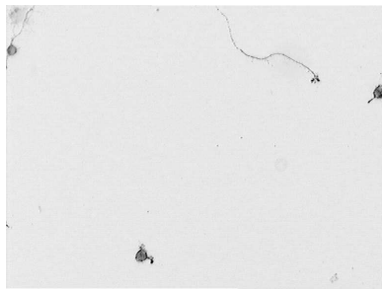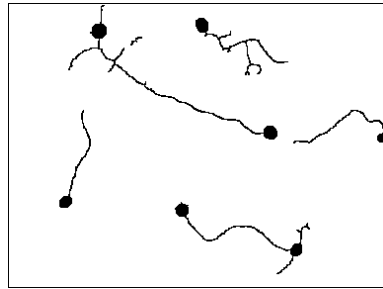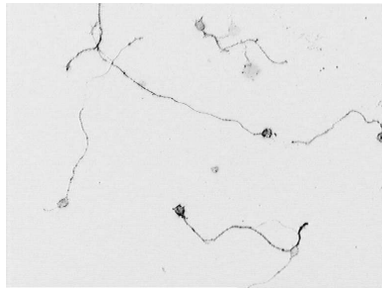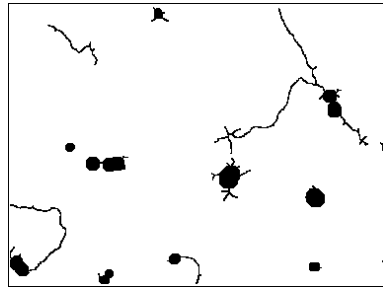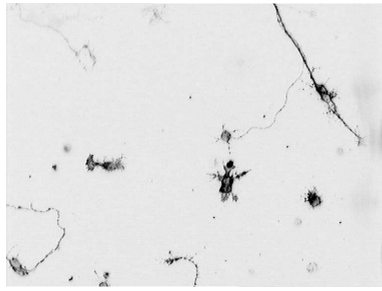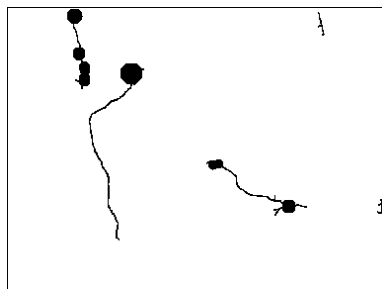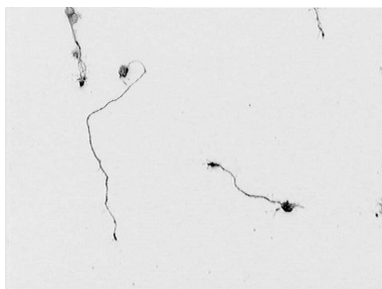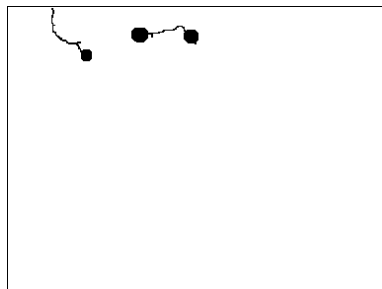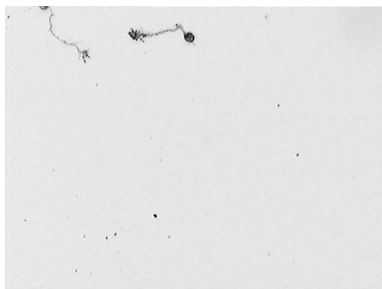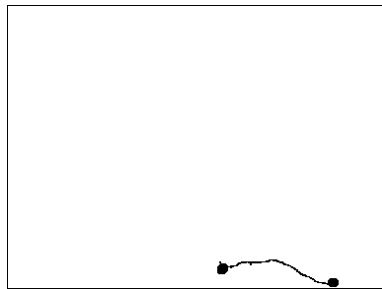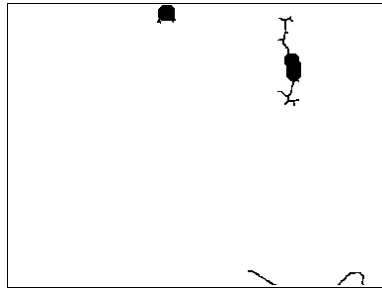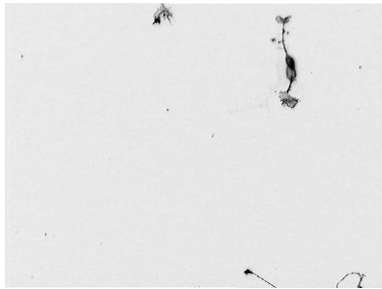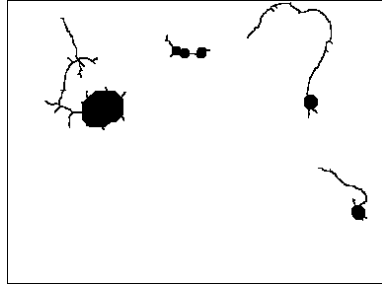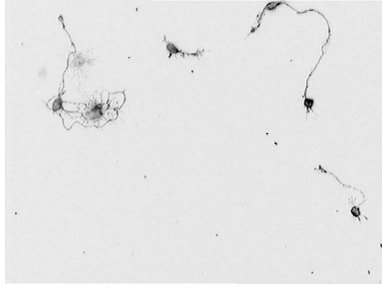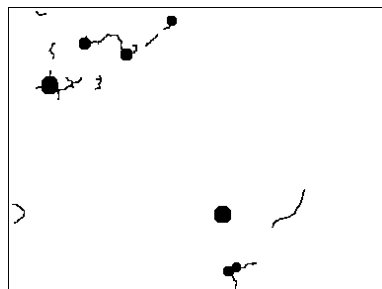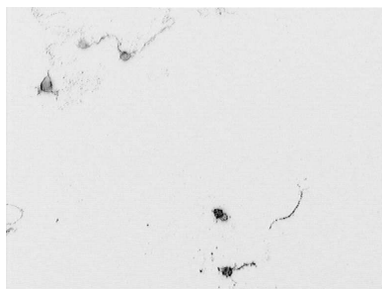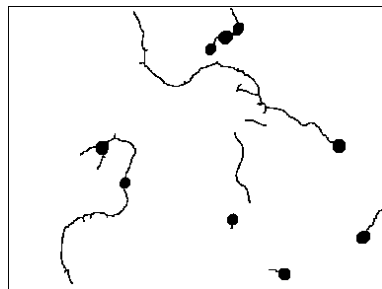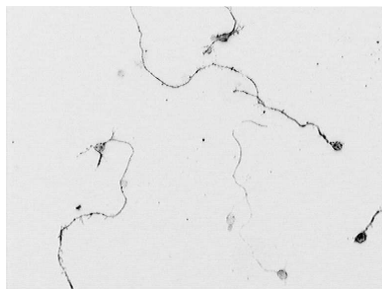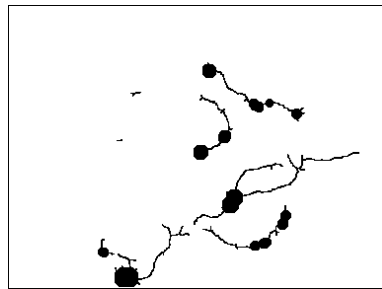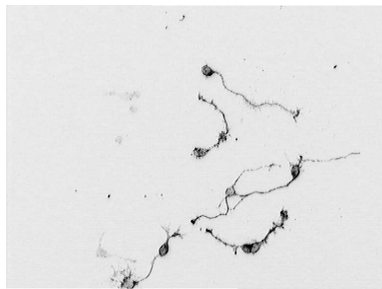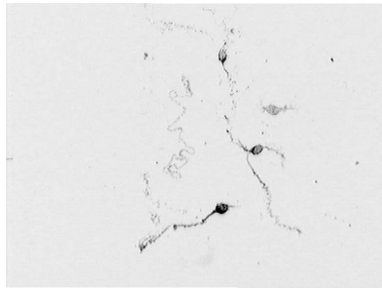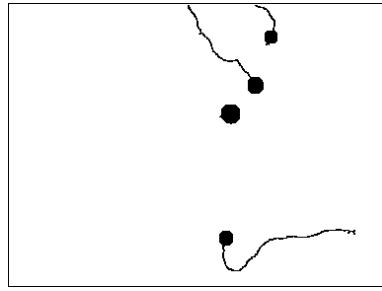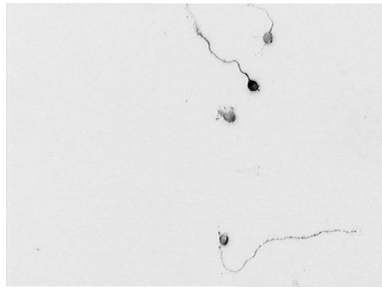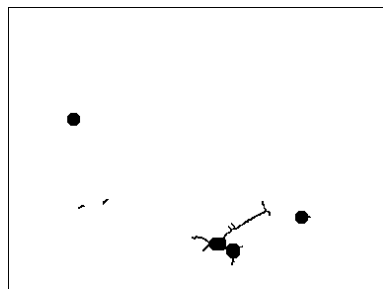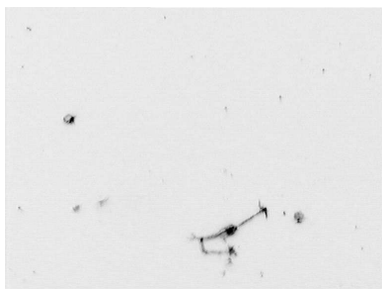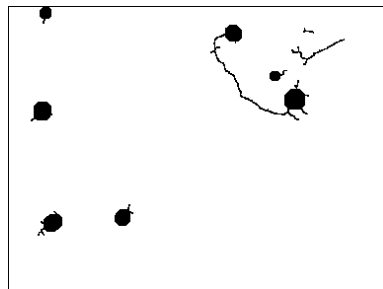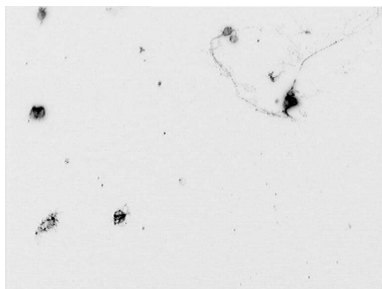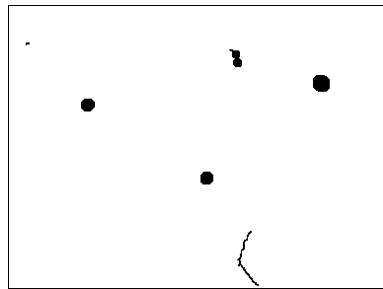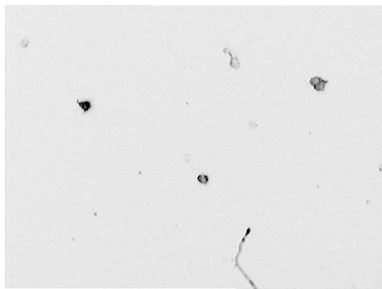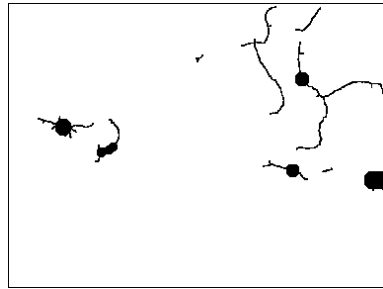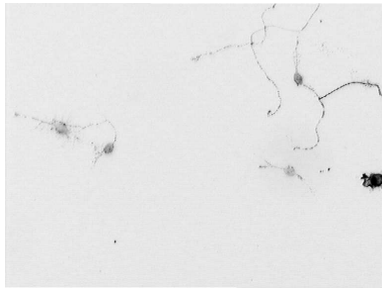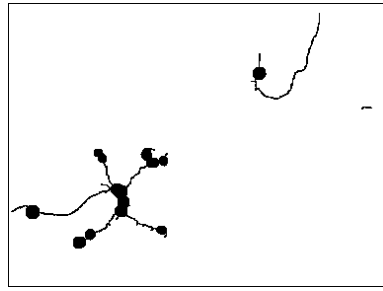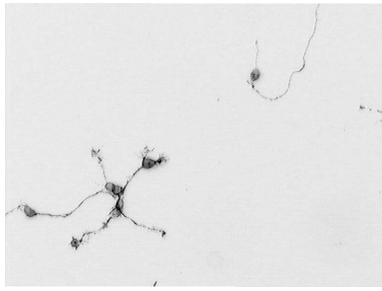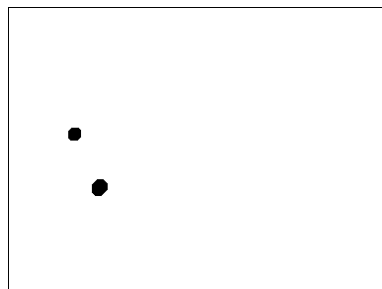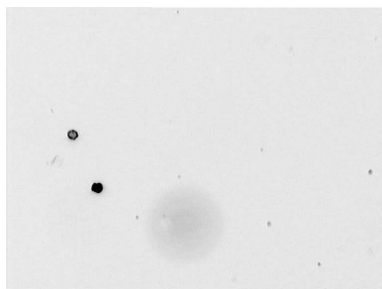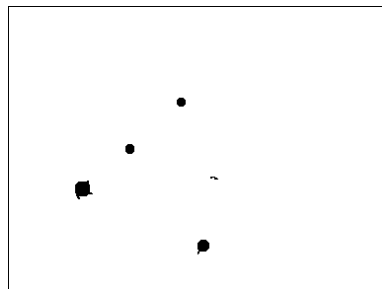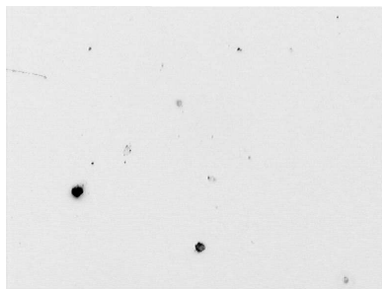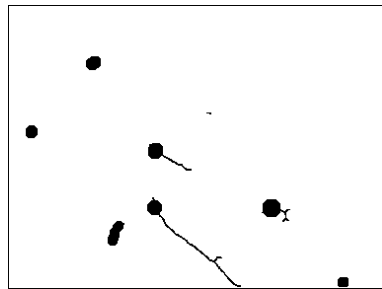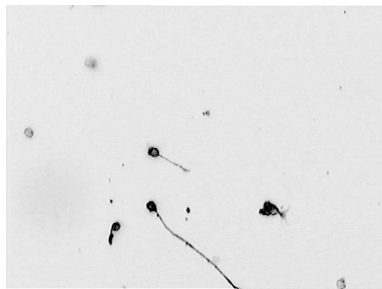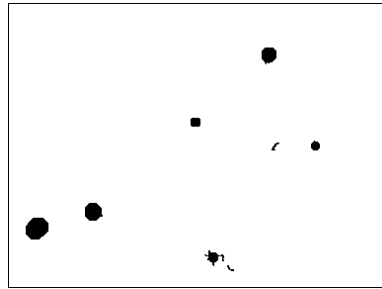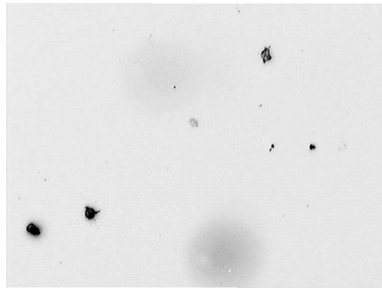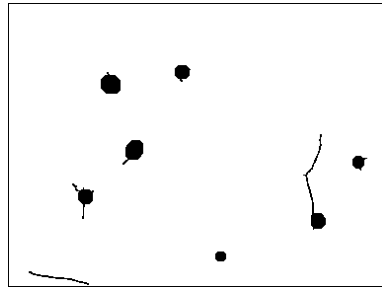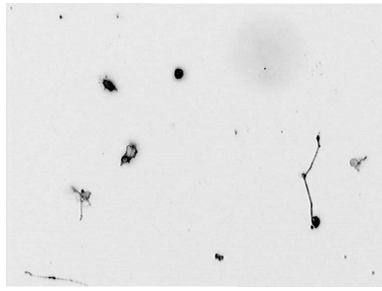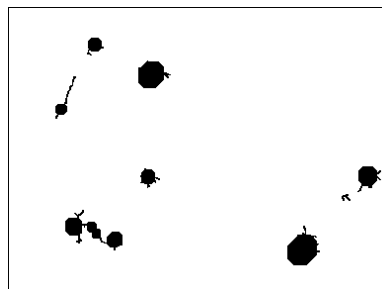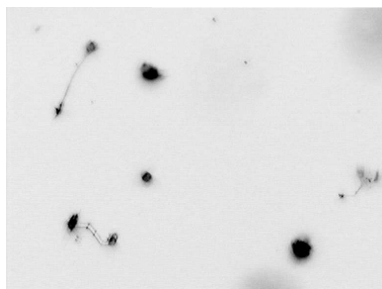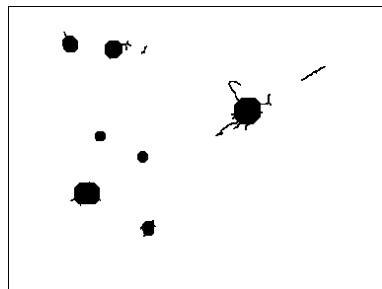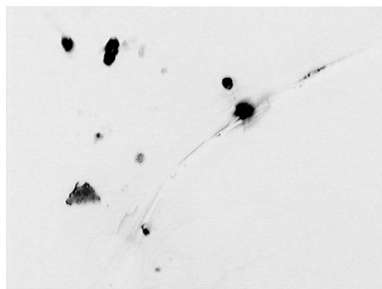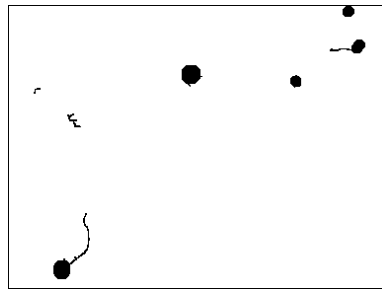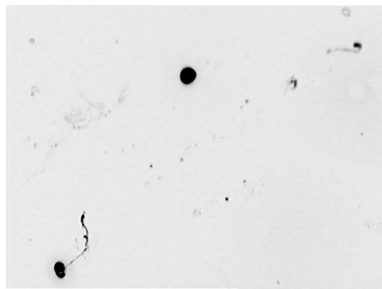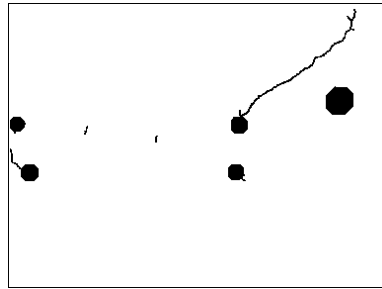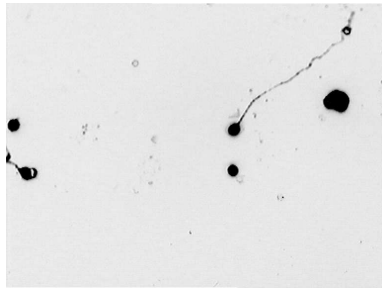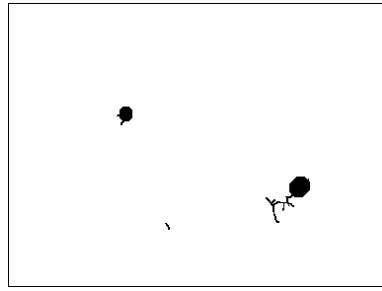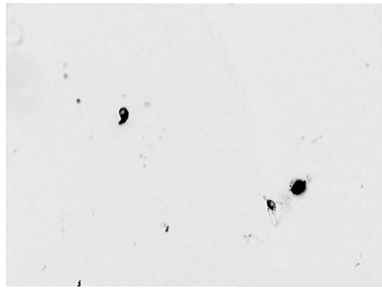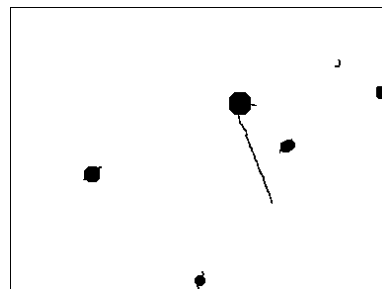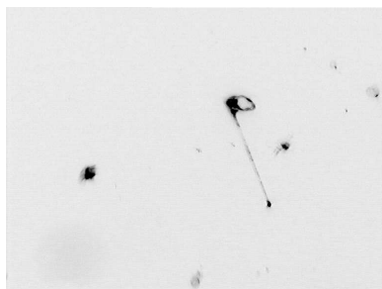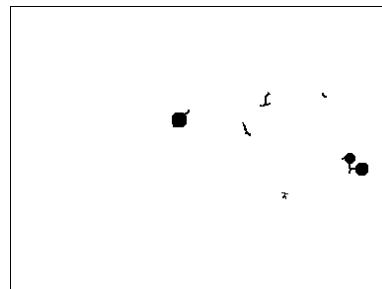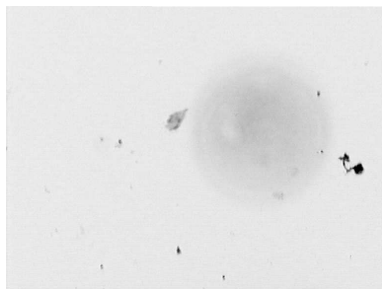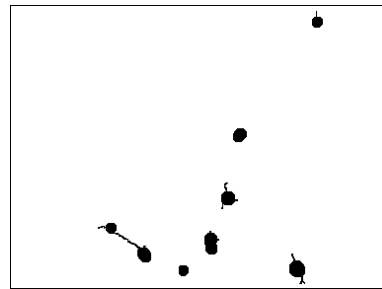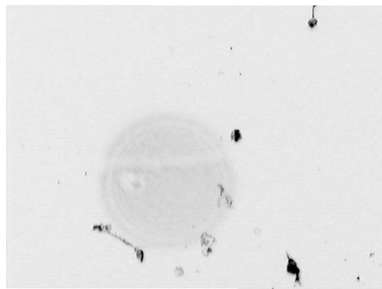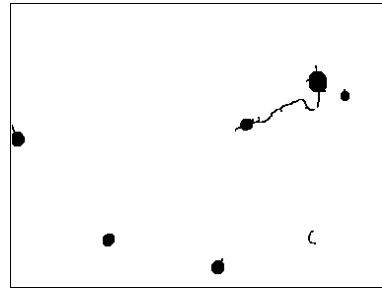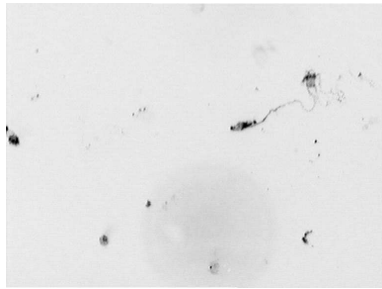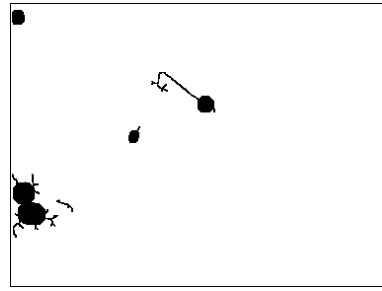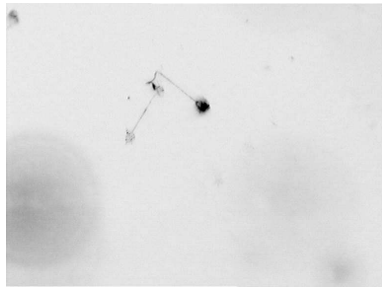
B   Experimental data

The tables contain averaged data for each experiment, extracted by a human expert and the PrLenS program. The experimental data are marked 'control', where no substances were added, and otherwise with concentration of substances. Each value is an average from 20 to 50 images recorded in a single experiment. The number of images analyzed by a human expert is the same as the number of images analyzed by the program in each experiment.

Legend:

- CH - number of cell bodies, as calculated by a human expert

- PH - length of neurites in μm, as calculated by a human expert using the stereological method

- RH - averaged length of neurites, PH/CH.

- CM - number of cell bodies, as extracted by the detector program.

- PM - length of neurites in μm, as extracted by the detector program

- RM - averaged length of neurites, PM/CM.

The plots of the data in rows RH and RM are displayed in Figures 5.4, 5.5 and 5.6. The columns reflect the first, second, and third experiment, respectively, under the same experimental setup, where available. The other columns contain average values of all experiments under the same setup, and standard error of means, when there is data from more than one experiment.

```
C3d-amide


Control      Exp.#1    Exp.#2    Exp.#3    Average    SEM
CH            3.333                          3.333     0.000
PH           33.757                         33.757     0.000
RH           10.127                         10.127     0.000
CM            4.033                          4.033     0.000
PM           66.407                         66.407     0.000

RM           16.465                         16.465     0.000



0.2µg/ml
CH            2.500                          2.500     0.000
PH           37.460                         37.460     0.000
RH           14.984                         14.984     0.000
CM            3.513                          3.513     0.000
PM           70.380                         70.380     0.000

RM           20.035                         20.035     0.000



1µg/ml
CH            2.667    1.800                 2.233     0.433
PH           61.537   41.836                51.686     9.851
RH           23.076   23.242                23.159     0.083
CM            3.493    2.120                 2.806     0.686
PM           56.225   35.915                46.070    10.155

RM           16.095   16.941                16.518     0.423



5µg/ml
CH            3.333    2.020                 2.676     0.656
PH           82.455   68.084                75.269     7.185
RH           24.737   33.701                29.219     4.482
CM            4.983    2.677                 3.830     1.153
PM           76.368   55.730                66.049    10.319

RM           15.325   20.820                18.072     2.748



20µg/ml
CH            1.738                          1.738     0.000
PH            2.490                          2.490     0.000
RH            1.433                          1.433     0.000
CM            2.675                          2.675     0.000
PM           13.143                         13.143     0.000

RM            4.913                          4.913     0.000
```

```
10F10-d and SU5402


Control     Exp.#1     Exp.#2     Exp.#3    Average     SEM
CH           8.696      3.509      3.383      5.196     1.750
PH          27.429     69.902     54.786     50.706    12.429
RH           3.154     19.922     16.193     13.090     5.083
CM           6.435      3.158      2.917      4.170     1.135
PM          32.722     66.989     33.388     44.366    11.313

RM           5.085     21.213     11.447     12.582     4.690



5μg/ml 10F10-d
CH          12.750      4.721      8.696      8.722     2.318
PH        1104.015    370.643    703.047    725.902   212.014
RH          86.589     78.511     80.850     81.983     2.400
CM           6.562      3.953      5.217      5.244     0.753
PM         714.912    281.071    432.608    476.197   127.121

RM         108.939     71.094     82.916     87.650    11.178



5μg/ml 10F10-d, 25μM SU5402
CH           8.417      4.930     11.111      8.153     1.789
PH         383.223    211.576    533.100    375.966    92.887
RH          45.531     42.914     47.979     45.475     1.462
CM           6.292      4.256      7.722      6.090     1.006
PM         276.465    159.583    313.896    249.981    46.473

RM          43.941     37.498     40.648     40.696     1.860



5μg/ml 10F10-d, 50μM SU5402
CH          11.200      4.762     10.100      8.687     1.988
PH         522.955    145.463    531.255    399.891   127.237
RH          46.692     30.547     52.600     43.280     6.591
CM           8.450      4.643      6.300      6.464     1.102
PM         395.951    106.857    400.932    301.247    97.205

RM          46.858     23.015     63.640     44.504    11.786



5μg/ml 10F10-d, 100μM SU5402
CH           5.205      3.407     10.895      6.502     2.257
PH         168.571     56.277    389.704    204.851    97.947
RH          32.386     16.519     35.770     28.225     5.934
CM           5.205      3.542      8.316      5.688     1.399
PM         107.131     51.869    249.608    136.203    58.904

RM          20.582     14.642     30.016     21.747     4.476
```

```
10F10-d


Control    Exp.#1    Exp.#2    Exp.#3    Average    SEM
CH          2.899                          2.899    0.000
PH         12.030                         12.030    0.000
RH          4.150                          4.150    0.000
CM          2.928                          2.928    0.000
PM         13.314                         13.314    0.000

RM          4.548                          4.548    0.000


0.2µg/ml
CH          2.299     3.509                2.904    0.605
PH         16.029     5.243               10.636    5.393
RH          6.973     1.494                4.234    2.739
CM          2.989     3.351                3.170    0.181
PM         20.800     9.417               15.108    5.692

RM          6.960     2.810                4.885    2.075


1µg/ml
CH          2.985     3.571                3.278    0.293
PH         81.274    99.610               90.442    9.168
RH         27.227    27.891               27.559    0.332
CM          3.791     3.714                3.752    0.038
PM         83.752    60.873               72.313   11.439

RM         22.092    16.389               19.240    2.851


5 µg/ml
CH          6.452     4.762                5.607    0.845
PH        427.361   298.041              362.701   64.660
RH         66.241    62.589               64.415    1.826
CM          6.548     4.881                5.715    0.833
PM        369.344   200.802              285.073   84.271

RM         56.402    41.140               48.771    7.631


20µg/ml
CH          4.651                          4.651    0.000
PH        287.249                        287.249    0.000
RH         61.758                         61.758    0.000
CM          4.209                          4.209    0.000
PM        222.901                        222.901    0.000

RM         52.954                         52.954    0.000
```

```
P2d and SU5402


Control    Exp.#1    Exp.#2    Exp.#3    Average    SEM
CH          4.762     2.857     5.395     4.338    0.763
PH         52.177    15.284    60.290    42.584   13.849
RH         10.957     5.349    11.176     9.161    1.907
CM          4.381     2.825     4.447     3.884    0.530
PM         53.758    18.534    52.281    41.524   11.503

RM         12.271     6.560    11.755    10.195    1.824


0.32μg/ml P2d
CH          5.882     5.000     6.250     5.711    0.371
PH        345.707   147.755   206.484   233.315   58.697
RH         58.770    29.551    33.037    40.453    9.214
CM          5.059     3.975     4.656     4.563    0.316
PM        259.606    96.152   129.355   161.704   49.880

RM         51.317    24.189    27.781    34.429    8.507


0.32μg/ml P2d, 25μM SU5402
CH          7.407     3.206     8.200     6.271    1.550
PH        287.763    61.136   207.190   185.363   66.326
RH         38.848    19.067    25.267    27.727    5.841
CM          8.296     2.857     6.200     5.784    1.584
PM        218.692    38.562   183.283   146.846   55.098

RM         26.360    13.497    29.562    23.140    4.909


0.32μg/ml P2d, 50μM SU5402
CH          7.692     3.865     6.242     5.933    1.116
PH        300.108    44.697   143.882   162.896   74.341
RH         39.014    11.563    23.049    24.542    7.960
CM          6.769     3.423     4.939     5.044    0.967
PM        209.012    16.602   112.691   112.768   55.544

RM         30.877     4.850    22.815    19.514    7.692


0.32μg/ml P2d, 100μM SU5402
CH          6.281     2.254     9.318     5.951    2.046
PH        116.212     6.442   175.073    99.242   49.413
RH         18.501     2.859    18.788    13.383    5.262
CM          6.125     2.343     6.773     5.080    1.381
PM         73.324    10.572   131.305    71.734   34.862

RM         11.971     4.512    19.387    11.957    4.294
```

```
S100 A4


Control     Exp.#1    Exp.#2    Exp.#3    Average    SEM
CH           5.306     4.515               4.910    0.396
PH          47.653    18.446              33.050   14.603
RH           8.982     4.085               6.534    2.448
CM           5.417     4.455               4.936    0.481
PM          44.732    50.308              47.520    2.788

RM           8.258    11.294               9.776    1.518


1.25μM
CH           5.049     5.907     5.692     5.549    0.258
PH         562.839   696.243   537.783   598.955   49.179
RH         111.480   117.868    94.475   107.941    6.981
CM           5.951     5.814     5.872     5.879    0.040
PM         483.745   461.245   282.513   409.168   63.660

RM          81.285    79.334    48.114    69.578   10.747


2.5μM
CH           5.805     4.310     5.390     5.168    0.446
PH         948.863   656.164   834.136   813.054   85.150
RH         163.460   152.259   154.749   156.823    3.396
CM           6.707     5.095     6.000     5.934    0.467
PM         703.077   398.705   404.110   501.964  100.569

RM         104.822    78.251    67.352    83.475   11.128


5μM
CH           5.286     4.907     5.024     5.072    0.112
PH         681.198   881.565   668.118   743.627   69.072
RH         128.875   179.655   132.975   147.168   16.286
CM           5.762     6.093     5.659     5.838    0.131
PM         552.205   573.854   437.719   521.259   42.235

RM          95.837    94.182    77.355    89.125    5.904


10μM
CH           5.214     4.073     5.000     4.762    0.350
PH         624.541   376.576   475.107   492.075   72.082
RH         119.775    92.453    95.021   102.416    8.711
CM           5.119     1.829     4.976     3.975    1.074
PM         460.896   116.347   272.106   283.116   99.615
RM          90.035    63.603    54.688    69.442   10.613
```

References

Abercrombie M. Estimation of nuclear population from microtome sections. Anat. Rec. 1946, 94: 239-247

ActiveState Perl. http://www.activestate.com/Products/ActivePerl/

Alberts B, Bray D, Lewis J, Raff M, Roberts K, Watson JD. Molecular biology of the cell. 2nd edition. ISBN 0-8240-3965-6. Garland Publishing Inc. 1989.

Ambatsurmian NS, Grigorian MS, Larsen IF, Karlstrøm O, Sidenius N, Rygaard J, Georgiev G, Lukanidin E. Metastasis of mammary carcinomas in GRS/A hybrid mice transgenic for the mts1 gene. Oncogene 1996 :1621-1630

Andersen BB, Gundersen HJG, Pakkenberg B. Aging of the human cerebellum: a stereological study. J. Comp. Neurol. 2003, 466:356-365

Andersen H, Mahmood S, Tkach V, Cohn M, Kustikova O, Grigorian M, Berezin V, Bock E, Lukanidin E, Tulchinsky E. The ability of Fos family members to produce phenotypic changes in epithelioid cells is not directly linked to their transactivation potentials. Oncogene 2002, 21:4843-4848

Archer FR, Doherty P, Collins D, Bolsover SR. CAMs and FGF cause a local sub-membrane calcium signal promoting axon outgrowth without a rise in bulk calcium concentration. Eur. J. Neurosci. 1999, 11:3565-3573

Ballard DH. Generalizing the Hough transform to detect arbitrary shapes. Patt. Rec. 1981, 13:111-122

Barber PR, Vojnovic B, Kelly J, Mayes CR, Boulton P, Woodcock M, Joiner MC. Automated counting of mammalian cell colonies. Phys. Med. Biol. 2001, 46:63-76

Barrett WA, Mortensen EN. Interactive live-wire boundary extraction. Med. Image Anal. 1997, 1:331-341

Barron D. The world of scripting languages. John Wiley & Sons, 2001. ISBN 0471998869

Benes FM, Lange N. Two-dimensional versus three-dimensional cell counting: a practical perspective. Trends Neurosci. 2001, 24:11-17

Benes FM, Lange N. Reconciling theory and practice in cell counting. Trends Neurosci. 2001b 2:378-380.

Berezin A, Karasik D, Belman V, Berezin V, Bock E. Prima - Perl toolkit for X, win32, & OS/2 PM. Proceedings of the Open Source Convention, August 1999, Monterey CA.

Berezin V, Bock E. NCAM mimetic peptides: pharmacological and therapeutic potential. J. Mol. Neurosci. 2004, 22:33-40

Bezdek JC. Pattern recognition with fuzzy objective function algorithms. New York: Plenum, 1981

Bhattacharyya A, Oppenheim RW, Prevette D, Moore BW, Brackenbury R, Ratner N. S100 is present in developing chicken neurons and Schwann cells and promotes motor neuron survival in vivo. J. Neurobiol. 1992, 23:451-466

Bilsland J, Rigby M, Young L, Harper S. A rapid method for semi-quantitative analysis of neurite outgrowth from chick DRG explants using image analysis. J. Neirosci. Methods. 1999, 92:75-85

Blake A, Isard M. Active contours. Springer, 1988.

Blanchette J, Summerfield M. C++ GUI Programming with Qt 3. ISBN 0-13-124072

Brownlee H, Gao PP, Frisen J, Dreyfus C, Zhou R, Black IB. Multiple ephrins regulate hippocampal neurite outgrowth. J. Comp. Neurol. 2000, 425:315-322

Brummendorf T, Kenwrick S, Rathjen FG. Neural cell recognition molecule L1: from cell biology to human hereditary brain malformations. Curr. Opin. Neurobiol. 1998, 8:87-97. Review

Canny JF. Finding edges and lines in images. Technical Report 720, MITAIL 1983

Canny JF. A computational approach to edge detection. IEEE Trans. Pat. Anal. Mach. Intell. 1986, 8:679-698

Cassel CM, Särndal CE, Wretman JH. Foundations of inference in sampling. Malabar, FL: Krieger 1993

Chan TF, Vese LA. An active contour model without edges. Int. Conf. Scale-Space Theories in Computer Vision. 1999, 16:266-277

Choung PH, Seo BM, Chung CP, Yamada KM, Jang JH. Synergistic activity of fibronectin and fibroblast growth factor receptors on neuronal adhesion and neurite extension through extracellular signal-regulated kinase pathway. Biochem. Biophys. Res. Commun. 2002, 295:898-902

Coggeshall RE, Lekan HA. Methods for determining number of cells and synapses: a case for more uniform standards of reviews. J. Comp. Neurol. 1996, 364:6-15

Colchester ACF. Network representation of 2D and 3D images, in 3D Imaging in Medicine (eds) Hoehne KH, Fuchs H, Pizer S. Springer-Verlag, Berlin, 1990:45-62

Comprehensive Perl Archive Network. http://search.cpan.org/modlist/ User_Interfaces

Connor JA. Digital imaging of free calcium changes of spatial gradients in growing process in single, mammalian central nervous system cells. Proc. Natl. Acad. Sci. USA. 1986, 83:6179-6183.

Crossin KL, Chuong CM, Edelman GM. Expression sequences of cell adhesion molecules. Proc. Natl. Acad. Sci. USA. 1985, 82:6942-6946

Crowley JL, Parker AC. A representation for shape based on peaks and ridges in the difference of low-pass transform. IEEE Trans. PAMI 1984, 6:156-170

Cruz-Orive LM. Systematic sampling in stereology. Bull. Internat. Statist. Inst. 1993, 50:451-468

Cruz-Orive LM. Precision of Cavalieri sections and slices with local errors. J. Microsc. 1999, 193: 182-198

Deriche R. Using Canny's criteria to derive a recursively implemented optimal edge detector. Int. J. Comp. Vis., 1987:167-187

Desire L, Courtois Y, Jeaunny JC. Suppression of gibroblast growth factors 1 and 2 by antisense oligonucleotides in embryonic chick retinal cells in vitro inhibits neuronal differentiation and survival. Exp. Cell Res. 1998, 241:210-221

Digital Image Processing, 2e. Rafael C. Gonzalez, Richard E. Woods & Steven L. Eddins. Prentice Hall, 2002

Dima A, Scholz M, Obermayer K. Automatic segmentation and skeletonization of neurons from confocal microscopy images based on the 3-D wavelet transform. IEEE Trans. Image Proc. 2002, 11:790-801

Ditlevsen DK, Kohler LB, Pedersen MV, Risell M, Kolkova K, Meyer M, Berezin V, Bock E. The role of PI3-kinase in NCAM-mediated neuronal differentiation and survival. J. Neurochem. 2003, 84:546-556

Doherty P, Walsh FS. Cell adhesion molecules, second messengers and axonal growth. Curr. Opin. Neurobiol. 1992, 2:595-560

Doherty P, Williams G, Williams EJ. CAMs and axonal growth: a critical evaluation of the role of calcium and the MAPK cascade. Mol. Cell Neurosci. 2000, 16:283-295. Review

Donato R. Intracellular and extracellular roles of S100 proteins. Microsc. Res. Tech. 2003, 60:540-551

Dong L, Chen S, Richter M, Schachner M. Single-chain variable fragment antibodies against the neural adhesion molecule CHL1 (close homolog of L1) enhance neurite outgrowth. J. Neurosci. Res. 2002, 69:437-447

Dong L, Chen S, Schachner M. Single chain Fv antibodies against neural cell adhesion molecule L1 trigger L1 functions in cultured neurons. Mol. Cell Neurosci. 2003, 22:234-247

Dorph-Petersen KA, Gundersen HJ, Jensen EB. Non-uniform systematic sampling in stereology. J. Microsc. 2000, 200:148-157

Dua RO, Hart PE. Pattern Classification and Scene Analysis. Wiley, 1973

Eberly D, Gardner R, Morse B, Pizer S, Scharlach. Ridges for image analysis. JMIV. 1994, 4:351-371

Edelman GM. Cell adhesion molecules in the regulation of animal form and tissue pattern. Ann. Rev. Cell Biol. 1986, 2:81-116. Review

Floderus S. Untersuchungen über den Bau der mentschlichen Hypophyse mit besonderer Berücksichtungen der quantitativen mikromorphologische Verhaltnisse. Acta pathol et microbiol scand. 1944, 53:1-276

Forbes SJ, Vig P, Poulsom R, Wright NA, and Alison MR. Adult stem cell plasticity: New pathways of tissue regeneration become visible. Clinical Sci. 2002, 103:355-369

Ford-Holevinski TS, Dahlberg TA, Agranoff BW. A microcomputer-based image analyzer for quantitating neurite outgrowth. Brain Res. 1986, 368:339-346

Fournier AE, Takizawa BT, Strittmatter SM. Rho kinase inhibition enhances axonal regeneration in the injured CNS. J. Neurosci. 2003, 23:1416-1423

Fullman DL. Measurement of particle sizes in opaque bodies. J. of Metals. 1953, 197:447-452.

GNU C Compiler. http://gcc.gnu.org/

Garcia-Finana M, Cruz-Orive LM. New approximations for the variance in Cavalieri sampling. J. Miscrosc. 2000, 199:224-238

Geiger D, Gupta A, Costa A, Vlontzos J. Dynamic programming for detecting, tracking, and matching deformable contours. IEEE Trans. 1995, 17:294-303

Geuna S, Tos P, Battison B, Guglielmone R, Giacobini-Robecchi. Morphological analysis of peripheral nerve regenerated by means of vein grafts filled with fresh skeletal muscle. Anat. Embryol. 2000, 201:475-482

Geuna S. Appreciating the difference between design-based and model-based sampling strategies in quantitative morphology of the nervous system. J. Comp. Neurol. 2000, 427:333-339. Review

Gitai Z, Yu TW, Lundquist EA, Tessier-Lavigne M, Bargmann CI. The netrin receptor UNC-40/DCC stimulates axon attraction and outgrowth through enabled and, in parallel, Rac and UNC-115/AbLIM. Neuron. 2003, 37:53-65

Gundersen HJ, Bagger P, Bendtsen TF, Evans SM, Korbo L, Marcussen N, Moller A, Nielsen K, Nyengaard JR, Pakkenberg B, et al. The new stereological tools: disector, fractionator, nucleator and point sampled intercepts and their use in pathological research and diagnosis. APMIS. 1988, 96:857-881. Review

Gundersen HJ, Jensen EB. The efficiency of systematic sampling in stereology and its prediction. J. Microsc. 1987, 147:229-263

Gundersen HJ, Østerby R. Optimizing sampling efficiency of stereological studies in biology: or 'do more less well!'. J. Microsc. 1981, 121:65-73

Gundersen HJ. The nucleator. J. Microsc. 1988, 151:3-21

Gundersen HJ. Stereology of arbitrary particles. A review of unbiased number and size estimators and the presentation of some new ones, in memory of William R. Thompson. J. Microsc. 1986, 143:3-45

Gundersen HJG, Jensen EBV, Kiêu K, Nielsen J. The efficiency of systematic sampling in stereology - reconsidered. J. Microsc. 1999, 193:199-211

Halfter W. A heparan sulfate proteoglycan in developing avian axonal tracts. J. Neurosci. 1993, 13: 2863-2873

Hansen K, Andersen JD. Understanding the Hough Transform: Hough cell support and its utilisation. Image and Vision Computing. 1997, 15:205-218

Haralick R. Ridges and valleys in digital images. CVGIP. 1983, 22:28-38.

Haralick RM, Shapiro LG. Survey: Image segmentation techniques. Comp. Vision, Graphics, Image proc. 1985, 29:100-132

Hartmann U, Maurer P. Proteoglycans in the nervous system–the quest for functional roles in vivo. Matrix Biol. 2001, 20:23-35

Hedreen JC. Lost caps in histological counting methods. Anat. Rec. 1998, 250:366-372

Hedreen JC. What was wrong with the Abercrombie and empirical cell counting methods? A review. Anat. Rec. 1998, 250:373-380. Review

Hedreen JC. Unbiased stereology? Trends Neurosci. 1999, 22:346-347

Hendry IA. A method to correct adequately fo rthe change in neuronal size when estimating neuronal number after nerve growth factor treatment. J. Neurocytol. 1976, 5:337-349

Henkemeyer M, Orioli D, Henderson JT, Saxton TM, Roder J, Pawson T, Klein R. Nuk controls pathfinding of commissural axons in the mammalian central nervous system. Cell. 1996, 86:35-46

Horowitz SL, Pavlidis T. Picture segmentation by a directed split-and-merge procedure. Technical report, Departement of Electrical Engineering, Princeton University , N. J. 08540, 1975

Horwitz DG, Thompson DJ. A generalization of sampling without replication from a finite universe. J. Amer. Statist. Assoc. 1952, 47:663-685

Hough PVC. Method and means of recognizing complex patterns, 1962. U.S. Patent 306965418.

Huang EJ, Reichardt LF. Neurotrophins: roles in neuronal development and function. Ann. Rev. Neurosci. 2001, 24:677-736

Huang TS, Yang GJ, Yang GY. A fast two-dimensional median filtering algorithm. IEEE Trans. Acoust. Speech Signal Proc. 1979, 27:13-18

IBM OS/2 Warp. http://www.ibm.com/software/os/warp/

Intel Image Processing Library. http://developer.intel.com/software/products/ipp

Isaacs KR, Hanbauser I, Jacobowitz DM. A method for the rapid analysis of neuronal properties and neurite morphology in primary cultures. Exp. Neurol. 1998, 149:464-467

Ivanov DB, Philippova MP, Tkachuk A. Structure and functions of classical cadherins. Biochemistry (Mosc). 2001, 66:1174-1186

Jap Tjoen San ER, Schmidt-Michels MH, Spruijt BM, Oestreicher AB, Schotman P, Gispen WH. Quantitation of the growth-associated protein B-50/GAP-43 and neurite outgrowth in PC12 cells. J. Neurosci. Res. 1991, 29:149-154

Ji L, Piper J. Fast homotopy-preserving skeletons using mathematical morphology. IEEE Trans. Pat. Anal. Mach. Intell. 1992, 14:653-664

Jin Z, Strittmatter SM. Rac1 mediates collapsin-1-induced growth cone collapse. J. Neurosci. 1997, 17:6256-6263

Jones LL, Sajed D, Tuszynski MH. Axonal regeneration through regions of chondroitin sulfate proteoglycan deposition after spinal cord injury: a balance of permissiveness and inhibition. J. Neurosci. 2003, 23:9276-9288

Joseph SJ, Ford MD, Barth C, Portbury S, Bartlett PF, Nurcombe V, Greferath U. A proteoglycan that activates fibroblast growth factors during early neuronal development is a perlecan variant. Development. 1996, 122:3443-3452

Kamber M, Shinghal R, Collins DL, Francis GS, Evans AC. Model-based 3-D segmentation of multiple sclerosis lesions in magnetic resonance brain images. IEEE Trans. Med. Imaging. 1995, 14:442-453

Karasik D. PDL-PrimaImage package. http://www.prima.eu.org/PDL-PrimaImage 2003

Karasik D. Prima, the Perl graphic toolkit. Online manual. http://www.prima.eu.org/download/Prima.pdf 2004

Keleman K, Dickson BJ. Short- and long-range repulsion by the Drosophila Unc5 netrin receptor. Neuron. 2001, 32:605-617

Kiryushko D, Berezin V, and Bock E. Regulators of neurite outgrowth. Ann. NY Acad. Sci. 2004, 1014:1-15.

Kiryushko D, Kofoed T, Skladchikova G, Holm A, Berezin V, Bock E. A synthetic peptide ligand of neural cell adhesion molecule (NCAM), C3d, promotes neuritogenesis and synaptogenesis and modulates presynaptic function in primary cultures of rat hippocampal neurons. J. Biol. Chem. 2003, 278:12325-12334.

Kiselyov VV, Berezin V, Maar TE, Soroka V, Edvardsen K, Schousboe A, Bock E. The first immunoglobulin-like neural cell adhesion molecule (NCAM) domain is involved in double-reciprocal interaction with the second immunoglobulin-like NCAM domain and in heparin binding. J. Biol. Chem. 1997, 272:10125-10134

Kiselyov VV, Skladchikova G, Hinsby AM, Jensen PH, Kulahin N, Soroka V, Pedersen N, Tsetlin V, Poulsen FM, Berezin V, Bock E. Structural basis for a direct interaction between FGFR1 and NCAM and evidence for a regulatory role of ATP. Structure (Camb). 2003, 11:691-701

Kiêu K, S, Istas J. Precision of systematic sampling and transitive methods. J. Stat. Planning and Inference. 1999, 77:263-279

Kiêu K. Three lectures on systematic geometric sampling. Memoirs 13, Department of Theoretical Statistics, University of Århus 1997.

Kligman D, Marshak DR. Purification and characterisation of a neurite extension factor from bovine brain. Proc. Natl. Acad. Sci. USA. 1985, 82:7736-7739

Kneip J, Ohmacht M, Rönner K, Pirsch P. Architecture and C++-programming environment of a highly parallel image signal processor. Microprocessing and Micro-programming 41 391-408, 1995

Koenderink JJ. The structure of images. Biol. Cybernetics, 1984, 50:363-370

Kolkova K, Novitskaya V, Pedersen N, Berezin V, Bock E. Neural cell adhesion molecule-stimulated neurite outgrowth depends on activation of protein kinase C and the Ras-mitogen-activated protein kinase pathway. J. Neurosci. 2000, 20:2238-2246

Kolkova K, Pedersen N, Berezin V, Bock E. Identification of an amino acid sequence motif in the cytoplasmic domain of the NCAM-140 kDa isoform essential for its neuritogenic activity. J. Neurochem. 2000, 75:1274-1212

Korshunova I, Novitskaya V, Pedersen P, Kolkova K, Rayko M, Kropotova E, Mosevitsky M, Rudka T, Morrow JS, Ginzburg I, Berezin V, Bock E. GAP-43 is a functional switch between NCAM-140 and NCAM-180. J. Nature Neurosci, submitted.

Kriajevska M, Tarabykina S, Bronstein I, Maitland N, Lomanosov M, Hansen K, Georgive G, Lukanidin E. Metastasis-associated Mts1 (S100A4) protein modulates protein kinase C phosphorylation of the heavy chain of nonmuscle myosin. J. Biol. Chem. 1998, 273:9852-9856

Køhler, L.B., Berezin, V., Bock, E. and Penkowa, M. The role of metallothionein II in neuronal differentiation and survival. Brain Res. 2003, 992: 128-136

Lam L, Lee SW, Suen CY. Thinning methodologies - A comprehensive survey. IEEE Trans. Pat. Anal. Mach. Intell. 1992 14:869-885

Latson L, Sebek B, Powell KA. Automated cell nuclear segmentation in color images of hematoxylin and eosin-stained breast biopsy. Anal. Quant. Cytol. Histol. 2003, 25:321-331

Lee FS, Kim AH, Khursigara G, Chao MV. The uniqueness of being a neurotrophin receptor. Curr. Opin. Neurobiol. 2001, 11:281-286

Levi-Montalcini R, Angeletti PU. Growth control of the sympathetic system by a specific protein factor. Q. Rev. Biol. 1961 Jun 36:99-108

Levine, MD. Vision in Man and Machine. McGraw-Hill, 1985

Li ZH, Spektor A, Varlamova O, Bresnick AR. Mts1 regulates the assembly of non-muscle myosin-iia. Biochemistry 2003, 42:14258-14266

Lieberman H. Integrating user interface agents with conventional applications. Knowledge-Based Systems. 1998, 11 15-23

Lindeberg T. Edge detection and ridge detection with automatic scale selection. Int J. of Computer Vision. 1996, 30 77-116

Lindley CA. Practical image processing in C: acquisition, manipulation, storage. ISBN: 0-471-53240-53241. Wiley, New York NY 1991

Linux Online. http://www.linux.org/

Livesey FJ. Netrins and netrin receptors. Cell Mol. Life Sci. 1999, 56:62-68

Maar TE, Rønn LC, Bock E, Berezin V, Moran J, Pasantes-Morales H, Schousboe A. Characterization of microwell cultures of dissociated brain tissue for studies of cell-cell interactions. J. Neurosci. Res. 1997, 47:163-172

Macagno ER, Levinthal C, Sobel I. Three-dimensional computer reconstruction of neurons and neuronal assemblies. Ann. Rev. Biophys. Bioeng. 1979, 8:323-351

Malgrange B, Delree P, Rigo JM, Baron. Image analysis of neurite regeneration by adult rat dorsal root ganglion neurons in culture: quantification of the neurotoxicity

of anticancer agents and of its prevention by nerve growth factor or basic fibroblast growth factor but not brain-derived neurotrophic factor or neurotrophin-3. J. Neurosci. Methods. 1994, 53:111-122

Mandarim-de-Lacerda CA. Stereological tools in biomedical research. An Acad. Bras. Cienc. 2003, 75:469-486. Review

Markus A, Patel TD, Snider WD. Neurotrophic factors and axonal growth. Curr. Opin. Neurobiol 2001, 12:523-531

Marr D. Vision: a computational investigation into the human representation and processing of visual information. W.H. Freeman, San Francisco 1982.

Martelli A. Edge detection using heuristic search methods. Comp. Graphics Image Proc. 1972, 1:169-182

Matheron G. The theory of regionalized variables and its applications. École Nationale Supérieure des Mines de Paris: Les Cahiers du Centre de Morphologie Matématique de Fontainebleau, 1971.

Matheron G. Les Variables Régionalisées et leur Estimation. Paris:Masson 1965.

Mathieu O, Cruz-Orive LM, Hoppeler H, Weibel ER. Measuring error and sampling variation in stereology: comparison of the efficiency of various methods for planar image analysis. J. Microsc. 1981, 121:75-88

Mayhew TM, Gundersen HJG. If you assume, you can make an ass out of u and me': a decade of the disector for stereological counting of particles in 3D space. J. Anat. 1996, 188 (Pt 1):1-15. Review.

McKerracher L. Spinal cord repair: Strategies to promote axon regeneration. Neurobiol Disease 2001, 8:11-18

Meijering E, Jacob M, Sarria JCF, Steiner P, Hirling H, Unser M. Design and validation of a tool for neurite tracing and analysis in fluorescence microscopy images. Cytometry 2004, 58A:167-176

Meiners S, Nur-e-Kamal MS, Mercado ML. Identification of a neurite outgrowth-promoting motif within the alternatively spliced region of human tenascin-C. J. Neurosci. 2001, 21:7215-7225

102

Mendis-Handagama, SMLC. Estimation error of Leydig cell numbers in atrophied rat tests due to the assumptions of spherical nuclei. J. Microsc. 1992, 168:25-32

Microsoft Visual C++. http://msdn.microsoft.com/visualc/

Microsoft Windows. http://www.microsoft.com/windows

Mochizuki M, Kadoya Y, Wakabayashi Y, Kato K, Okazaki I, Yamada M, Sato T, Sakairi N, Nishi N, Nomizu M. Laminin-1 peptide-conjugated chitosan membranes as a novel approach for cell engineering. FASEB J. 2003, 17:875-877

Moreno-Flores MT, Martin-Aparicio E, Avila J, Diaz-Nido J, Wandosell F. Ephrin-B1 promotes dendrite outgrowth on cerebellar granule neurons. Mol. Cell Neurosci. 2002, 20:429-446

Morgenstern DA, Asher RA, Fawcett JW. Chondroitin sulphate proteoglycans in the CNS injury response. Prog. Brain Res. 2002, 137:313-332.

Mouton PR, Gokhale AM, Ward NL, West MJ. Stereological length estimation using spherical probes. J. Microsc. 2002, 206:54-64

Mumford D, Shah J. Optimal approximations by piecewise smooth functions and variational problems. CPAM, 1988 XLII:577-685

Murphy M, Drago J, Bartlett PF. Fibroblast growth factor stimulates the proliferation and differentiation of neural precursor cells in vitro. J. Neurosci. Res. 1990, 25:463-475

Neiiendam J, Køhler L, Pedersen MV, Ditlevsen DK, Kornum MK, Berezin V and Bock E. An NCAM-derived FGF-receptor agonist, the FGL-peptide, induces neurite outgrowth and neuronal survival in primary rat neurons. J. Neurochem. 2004, 91:920-935

Novitskaya V, Grigorian M, Kriajevska M, Tarabykina S, Bronstein I, Berezin V, Bock E, Lukanidin E. Oligomeric forms of the metastasis-related Mts1 (S100A4) protein stimulate neuronal differentiation in cultures of rat hippocampal neurons. J. Biolog Chem 2000, 275:41278-41286

Oertle T, van der Haar ME, Bandtlow CE, Robeva A, Burfeind P, Buss A, Huber AB, Simonen M, Schnell L, Brosamle C, Kaupmann K, Vallon R, Schwab ME. Nogo-A

inhibits neurite outgrowth and cell spreading with three discrete regions. J. Neurosci. 2003, 23:5393-5406

Olsen OF, Nielsen M. Generic events for the gradient squared with application to multi-scale segmentation. Scale-Space, 1997:101-112

Oohira A, Kushima Y, Tokita Y, Sugiura N, Sakurai K, Suzuki S, Kimata K. Effects of lipid-derivatized glycosaminoglycans (GAGs), a novel probe for functional analyses of GAGs, on cell-to-substratum adhesion and neurite elongation in primary cultures of fetal rat hippocampal neurons. Arch Biochem Biophys. 2000, 378:78-83

Orwant J, Hietaniemi J, Macdonald J. Mastering algorithms with Perl. O'Reilly, 1999

Otsu N. A threshold selection method from grey-level histograms. IEEE Trans. Systems, Man, and Cybernetics, 1979, 9:377-393

Pasterkamp RJ, Peschon JJ, Spriggs MK, Kolodkin AL. Semaphorin 7A promotes axon outgrowth through integrins and MAPKs. Nature. 2003, 424:398-405

Pataky DM, Borisoff JF, Fernandes KJL, Tetzlaff W, Steeves JD. Fibroblast growth factor produces differential effects on survival and neurite outgrowth from identified bulbospinal neurons in vitro. Exp. Neurol. 2000, 163:357-372

Patel TD, Jackman A, Rice FL, Kucera J, Snider WD. Development of sensory neurons in the absence of NGF/TrkA signaling in vivo. Neuron, 2000, 25:345-357

Pavlov I, Voikar V, Kaksonen M, Lauri SE, Hienola A, Taira T, Rauvala H. Role of heparin-binding growth-associated molecule (HB-GAM) in hippocampal LTP and spatial learning revealed by studies on overexpressing and knockout mice. Mol. Cell Neurosci. 2002, 20:330-342

Pedersen MV, Køhler LB, Ditlevsen DK, Li S, Berezin V, Bock E. Neuritogenic and survival-promoting effects of the P2 peptide derived from a homophilic binding site in the neural cell adhesion molecule. J. Neurosci. Res. 2004, 75 55-65

Pedersen MV., Køhler LB., Grigorian M., Lukanidin E., Bock E. and Berezin V. The Mts1 (S100A4) protein is a neuroprotectant. J. Neurosci. Res. 2004, 77:777-786

Perron JC, Bixby JL. Distinct neurite outgrowth signaling pathways converge on ERK activation. Mol. Cell Neurosci. 1999, 13:362-378

Pover CM, Coggeshall RE. Verification of the disector method for counting neurons, with comments on the empirical method. Anat. Rec. 1991, 231:573-578

Pratt, WK. Digital Image Processing, 2nd ed. John Wiley, NY, 1991.

Prechelt L. An empirical comparison of C, C++, Java, Perl, Python, Rexx, and Tcl for a search/string-processing program. http://www.ubka.uni-karlsruhe.de/cgi-bin/psview?document=/ira/2000/5

Raff MC. Social control on cell survival and cell death. Nature 1992, 365:397-400

Ralets I, Ostergaard S, Holm A, Kohler L, Bock E, and Berezin V. Identification of neurite extension inducing peptides by means of soluble combinatorial peptide libraries. J. Neurosci. Methods 2004, 137:61-69.

Ranefall P, Egevad L, Nordin B, Bengtsson E. A new method for segmentation of colour images applied to immunohistochemically stained cell nuclei. Anal. Cell Pathol. 1997, 15:145-156

Rauch U, Feng K, Zhou XH. Neurocan: a brain chondroitin sulfate proteoglycan. Cell Mol. Life Sci. 2001, 58:1842-1856.

Raulo E, Julkunen I, Merenmies J, Pihlaskari R, Rauvala H. Secretion and biological activities of heparin-binding growth-associated molecule. Neurite outgrowth-promoting and mitogenic actions of the recombinant and tissue-derived protein.J. Biol. Chem. 1992, 267:11408-11416

Retzler C, Gohring W, Rauch U. Analysis of neurocan structures interacting with the neural cell adhesion molecule N-CAM. J. Biol. Chem. 1996, 271:27304-27310

Rigato F, Garwood J, Calco V, Heck N, Faivre-Sarrailh C, Faissner A. Tenascin-C promotes neurite outgrowth of embryonic hippocampal neurons through the alternatively spliced fibronectin type III BD domains via activation of the cell adhesion molecule F3/contactin. J. Neurosci. 2002, 22:6596-6609

Ringstedt T, Braisted JE, Brose K, Kidd T, Goodman C, Tessier-Lavigne M, O'Leary DD. Slit inhibition of retinal axon growth and its role in retinal axon pathfinding and innervation patterns in the diencephalon. J. Neurosci. 2000, 20:4983-4991

Ruoslahti E, Obrink B. Common principles in cell adhesion. Exp. Cell Res. 1996, 227:1-11

Russ JC, Dehoff RT. Practical Stereology. Second edition. Kluwer Academics/Plenum Publishers New York, 2000

Russ JC. The Image Processing Handbook. CRC Press, 1995.

Rønn LC, Dissing S, Holm A, Berezin V, Bock E. Increased intracellular calcium is required for neurite outgrowth induced by a synthetic peptide ligand of NCAM. FEBS Lett. 2002, 518:60-66

Rønn LC, Olsen M, Ostergaard S, Kiselyov V, Berezin V, Mortensen MT, Lerche MH, Jensen PH, Soroka V, Saffell JL, Doherty P, Poulsen FM, Bock E, Holm A, Saffells JL. Identification of a neuritogenic ligand of the neural cell adhesion molecule using a combinatorial library of synthetic peptides. Nat. Biotechnol. 1999, 17:1000-1005

Rønn LC, Ralets I, Hartz BP, Bech M, Berezin A, Berezin V, Moller A, Bock E. A simple procedure for quantification of neurite outgrowth based on stereological principles. J. Neurosci. Methods. 2000, 100:25-32

SGI IRIX. http://www.sgi.com/software/irix/

Sack U, Knoechnera S, Warschkaub H, Piglac U, Emmricha F, Kamprad M. Computer-assisted classification of HEp-2 immunofluorescence patterns in autoimmune diagnostics. Autoimmun. Rev. 2003, 2:298-304.

Sang Q, Tan SS. Contact-associated neurite outgrowth and branching of immature cortical interneurons. Cereb. Cortex. 2003, 13:677-683

Sato Y, Nakajim S, Shigara N, Atsumi H, Yoshida S, Koller T, Gerig G, Kikinis R. Three-dimensional multi-scale line filter for segmentation and visualization of curvilinear structures in medical images. Med. Image Anal. 1998, 2:143-168

Savikko V. Generative and incremental approach to scripting support implementation. Software Engineering Research and Practice 2003, 105-111

Schmitz C, Korr H, Heinsen H. Design-based counting techniques: the real problems. Trends Neurosci. 1999, 22:345-346

Scilab documentations. http://cyvision.if.sc.usp.br/~rfabbri/sip

Serra J. Image Analysis and Mathematical Morphology. Academic Press, London, 1982

Shi J, Malik J. Normalized Cuts and Image Segmentation. IEEE Trans. Pat. Anal. Mach. Intell. 2000, 22

Shiga T, Oppenheim RW. Immunolocalization studies of putative guidance molecules used by axons and growth cones of intersegemental interneurons in the chick embryo spinal cord. J. Comp. Neurol. 1991, 310:234-252

Sifakis E, Garcia C, Tziritas G. Bayesian level sets for image segmentation. J. Visual Comm. and Image Representation. 2002, 13:44-64

Smith TW, Yun Z, Mender DG, McIntire LV, Nicolson GL. Computerized analysis of tumor cell interactions with extracellular matrix proteins, peptides, and endothelial cells under laminar flow. Biotechnol. Bioeng. 1996, 50:598-607

Smolen AJ, Wright LL, Cunningham TJ. Neuron numbers in the superior cervical sympathetic ganglion of the rat: a critical comparison of methods for cell counting. J. Neurocytol. 1983, 12:739-750

Soeller C, Lukka TJ, Glazebrook K et al. The PDL manuals. http://pdl.sourceforge.net/PDLdocs

Sofroniev MV, Howe CL, Mobley WC. Nerve growth factor signaling, neuroprotection, and neural repair. Ann. Rev. Neurosci. 2001, 24:1217-1281

Sonka M, Hlavac V, Boyle R. Image processing, analysis, and machine vision. Brooks/Cole Publishing Comp. 1998

Sonka M, Winniford MD, Collins SM. Robust simultaneous detection of coronary borders in complex images. IEEE Trans. Med. Imaging, 1994, 14:151-161

Sorci G, Riuzzi F, Agneletti AL, Marchetti C, Donato R. S100B inhibits myogenic differentiation and myotube formation in a RAGE-independent manner. Mol. Cell Biol. 2003, 23:4870-4881

Soroka V, Kiryushko D, Novitskaya V, Rønn LC, Poulsen FM, Holm A, Bock E, Berezin V. Induction of neuronal differentiation by a peptide corresponding to the homophilic binding site of the second Ig module of the neural cell adhesion molecule. J. Biol. Chem. 2002, 277:24676-24683

Soroka V, Kolkova K, Kastrup JS, Diederichs K, Breed J, Kiselyov VV, Poulsen FM, Larsen IK, Welte W, Berezin V, Bock E, Kasper C. Structure and interactions of NCAM Ig1-2-3 suggest a novel zipper mechanism for homophilic adhesion. Structure (Camb). 2003 Oct 11:1291-1301

Sporring J, Nielsen M, Florac L, Johansen P. Gaussian scale-space theory. Kluwer Academic Publishers, Netherlands 1997

Sterio DC. The unbiased estimation of number and sizes of arbitrary particles using the disector. J. Microsc. 1984, 134:127-136

Tai LC. The GUI Toolkit, Framework Page http://www.atai.org/guitool/ 2003

Takenouchi T, Kadosaka M, Shin SY, Munekata E. Biological actions of the epidermal growth factors-like domain peptides of mouse schwannoma-derived growth factor and human amphiregulin. J. Pept. Res. 1999, 53:120-125

Tardy M. Role of laminin bioavailability in the astroglial permissivity for neurite outgrowth. An Acad. Bras. Cienc. 2002, 74:683-690

Tatsumi N, Pierre RV. Automated image processing. Past, present, and future of blood cell morphology identification. Clin. Lab. Med. 2002, 22:299-315, viii. Review

The FreeBSD Project. http://www.freebsd.org/

The Perl Directory. http://www.perl.org/

The R Project for Statistical Computing. http://www.r-project.org/

Tessier-Lavigne M, Goodman CS. The molecular biology of axon guidance. Science. 1996 274:1123-33. Review

Thomas AD, Davies T, Luxmoore AR. The Hough transform for locating cell nuclei. Anal. Quant. Cytol. Histol. 1992 347-353

Titterington DMA, Smith FM, Markov UE. Statistical Analysis of Finite Mixture Distributions. John Wiley & Sons, Chichester, 1985

Tk widget for Perl. http://www.perltk.org/

Tkach V, Tulchinsky E, Lukanidin E et al. Role of Fos family members, c-Fos, Fra-1 and Fra-2, in the regulation of cell motility. Oncogene 2003, 22:5045-5054

Treubert U, Brummendorf T. Functional cooperation of beta1-integrins and members of the Ig superfamily in neurite outgrowth induction. J. Neurosci. 1998, 18:1795-1805

Tucker KG, Chalder S, Al-Rubeai M, Thomas CR. Measurement of hybridoma cell number, viability, and morphology using fully automated image analysis. Enzyme Microb. Technol. 1994, 16

Turnley AM, Bartlett PF. MAG and MOG enhance neurite outgrowth of embryonic mouse spinal cord neurons. Neuroreport. 1998, 9:1987-1990

Vaughn DE, Bjorkman PJ. The (Greek) key to structures of neural adhesion molecules. Neuron. 1996, 16:261-273

Vincent L, Soille P. Watersheds in digital spaces: an efficient algorithm based on immersion simulations. IEEE Trans. Patt. Anal. Mach. Intell. 1991, 13:583-598

Vincent L. Morphological grayscale reconstruction in image analysis: applications and efficient algorithms. IEEE Trans. Image Proc. 1993, 2:176-201

Vinson M, Strijbos PJ, Rowles A, Facci L, Moore SE, Simmons DL, Walsh FS. Myelin-associated glycoprotein interacts with ganglioside GT1b. A mechanism for neurite outgrowth inhibition. J. Biol. Chem. 2001, 276:20280-20285.

Wall L, Christiansen T, Orwant J. Programming Perl, 3rd edition. O'Reilly, 2000

Walmod PS, Hartmann-Petersen R, Berezin A, et al. Evaluation of individual-cell motility. Methods in Molecular Biology: Cytoskeleton Methods and Protocols, 2000 161, Humana Press Inc. Totowa, NJ

Walmod PS, Hartmann-Petersen R, Prag S, Lepekhin EL, Röpke C, Berezin V, Bock E. Cell-cycle-dependent regulation of cell motility and determination of the role of Rac1. Exp. Cell Res. 2004, 295:407-420

Walsh N. Learning Perl/Tk. O'Reilly, 1999

Watson M. Portable gui development with C++. McGraw-Hill Osborne Media, 1993

Weaver CM, Pinezich JD, Brent Lindquist W, Vazquez ME. An algorithm for neurite outgrowth reconstruction. J. Neurosci. Methods. 124 2003:197-205

West MJ. New stereological methods for counting neurons. Neurobiol. Aging 1993, 14:275-285

West MJ. Stereological methods for estimating the total number of neurons and synapses: issues of precision and bias. Trends Neurosci. 1999, 22:51-61. Review

Wiederkehr A, Staple J, Caroni P. The motility-associated proteins GAP-43, MAR-CKS, and CAP-23 share unique targeting and surface activity-inducing properties. Exp. Cell Res. 1997, 236:103-116

Williams EJ, Furness J, Walsh FS, Doherty P. Characterisation of the second messenger pathway underlying neurite outgrowth stimulated by FGF. Development 19941685-19941693.

Winningham-Major F, Staecker JL, Barger SW, Coats S, Van Eldik LJ. Neurite extension and neuronal survival activities of recombinant S100 beta proteins that differ in the content and position of cysteine residues. J. Cell Biol. 1989, 109:3063-3071

Witkin AP. Scale-space filtering. In Proc. 4th Int. Joint Conf. on Artificial Intell. 1983:1019-1022

WxWindows documentation. http://www.wxwindows.org

Zheng Q, Milthorpe BK, Jones AS. Direct neural network application for automated cell recognition. Cytometry. 2004, 57A:1-9

Zhu SC, Yuille A. Region competition: unifying snakes, region growing, and Bayes/MDL for Multiband Image Segmentation. IEEE Trans. Pat. Anal. Mach. Intell. 1996, 18

Zucker SW. Region growing: childhood and adolescence. Comp. Graphics Image Proc. 1976, 5:382-399